The MRi-Share database: brain imaging in a cross-sectional cohort of 1,870 university students.

Ami Tsuchida, Alexandre Laurent, Fabrice Crivello, Laurent Petit, Marc Joliot, Antonietta Pepe, Naka Beguedou, Marie-Fateye Gueye, Violaine Verrecchia, Victor Nozais, et al.

The MRi-Share database: brain imaging in a cross-sectional cohort of 1,870 university students

Ami Tsuchida[1,2,3], Alexandre Laurent[1,2,3], Fabrice Crivello[1,2,3], Laurent Petit[1,2,3], Marc Joliot[1,2,3,4], Antonietta Pepe[1,2,3], Naka Beguedou[1,2,3], Marie-Fateye Gueye[1,2,3,4], Violaine Verrecchia[1,2,3,4], Victor Nozais[1,2,3,4], Laure Zago[1,2,3], Nathalie Tzourio-Mazoyer[1,2,3], Emmanuel Mellet[1,2,3], Stephanie Debette[5,6], Christophe Tzourio[5,6], Bernard Mazoyer[1,2,3,4,6,CA]

Abstract We report on MRi-Share, a multi-modal brain MRI database acquired in a unique sample of 1,870 young healthy adults, aged 18 to 35 years, while undergoing university-level education. MRi-Share contains structural (T1 and FLAIR), diffusion (multispectral), susceptibility weighted (SWI), and resting-state functional imaging modalities. Here, we described the contents of these different neuroimaging datasets and the processing pipelines used to derive brain phenotypes, as well as how quality control was assessed. In addition, we present preliminary results on associations of some of these brain image-derived phenotypes at the whole brain level with both age and sex, in the subsample of 1,722 individuals aged less than 26 years. We demonstrate that the post-adolescence period is characterized by changes in both structural and microstructural brain phenotypes. Grey matter cortical thickness, surface area and volume were found to decrease with age, while white matter volume shows increase. Diffusivity, either radial or axial, was found to robustly decrease with age whereas fractional anisotropy only slightly increased. As for the neurite orientation dispersion and densities, both were found to increase with age. The isotropic volume fraction also showed a slight increase with age. These preliminary findings emphasize the complexity of changes in brain structure and function occurring in this critical period at the interface of late maturation and early aging.

Keywords MRI · brain · student · cohort · cross-sectional · post-adolescence

Introduction

There is mounting evidence indicating the importance of early life factors on cognitive status and neurological conditions later in life (Whalley et al., 2006). Genetic factors can shape early brain development as well as cognitive ageing processes through common molecular pathways (Kovacs et al., 2014), and early life conditions (e.g. pre- and postnatal environment, socioeconomic status, educational attainment) as well as lifestyle choices contribute to risk factors for cerebrovascular diseases and dementia later in life (e.g. Backhouse et al., 2017; Corley et al., 2018; Wajman et al., 2018). The vast majority of epidemiological studies investigating the risk factors for late-onset neurological conditions tend to focus either on the middle- to old-age population (e.g. Debette et al., 2011; Kivipelto et al., 2001; Whitmer et al., 2007) or on childhood (Backhouse et al., 2017; Field et al., 2016; Gluckman et al., 2008). Likewise, many large-scale neuroimaging cohort studies have charted morphological changes associated with healthy and pathological development and ageing, focusing on early and late childhood to early adulthood for development (e.g. PING, Jernigan et al., 2016; PNC, Satterthwaite et al., 2016; IMAGEN, Schumann et al., 2010; Generation R, White et al., 2013) or on middle- to late-life for ageing (Three-City, 3C Study Group, 2003; UK-Biobank (UKB), Alfaro-Almagro et al., 2018; 1000BRAINS, Caspers et al., 2014; LBC1936, Deary et al., 2007; Rotterdam, Ikram et al., 2017; EVA, Lemaître et al., 2005; LIFE, Loeffler et al., 2015; OASIS, Marcus et al., 2010; BILGIN, Mazoyer et al., 2016; SYS, Pausova et al., 2017; ADNI, Petersen et al., 2010; MAS, Sachdev et al., 2010, OATS, 2009; ASPS-Fam, Seiler et al., 2014; Framingham, Seshadri et al., 2004). Consequently, there is a relative paucity of epidemiological data

Corresponding author: (CA)
Bernard Mazoyer
bernard.mazoyer@u-bordeaux.fr

[1] Université de Bordeaux, Institut des Maladies Neurodégénératives, UMR5293, Groupe d'Imagerie Neurofonctionnelle, Bordeaux, France

[2] CNRS, Institut des Maladies Neurodégénératives, UMR5293, Groupe d'Imagerie Neurofonctionnelle, Bordeaux, France

[3] CEA, Institut des Maladies Neurodégénératives, UMR5293, Groupe d'Imagerie Neurofonctionnelle, Bordeaux, France

[4] Fealinx and Université de Bordeaux, Ginesislab, Bordeaux, France

[5] Université de Bordeaux, Inserm, Bordeaux Population Health Research Center, UMR1219, CHU Bordeaux, Bordeaux, France

[6] Centre hospitalier universitaire Pellegrin, Bordeaux, France

and neuroimaging cohorts focusing on early adulthood, despite the significant life changes many undergo during this period, as they explore the world to attain independence and, for some, pursue higher education. While the most rapid brain changes occur during early development and the total brain size reaches adult levels by the end of childhood, both global and regional changes in brain structure and function continue throughout this period (Dumontheil, 2016). Yet, few studies investigate the impact of learning and social changes associated with higher education on maturational changes in the brain, and how it interacts with the personal traits, physical and mental health status to influence immediate as well as later-life events. Such data are crucial both for developing effective policies and interventions for promoting student health and well-being, and for gaining insight into the early life factors associated with vulnerabilities later in life.

The i-Share (for internet-based Student Health Research enterprise; www.i-share.fr) cohort project was conceived to fill this gap. It aims to evaluate important health aspects among 30,000 university students over the course of 10 years. Besides the evaluation of the frequency and impact of specific health conditions, i-Share will also allow for testing of biological mechanisms and preventive strategies for mental and physical health conditions in young adults. Launched in 2013, it has collected detailed information pertaining to personal characteristics and lifestyle habits, including risk-taking behaviours, physical activity, diet, sleep, and cognitive abilities, through web-based questionnaires, as well as medical and health status.

An important sub-component of the i-Share study, which was called “MRi-Share”, is a multi-modal brain magnetic resonance imaging (MRI) database collected in a subset of i-Share participants. The specific motivations behind MRi-Share were to 1) characterize late-maturational changes of post-adolescence brain; 2) investigate the impact of higher education on late maturational processes of the brain; 3) study the associations between brain phenotypes and neuropsychiatric conditions prevalent in young adults, such as migraine, depression and anxiety disorders, and substance abuse ; and 4) establish the early occurrence of imaging biomarkers of late-life disorders, such as white matter hyperintensities (WMH) and enlarged perivascular space (ePVS). Nearly all MRi-Share participants enrolled in another closely associated i-Share sub-component, called “Bio-Share”, a biobank derived from analyses of blood samples, used to generate large scale multi-modal molecular biomarkers. Together, these two i-Share components permit the exploration of early neuroimaging-based biomarkers for late-onset neurocognitive conditions such as cerebrovascular disease and dementia.

The primary goal of the present manuscript is to describe the MRi-Share image acquisition protocol as well as the analysis pipelines used for deriving brain phenotypes from MRI. These image-derived phenotypes (IDPs) include 1) measures of both volume- and surface-based brain morphometry from structural MRI, 2) measures of the organization of the white matter microstructure organization based on diffusion MRI, and 3) measures of intrinsic functional connectivity derived from resting-state functional MRI. These phenotypes were obtained at both the brain, regional, and voxel levels. A special care has been taken to detail the quality control (QC) steps, since there is an increasing awareness of the impact of QC procedures and metrics on IDPs of morphometry (Ducharme et al., 2016; Madan, 2018; Reuter et al., 2015) and white matter properties (Roalf et al., 2016). The secondary goal is to present preliminary results on associations of some of these IDPs at the whole brain level with both age and sex, in this large cross-sectional cohort of post-adolescence individuals.

Data Acquisition

MRi-Share study protocol

The study protocol was approved by the local ethics committee (CPP2015-A00850-49). All participants were recruited through the larger i-Share cohort study. The i-Share participants recruited at the Bordeaux site were given the information regarding MRi-Share and Bio-Share substudies. Those interested in contributing received detailed information about both substudies, including a “virtual visit” to the MRI facility that gave the participants a better idea about what was involved, and were invited to make an appointment with one of the MD investigators. The MD investigator ensured that each participant received all the information pertinent to the participation in both studies, and also checked for the absence of any cause for exclusion. Exclusion criteria were: 1) age over 35 years; 2) pregnancy or nursing; 3) claustrophobia; and 4) contraindications for head MRI. Participants then signed an informed written consent form, and scheduled for the MRI session, after which they received compensation for their contribution.

Out of 2,000 individuals who met with the MD investigators between October 2015 and June 2017, 29 were either not willing to participate in the MRi-Share or found to be ineligible. Additional 46 withdrew from the study before scheduling the MRI session, and another 7 participants withdrew at the scheduled session, before the scanning took place. Forty-eight students had been eligible and willing to participate, but could not be scheduled before the acquisition terminated in November 2017, and therefore were never scanned. Out of the remaining 1,870 participants who underwent the scanning session, two individual

datasets were removed, one because a participant withdrew from the study after being scanned, the other due to instrument failure during scanning. In addition, there were incidental findings requiring medical referral in 36 participants (see Incident findings section for details), and their imaging data were subsequently removed from further analyses, making the final sample size of 1,832.

Demographic information

While the larger i-Share study collected a detailed socio-demographic, health and lifestyle-related information through web-based questionnaires (see Montagni et al., 2019 for examples of domains covered by the study), we report here a limited set of demographic variables collected specifically in association with the MRi-Share protocol. These include sex and age at the time of MRI acquisition, as summarized in Table 1. The table also contains the proportion of each sex for the entire i-Share cohort for comparison. It can be seen that the high proportion of females relative to males in the MRi-Share is a feature of the larger i-Share cohort itself. Actually, a higher proportion of women among University students is observed at the French national level (55%, source France Ministry for Higher Education, Research and Innovation 2019: https://cache.media.enseignementsup-recherche.gouv.fr/file/Brochures/32/8/parite2018_stats_A5_11d_908328.pdf). It is amplified in the i-Share cohort due to an over-recruitment of students coming from faculties in which even larger proportion of women are observed (medical and paramedical sciences, social sciences).

While the study protocol allowed enrolment of students up to 35 years of age, almost 95% of our sample was under 26 years old (95th percentile values for age in the entire sample = 26.3 years old; see Figure 1). We thus focused on the subsample under 26 years of age when describing the association of the MRI image derived phenotypes (IDPs) with age and sex in the sections below. Table 1 provides the demographic summary of this sub-sample as well. Males and females in our sample had a small but significant difference in their age (difference in mean age < 4 months, $p = 0.007$, *t*-test) in the entire cohort, but the difference was marginal in the sub-sample of under 26 year-olds (2 months difference in age, $p = 0.068$, *t*-test).

Table 1. Basic characteristics of the MRi-Share database. Age (mean ± SD and range, in years) of the MRi-Share participants are shown for entire sample as well as for those under 26 years old, for each sex separately and in the combined group. The proportion of each sex in the larger i-Share cohort is also shown for comparison.

		Females	Males	Total
i-Share (as of 11/2019)	N (%)	13,064 (75.1%)	4,323 (24.9%)	17,414
MRi-Share	N(%)	1,320 (72.0%)	512 (28.0%)	1,832
	Age (years)	22.0 ± 2.3 [18.1, 34.9]	22.3 ± 2.4 [18.1, 31.3]	22.1 ± 2.3 [18.1, 34.9]
MRi-Share (< 26 years old)	N (%)	1,252 (72.7%)	470 (27.3%)	1,722
	Age (years)	21.7 ± 1.7 [18.1, 26.0]	21.9 ± 1.8 [18.1, 25.9]	21.7 ± 1.8 [18.1, 26.0]

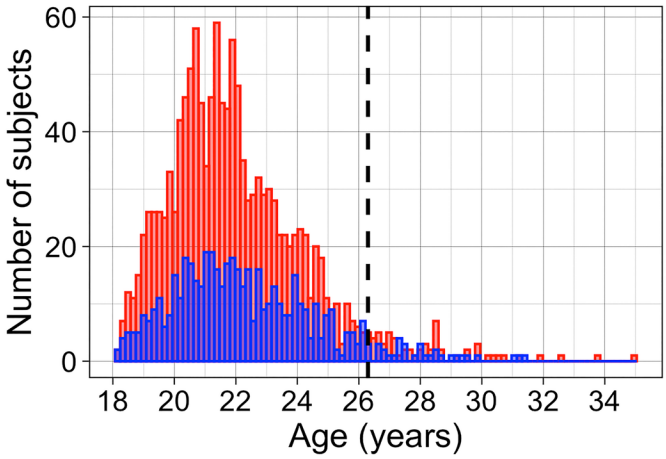

Figure 1. Age distribution histogram of the entire MRi-Share database. The age distribution histogram is shown for male (blue) and female (red). The dotted line indicates the 95th percentile of the distribution.

MRI acquisition

The MRI acquisition protocol for the MRi-Share database was designed to closely emulate that of the UKB MR brain imaging study (Alfaro-Almagro et al., 2018), in terms of both modalities and scanning parameters for each. We emulated the UKB brain MRI protocol so that it would allow the combined analysis of the two databases in the future, as the early adulthood target period of MRi-Share is not covered by the UKB design which includes individuals aged over 45 years old.

There were, still, some differences between the MRi-Share and UKB neuroimaging protocols. First, we did not include task-related fMRI runs and used the time gained to extend the resting-state fMRI (rs-fMRI) acquisition duration which lasted for ~15 min (instead of 6 min in the UKB) resulting in 1,054 volumes for MRi-Share (to be compared with 490 in the UKB rs-fMRI). Another minor difference in the scanning protocol was in diffusion weighted imaging (DWI): we acquired 8, 32, and 64 directions each for *b* values 300, 1000, and 2000 s/mm^2, respectively, while the UKB did not acquire *b* value of 300 s/mm^2 and instead acquired 50 directions each for *b* values 1000, and 2000 s/mm^2. We also had slightly more sets of $b = 0$ images acquired in Anterior-Posterior (AP) and the reverse PA phase encoding (8 pairs of AP and PA) than in UKB (3 pairs).

All neuroimaging data were acquired on the same Siemens 3T Prisma scanner with a 64-channels head coil (gradients: 80 mT/m - 200 T/m/s), in the 2-year period between November 2015 and November 2017.

Table 2 summarizes the key acquisition parameters for each imaging modality. The whole acquisition session lasted ~45 min. Prior to the rs-fMRI acquisition, participants were instructed to "keep their eyes closed, to relax, to refrain from moving, to stay awake, and to let their thoughts come and go", for the duration of the 15 min-long run. Compliance to the instruction was checked by the questions included in the self-report questionnaire, performed at the end of the scanning session.

While all 1,832 participants completed the structural scans (T1 and FLAIR), 17 did not complete the whole scanning session (2 with missing SWI, DWI, and rs-fMRI, 15 with missing or incomplete DWI and/or rs-fMRI) either due to anxiety attack or technical problems during scanning. The number of total images acquired for each scan (excluding the incidentals) is also listed in Table 2. For the description of each modality, we refer readers to the overview provided by Alfaro-Almagro et al. (2018).

Incident findings

Within days following the acquisition, T1 and FLAIR images were visually checked for quality by one of the three trained MD investigators (B.M, E.M). In the course of this quality control (QC) procedure, presence of any incident finding was recorded and paid special attention to when performing modality-specific individual QC (described in the Quality control section). In addition, any potentially harmful incident finding was sent to another neuroradiologist for a second opinion. Upon confirmation by the neuroradiologist, discovery of the incidental finding in a participant was notified to a neurologist investigator of the i-Share study (S.D) who took care of the participant information and follow-up. A total of 36 participants (1.9%) were identified as having incidental requiring medical referral and their data were excluded from analyses presented in the present manuscript. A detailed description of these incidental findings will be published in a separate report.

Automated image analysis pipelines

The acquired data were managed and processed with the Automated Brain Anatomy for Cohort Imaging platform (ABACI, IDDN.FR.001.410013.000.S.P.2016.000.31235) which integrates processing pipelines built with a *nipype* interface (Gorgolewski et al., 2011) with the Extensible Neuroimaging Archive Toolkit (XNAT; http://www.xnat.org) database management system. Through this platform, all image processing, except rs-fMRI data, was performed using a dedicated computing cluster system composed of CPU servers, in a python 3.6.3 environment, with *nipype* version 1.0.2. For running functions from the Statistical Parametric Mapping (SPM12: https://www.fil.ion.ucl.ac.uk/spm/), Matlab compiler runtime (MCR) was used (R2010A, v713, The Mathworks, Natick, MA). Processing of the rs-fMRI data was computed on CURTA, a shared computing cluster provided by the Mésocentre de Calcul Intensif Aquitain (MCIA) dedicated to intensive parallel computation. The python (3.6.5) and *nipype* (1.0.2) environment, and the resting-state pipeline contained in the ABACI platform were packaged on a single "resting state" singularity container (Kurtzer et al., 2017), together with all other tools and softwares the pipeline depended on. It used the same MCR v713 when running any functions from SPM12, but used MCR R2018a v94 when running other custom functions in Matlab. The main ABACI image analysis pipelines are briefly described below and detailed in the supplementary material section.

Table 2. Summary of acquisition parameters. For each of the five modalities, the key acquisition parameters are listed. T1: T1-weighted imaging, MPRAGE: magnetization-prepared rapid acquisition with gradient echo, TR: repetition time, TE: echo time, TI: inversion time, FLAIR: Fluid-attenuated inversion recovery imaging, SPACE: sampling perfection with application-optimized contrasts using different flip angle evolutions, R: in-plane acceleration factor, PF: partial Fourier, SWI: susceptibility-weighted imaging, DWI: diffusion weighted imaging, MB: multiband factor, AP/PA: anterior-posterior/posterior-anterior; b-values are in s/mm2 and the number of directions is given in parentheses. rs-fMRI: resting-state functional magnetic resonance imaging; EPI: EchoPlanar Imaging.

Modality	Duration	Voxel (matrix) size	Key parameters	# vol	*N*
T1	4:54	1.0x1.0x1.0 mm³ (192x256x256)	3D MPRAGE, sagittal, R=2, TR/TE/TI=2000/2.0/880 ms	1	1,832
FLAIR	5:50	1.0x1.0x1.0 mm³ (192x256x256)	3D SPACE, sagittal, R=2, PF=7/8, TR/TE/TI=5000/394.0/1800 ms	1	1,832
SWI	2:15	0.8x0.8x3.0 mm³ (252x288x48)	2D axial, R=2, PF=7/8, TR/TE1=24.0/9.42 ms	1	1,830
DWI	9:45	1.75x1.75x1.75 mm³ (118x118x84)	2D axial, MB=3, R=1, PF=6/8, TR/TE=3540/75.0 ms, fat sat, b=0 s/mm² (8PA +8AP), b=300 s/mm² (8), b=1000 s/mm² (32), b=2000 s/mm² (60)	116	1,823
rs-fMRI	14:58	2.4x2.4x2.4 mm³ (88x88x66)	2D axial, EPI, MB=6, TR/TE=850/35.0 ms, flip angle=56°, fat sat	1,058	1,814

Image anonymization

In order to protect the anonymity of the participants, the high-resolution anatomical images (T1 and FLAIR) were processed with a defacing pipeline that masked out voxels in the facial region. This pipeline is a Nipype implementation of defacing protocol used by the UKB (Alfaro-Almagro et al., 2018), and uses the same face mask in MNI space available at the official code repository of the UKB (under templates folder in https://git.fmrib.ox.ac.uk/falmagro/UK_biobank_pipeline_v_1/tree/master).

T1 and T2-FLAIR structural pipeline

Our structural pipeline processed T1 and FLAIR images for multi-channel volume- and surface-based morphometry, primarily with SPM12 (https://www.fil.ion.ucl.ac.uk/spm/) and Freesurfer v6.0 (http://surfer.nmr.mgh.harvard.edu/). It also produced bias-field corrected and 'cropped' T1 images with reduced amount of non-brain tissues to be used as a reference image for all other modalities. Details of the proposed dual structural pipelines are described in the Supplementary Material, with the schematic representation of the pipeline in Supplemental Figure 1. Of note, we had initially used default parameters for SPM12-based unified tissue-segmentation and normalization of the structural images, using the cohort-specific template; however, the early visual QC of the tissue segmentation outputs revealed wrong cortical ribbon extraction leading to a underestimation of grey matter in the vast majority of participants (Supplemental Figure 2 and 3). We therefore modified the SPM12 default settings to overcome this grey matter underestimation, as described in detail in the Supplementary Material.

Global IDPs derived with this pipeline were: total grey matter volume (GM) and white matter volume (WM), mean cortical thickness (CT), total cortical inner surface defined by grey-white matter interface (inner CSA), and total cortical pial surface area (pial CSA). Although only explicitly discussed in a few surface-based morphometric studies (e.g. Hogstrom et al., 2013; Storsve et al., 2014; Tamnes et al., 2017), CSA is usually defined at the GM/WM boundary, representing inner, white surface, since the pial surface defined by the GM/cerebrospinal fluid (CSF) boundary in theory may be more sensitive to changes in CT (Winkler et al., 2012). Here, to thoroughly describe the age-related variation in GM morphometry, we also computed the total pial surface area. Distributions of these metrics in the entire sample (N = 1,832) are shown in Supplemental Figure 15. Overall, the IDPs from this pipeline include:

- 3 global Freesurfer surface-based IDPs (mean CT, total inner CSA, total pial CSAl)
- 1,390 regional Freesurfer surface-based IDPs (CT, inner CSA, pial CSA, number of vertices, and cortical volume for right and left cortical regions as defined by three cortical atlases included with Freesurfer package: Desikan-Killiany (34 regions: Desikan et al., 2006), DKT (31 regions: Klein and Tourville, 2012), and Destrieux (74 regions: Destrieux et al., 2010) cortical atlases)
- 31 global Freesurfer volume-based IDPs (17 global measures of volume contained in 'aseg. stats' table, 14 of which are described in https://surfer.nmr.mgh.harvard.edu/fswiki/MorphometryStats, plus 17 additionally calculated global measures of volume based on 'aseg' segmentation, as described in Supplementary Material)
- 34 regional Freesurfer volume-based IDPs (volumes for each region in 'aseg' labels, but excluding 7 ventricular regions that are aggregated in one of the global measures)
- 5 Freesurfer brainstem substructure volume IDPs (medulla oblongata, pons, superior cerebellar peduncle, and whole brainstem: Iglesias et al., 2015b)
- 26 Freesurfer hippocampal subfield volume IDPs (left/right parasubiculum, presubiculum, subiculum, cornu ammonis (CA) 1, CA2/3, CA4, granule cell and molecular layer of the dentate gyrus (GC-ML-DG), molecular layer, HATA, fimbria, hippocampal tail, hippocampal fissure, and whole hippocampus: Iglesias et al., 2015a)
- 3 tissue volume IDPs from SPM (total GM, WM, and CSF volumes)
- 138 regional GM volume IDPs based on SPM (total GM volume within regions defined by Harvard-Oxford cortical and subcortical atlases (Desikan et al., 2006; Frazier et al., 2005; Goldstein et al., 2007; left/right 48 cortical and 7 subcortical regions, and brainstem: Makris et al., 2006), and by Diedrichsen probabilistic cerebellar atlas (27 regions: Diedrichsen et al., 2009)

Fieldmap generation pipeline

As in the UKB (Alfaro-Almagro et al., 2018), we estimated the fieldmap images from the b=0 images with opposing AP-PA phase-encoding directions from DWI scans, rather than from "traditional" fieldmaps based on dual echo-time gradient-echo images. The Supplementary Material section describes the details of this pipeline, with the schematic representation of the pipeline in Supplemental Figure 5. The main outputs are: 1) the fieldmap phase and magnitude images in native T1 structural space that are used for EPI unwarping in the rs-fMRI pipeline; 2) the acquisition parameters, the field coefficient image and top-up movement parameters, and the brain mask generated from the average distortion-corrected b0 maps that are used for eddy-current and top-up distortion corrections in the DWI and rs-FMRI pipelines. This pipeline was built primarily using tools available

from FMRIB Software Library (FSL, v5.0.10: https://fsl.fmrib.ox.ac.uk).

Diffusion MRI pipeline

The preprocessing steps of DWI are described in the Supplementary Material section, and the Supplemental Figure 6 shows the schematic representation of the pipeline. Briefly, following the eddy current and top-up distortion correction and denoising of the DWI data, the resulting image was then used to fit 1) DTI (Diffusion-Tensor Imaging; Basser et al., 1994) modelling and 2) microstructural model fitting with NODDI (Neurite Orientation Dispersion and Density Imaging; Zhang et al., 2012). The preprocessing and DTI fitting was performed using tools from FSL and the *dipy* package (0.12.0, https://dipy.org; Garyfallidis et al., 2014), while the AMICO (Accelerated Microstructure Imaging via Convex Optimization) tool (Daducci et al., 2015) was used for NODDI fitting. Here we report global DTI/NODDI statistics measured for each individual within a cerebral WM mask defined using the Freesurfer-segmented WM further refined using the SPM12-based WM probability map with a 0.5 lower threshold. This masking procedure ensured that the mean DTI/NODDI values were computed within cerebral WM regions with limited partial volume effects.

The global IDPs from this pipeline that are reported in this paper are mean DTI and NODDI metrics within the cerebral WM mask. Specifically, these metrics are: fractional anisotropy (FA), mean, axial, and radial diffusivity (MD, AD, and RD), based on DTI modeling, neurite density index (NDI), orientation dispersion index (ODI), and isotropic volume fraction (IsoVF), derived from NODDI modeling. Distributions of these metrics in the entire sample with complete DWI data (N = 1,823) are shown in Supplemental Figure 16. Figure 3 shows the group average maps of these DTI and NODDI metrics in standard MNI space. The following list summarizes these and other IDPs from this pipeline, and the Supplementary Material describes how they were generated:

- 77 DTI/NODDI regional WM IDPs based on subject-specific masks generated using Freesurfer aseg labels (mean FA, MD, AD, RD, NDI, ODI, IsoVF within total and left/right cerebral, cerebellar, and ventral diencephalon WM, and within corpus callosum and brainstem)
- 28 DTI/NODDI regional GM IDPs based on subject-specific masks generated using Freesurfer aseg labels (mean DTI/NODDI metrics within cortical, hippocampal, subcortical (excluding hippocampi), and cerebellar GM)
- 525 DTI/NODDI regional WM IDPs based on subject-specific masks generated using Freesurfer wmparc labels (mean DTI/NODDI metrics within 75 WM parcellated regions of the wmparc atlas (5 corpus callosal subregions and 35 left/right WM regions: Salat et al., 2009)
- 336 DTI/NODDI regional WM IDPs based on spatially normalized DTI/NODDI maps and JHU ICBM-DTI-81 white matter labels atlas (6 bilateral and 21 left/right WM tracts: Mori et al., 2008; Oishi et al., 2008)
- 36 DTI global WM skeleton IDPs based on spatially normalized WM skeleton created using TBSS (Tract-Based Spatial Statistics, Smith et al., 2006), part of FSL package (Smith et al., 2004) (mean, standard deviation, and peak-width 90 of the skeleton, or the 95th to 5th percentile value over the WM skeleton, as described in Baykara et al. (2016) for the 4 DTI metrics, as well as the same metrics computed over the left and right WM skeletons, as described in Beaudet et al. (2020))

Resting-state fMRI pipeline

Processing of rs-fMRI is described in the Supplementary Material section, with the Supplemental Figure 7 showing the schematic representation of the preprocessing steps. Briefly, the distortion-corrected rs-fMRI data were aligned to the T1-weighted individual reference space, band-pass filtered to a frequency window of 0.01 - 0.1 Hz, then warped into the stereotaxic space at a voxel sampling size of 2x2x2 mm^3. These preprocessing steps were primarily performed using tools from FSL (v5.0.10: https://fsl.fmrib.ox.ac.uk) and AFNI (v18.0.05: https://afni.nimh.nih.gov, Cox, 1996). The following IDPs were then generated (details in the Supplemental Material) from the preprocessed data:

- 2 regional intrinsic connectivity (IC) matrices using the 384 regions of the AICHA atlas (Atlas of Intrinsic Connectivity of Homotopic Areas; Joliot et al., 2015), either with or without global signal removal;
- A ReHo map (Zang et al., 2004) that measures the homogeneity of local connectivity;
- An ALFF map that depicts the local amplitude of low frequency fluctuations (Yang et al., 2007)
- A map of fALFF (Zou et al., 2008), a normalized value of ALFF that improves sensitivity and specificity in detecting intrinsic brain activities;
- subject-specific IC components and their time series based on subject-level independent component analysis (ICA; Beckmann and Smith 2004).

Quality control

Overview of the QC strategy

The quality of acquired MR images and phenotypes obtained from them was ensured by a 5-stage quality control processes (Figure 2) : 1) Aborting or postponing the MRI scan during acquisition if the MR technician observes significant amount of artefacts due to motion or any technical problems;

2) Reviewing of acquired structural scans (T1 and FLAIR) by experts to check for any significant artefact or presence of anomalies (see the section on Incidentals and anomalies above, and see Supplemental Figure 8 for examples of the flagged artefact); 3) Generation and reviewing of modality- and processing-specific QC images for each participant, organized as static web-pages (Supplementary Material for description and examples from each pipeline); 4) Examination of the distributions of both QC metrics and IDPss for detection of outliers using interactive web-based figures with links to subject-specific QC web-pages (Supplementary Material for the description and distributions of IDPs and quantitative QC metrics for each pipeline); and finally 5) Detailed review of relevant raw and processed data when the images were flagged as having visible artefact or benign anomalies (i.e. not classified as incidentals) in step 2 or when any metrics computed in step 4 indicated potential problems in specific processing pipeline (e.g. review of tissue segmentation images for individuals with visible artefacts, known structural anomaly, or outlier values in specific morphometric values).

Since the structural scans, in particular T1 image, serve as a reference for all other modalities, we paid additional attention at checking the quality of their acquisition and processing, subjecting them to more individual individual-level QC review at step 2, in addition to the thorough review of raw acquired data at step 1. This is also because it is relatively easier to spot processing errors more objectively in the structural processing (e.g. segmentation failures) in individual-level QC images than in the DWI and rs-fMRI pipelines, where the accuracy of final output images cannot be easily assessed visually. However, whenever the group-level QC metric distributions indicated potential problems in the specific processing pipeline, individual-level QC images in the DWI and rs-fMRI pipelines were reviewed to check for any obvious problems in image quality and/or processing error. No manual editing or subject-specific parameter adjustment was performed for any of the pipelines, in order to ensure the repeatability of our results. In this paper, we primarily use the distribution of phenotypic variables of interest to define the outliers to be excluded in the analyses. Specifically, we checked for extreme outliers in each phenotypic variables using interquartile range (IQR), or Tukey fence method (Tukey, 1977), defining those with values below 3*IQR from the first quartile or above 3*IQR from the third quartile as the “far out” outliers. The distributions of

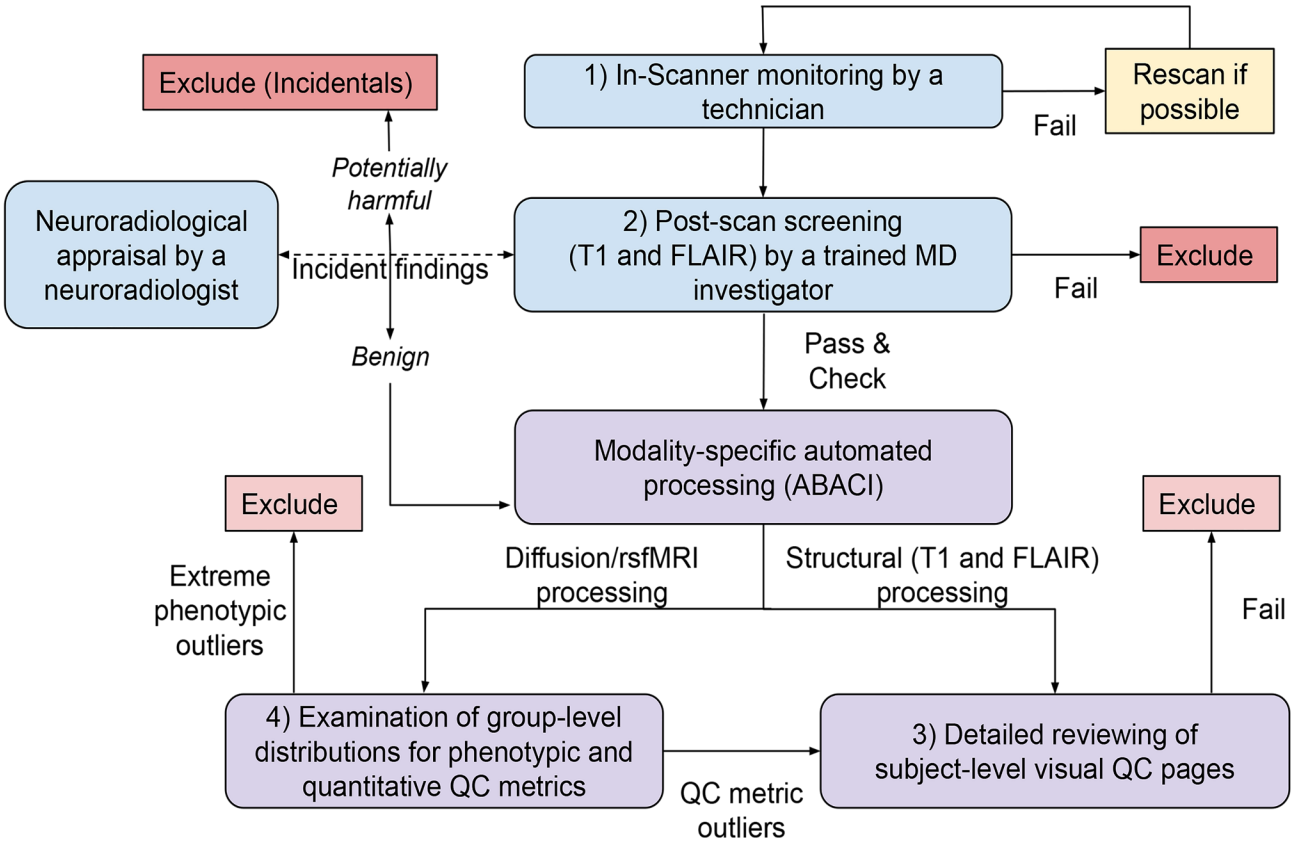

Figure 2. Overview of the QC workflow. Boxes in light blue represent QC steps that deal with raw data during and after acquisition, and those in light purple represent QC steps that use processed images via automated processing pipelines. While all MRI data from subjects with incidental findings were excluded (dark pink), those with processing-specific problems were excluded only from relevant analyses (light pink). Since the structural images, in particular T1 scans, served as a reference in other processing pipelines, those with severe artefacts in raw T1 images were removed from all analyses. The flowchart is loosely based on Backhausen et al. (2016), who described a recommended QC workflow for structural (T1) processing.

all the quantitative QC metrics are reported in the Supplementary Material.

Summary of modality-specific QC criteria and excluded participants

Structural pipeline

A total of 19 participants were flagged as having visible artefacts in raw T1 and/or FLAIR images by one of the three MD experts who reviewed raw images soon after the acquisition (step 2). However, none of the images had artefacts severe enough to exclude participants immediately (see Supplementary Material for the rating of artefact severity), partly because the first step in our QC protocol prevented unusable data from entering the database. We followed the recommendations and procedures proposed by (Backhausen et al., 2016), to carefully follow the impact of these flagged artefacts at each step of the structural processing, and found that all of the flagged images could be processed without any major issues. For structural pipeline, an independent trained rater (N.B) also reviewed subject-specific QC images generated from both SPM12 and Freesurfer streams for all participants, regardless of the artefact flagging, and found all 1,832 participants to have acceptable processing of T1 and FLAIR images, at least with regard to global morphometry reported here. The Supplemental Material Figure 15 shows the distributions of all the global morphometric variables we report in the current paper (CT, inner CSA, pial CSA, GM and WM volumes). None of these variables had extreme outliers in the entire sample (N = 1,832), nor in those under 26 years old (N = 1,722), who were used to examine the age and sex effects in the current paper. While most of the QC for the structural pipeline was performed by visual inspection of various images, we also computed some quantitative QC metrics and report their distributions in the Supplemental Figure 11.

Diffusion pipeline

For the diffusion pipeline, 9 participants had either missing or incomplete DWI scans due to technical problems or anxiety attacks, resulting in a total of 1,823 DWI data that could be processed. A number of quantitative QC metrics were reviewed for any outliers, and subject-specific visual QC images were reviewed by experts (L.P and A.T) for those outliers to detect any obvious problems with the quality of the acquired DWI or with any specific processing steps (see Supplementary Material for details for the distributions of all the quantitative QC metrics), but none was detected. There were also no extreme outliers in any of the mean DTI and NODDI metrics within the cerebral WM in the entire sample (N = 1,823), nor in those under 26 years old (N = 1,714).

Resting-state fMRI pipeline

The rs-fMRI scan, which was the last of the MRI session, was either missing or incomplete in 17 participants. One additional participant was found to have a wrong parameter for TR, and subsequently removed from the analysis. As a result, there was a total of 1,814 data that could be processed in the pipeline. Similarly to the diffusion pipeline, the QC for the resting-state fMRI focused on the identification of outliers on a number of quantitative QC metrics automatically generated by the pipeline, followed by the reviewing of subject-specific QC images by experts (M.J and M-F.G) to determine the acceptability of the data (see Supplementary Material for details for the distributions of all the quantitative QC metrics).

Statistical Analysis

MRi-Share study protocol

While the primary goal of the present manuscript is to describe the MRi-Share image acquisition protocol as well as the analysis pipelines used for deriving brain phenotypes from MRI, a secondary goal is to present preliminary results on associations of some of these brain image-derived phenotypes (IDP) at the whole brain level with both age and sex in yound adults.

As mentioned earlier, the vast majority of MRi-Share participants are aged between 18 and 26 years, with only about 5% being aged between 26 and 35 years. Rather than making an inference about age-related variations for the age-range of the entire sample that would rely on a small number of participants for the later age range, we focus here on the earlier age range of 18 to 26 years old where we have good coverage of the age span. Given the narrow target age range, we expected most of the age-related variations that exist in the IDPs to be captured by a linear age model. Indeed, preliminary comparison of models that included quadratic age effect to capture any non-linear trend did not improve model fit relative to linear age effect models in any of the IDPs examined, as judged by the Bayesian Information Criterion (BIC). Also using BIC, we examined linear age models with or without including the estimate of intracranial volume (eTIV) from Freesurfer as a covariate for the structural morphometric analyses, to check for the significant contribution of the eTIV in explaining the variance of the IDPs. For the mean DTI and NODDI metrics within cerebral WM, instead of eTIV, we examined the contribution of the volume of the cerebral WM mask as the latter has been shown to modulate the estimated DTI mean values by affecting the amount of partial volume effects (PVE) within the mask (Vos et al., 2011). We certainly minimised the PVE by restricting the mean metric computation in the Freesurfe WM mask voxels

having a WM tissue probability larger than 0.5. Nevertheless, including PVE as a covariate in the statistical analysis allowed us to verify that any residual PVE did not affect the estimates for the age effect.

Given the large disparity in the sample size of each sex, we studied age effects first separately for men and women first, then as acombined group to test for the main effect of sex as well as any interaction between sex and age. Thus, for sex-specific analyses, we examined two models as described in the following equations:

$$Y \sim A + \beta_{Age} Age \quad (1)$$
$$Y \sim A + \beta_{Age} Age + \beta_{Vol} Vol \quad (2),$$

where *Vol* represents eTIV for the structural morphometry IDPs and the cerebral WM mask volume for the DTI and NODDI IDPs. Comparing these two models, we primarily report the model showing optimal fit, i.e. having the lowest BIC. For the combined group analyses, the following two models were considered:

$$Y \sim A + \beta_{Sex} Sex + \beta_{Age} Age + \beta_{Sex:Age} Sex{:}Age \quad (3)$$
$$Y \sim A + \beta_{Sex} Sex + \beta_{Age} Age + \beta_{Vol} Vol + \beta_{Sex:Age} Sex{:}Age + \beta_{Sex:Vol} Sex{:}Vol \quad (4),$$

and we report the model parameter estimates with (3) or without eTIV or WM mask volume *(4)* when the best fit models for two sexes agreed (which should be chosen if we were to use BIC on the combined group models), and the results with *Vol (4)* when eTIV or the WM mask volume explained a significant amount of variance in at least one of the sexes. This was to avoid biasing the model selection for the combined group towards the larger sample size female group, when the selected model differs between the two sexes. Similarly, in the model *(4)*, we included a *Sex* by *Vol* interaction in the model to allow for a possible difference between the groups in the slope of the IDPs versus Vol, again avoiding biasing the fit towards the larger female group (Nordenskjöld et al., 2015). The interaction term with *Sex* and *Age* was included in both models to test for any sex differences in the age-related trajectory.

Both *Age* and *Vol* were mean-centered in respective groups (i.e. using female- or male-specific means in sex-specific analyses and combined mean in combined group analyses). Our aim in presenting these analyses is to describe the overall age trajectory of these global metrics inferred from the age-related variations in our dataset, rather than to test any specific hypotheses. Thus, we present the raw model fits with unadjusted *p*-values. Although we primarily report the results of the model selected by the procedure described above, we also provide the alternative model results in the Supplementary Material, given the inconsistencies in how global brain size is corrected (or not corrected) in prior studies investigating brain morphometric changes during development and maturation (e.g. Table 2 in a recent review by Vijayakumar et al., 2018). As for the DTI and NODDI IDPs, the effects of the mask volume during development are largely unknown.

All model fits were performed using *lm* function as implemented in *stats* library included with R version 3.4.4 (R Core Team, 2018), and the effect size estimates for each covariate in the model were computed as partial η^2 using '*etasq*' function in the R *heplots* library (Fox et al., 2018). BIC was computed using the '*extractAIC*' function in the R stats package, with the weight of the equivalent degrees of freedom (k) set to log(n), where n represents the sample size in the mode. In the combined-sex analyses, we report the estimates of β's for sex and sex interaction terms using the default contrast setting in R that treats one of the groups (female in our case) as a reference, so that the β represents the difference between male and female groups. However, to present the age effect across groups, we report β for age effect by setting the contrast to 'contr.sum', that gives orthogonal contrasts where the effect estimates for non-categorical variables (i.e. age in our case) represent those for the overall group mean.

Results

Figure 3 and 4 illustrate the spatially normalized average maps of various morphometry and white matter property IDPs across the entire MRi-Share sample (N = 1,832 for Figure 3, N = 1,823 for Figure 4). Figure 3A and B show the sample average images of spatially normalized T1 and FLAIR. Figures 3C, D, and E depict the vertex-level sample average of CT, inner CSA and pial CSA computed in the *fsaverage* surface-based template space. Figures 3E and 3F show the sample average GM and WM tissue probability maps and Figure 4 the sample average DTI and NODDI maps.

Global grey matter morphometry

Table 3 summarizes the descriptive statistics and the age and any sex differences in the three global cortical GM morphometry: Freesurfer-based mean CT, total inner CSA, total pial CSA, and SPM-based total GM volume, the latter being calculated from jacobian modulated and warped GM maps. The age and sex effect estimate on these metrics are also reported in Table 3 and plotted on Figure 5 for surface-based metrics, and Figure 6A for GM volume.

The best model for the mean CT was the model without eTIV in both sexes, which explained 0.1 and 1.0% of total variance in male and female data, respectively. In the combined group analysis, age, sex, and their interaction together explained 2.5% of the variance. There was a significant main effect of sex, with males showing slightly thicker CT than females (approximately 0.8% difference in CT).

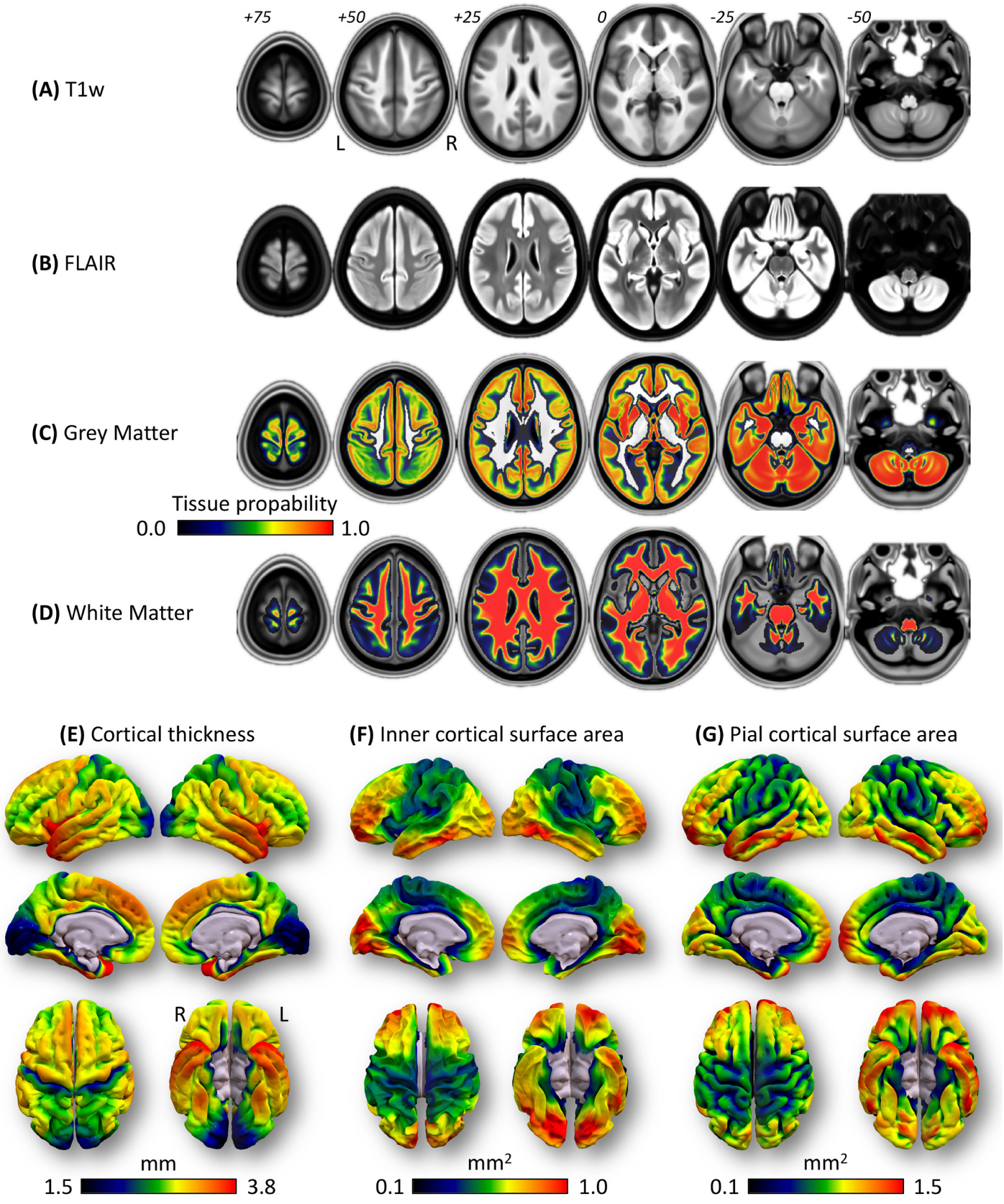

Figure 3. Group average maps for structural images for 1,832 MRi-Share subjects. Average maps across subjects are shown for (A) T1, (B) FLAIR, (C) mean CT, (D) total inner CSA, (E) total pial CSA , (F) GM tissue map, and (G) WM tissue map. Volumetric images (A, B, F, G) are spatially normalized and in standard MNI space. The tissue probability maps (F and G) are overlaid on the average T1 image, and the color bar at the bottom indicates the group average tissue probability. All volumetric maps were with the MRIcron (v1.0.20190902; https://people.cas.sc.edu/rorden/mricron/). Surface-based metrics (C to E) are projected onto *fsaverage* template space, with (C) and (E) projected onto pial surface, and (D) onto white surface of the template, visualized using the Suf Ice (v1.0.20190902; https://www.nitrc.org/projects/surfice/).

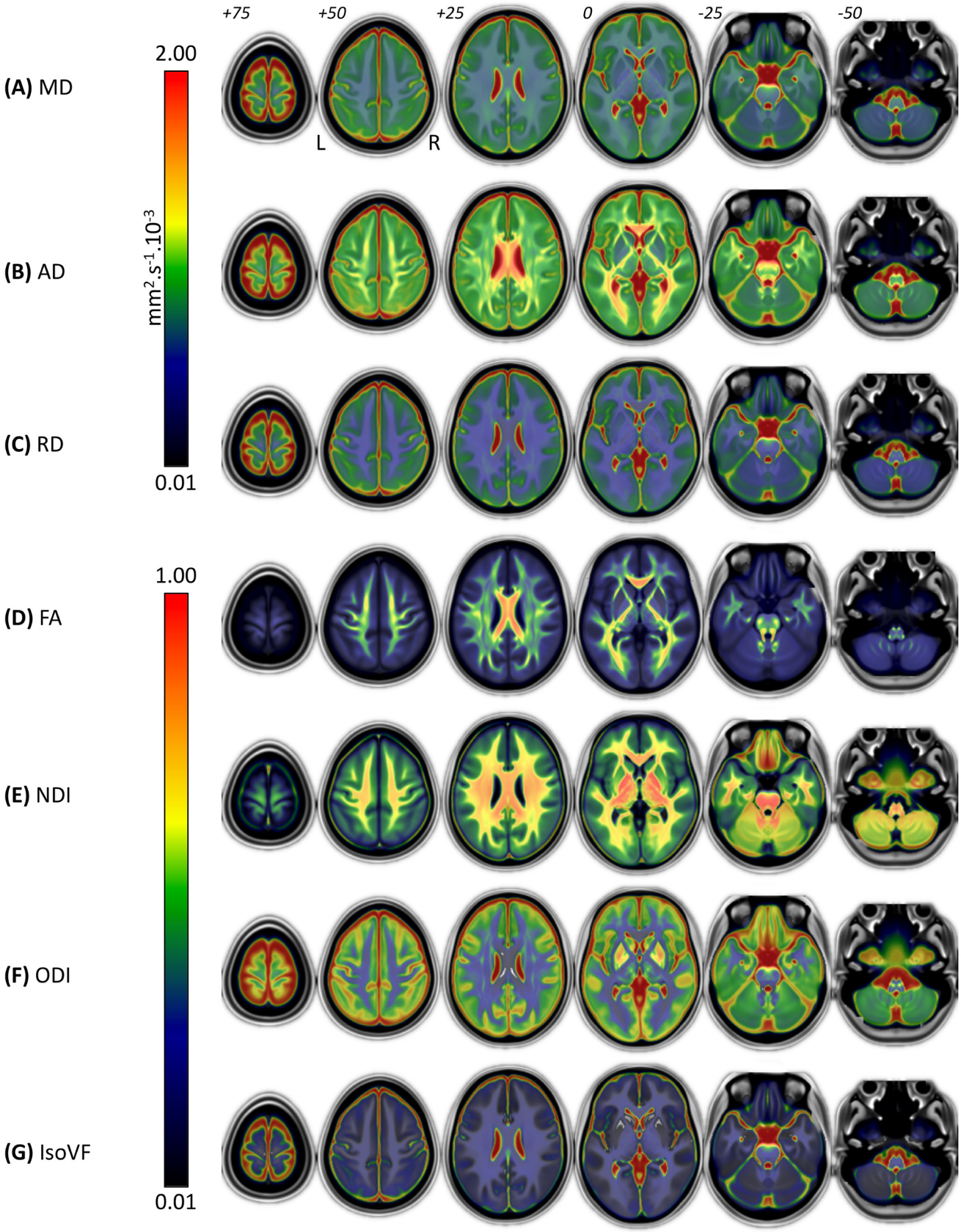

Figure 4. Group average maps for DTI and NODDI metrics in 1,823 MRiShare subjects. Average maps of (A) FA, (B) MD, (C) RD, and (D) AD from the DTI modeling, and (E) NDI, (F) ODI, and (G) IsoVF from the NODDI modeling across subjects are shown in the standard MNI space. Colorbar for the FA, NDI, ODI, and IsoVF is shown at the left-bottom, and that for the MD, RD, and AD is shown at the right-bottom of the figure. All maps were visualized with the MRIcron (v1.0.20190902; https://people.cas.sc.edu/rorden/mricron/).

Table 3. Summary of grey matter morphometry. Descriptive statistics and the results of linear model fit for mean CT, total inner CSA, and total pial CSA from Freesurfer v6.0, as well as total GM volume from SPM12, are shown. Parameter estimates (β) for age and sex are shown, together with 95% confidence intervals (CI) for each β, as well as uncorrected p values and partial eta squared as the effect sizes for each variable. The Model column indicates the selected model (see text) with the corresponding model number as described in Methods section. The interaction between sex and age was tested in the combined group but was not significant in any of the metrics listed here, and thus is not included in the table. The variance explained by eTIV for models that included it is discussed in the text. Overall model fit is indicated as adjusted squared R values.

				Age			Sex (M>F)			
	N	Mean ± SD [min, max]	Model	β [95% CI]	*p*	Partial η^2	β [95% CI]	*p*	partial η^2	adj-R^2
CT		(mm)		($x10^{-3}$ mm/yr)			($x10^{-3}$ mm)			
Males	470	2.86 ± 0.08 [2.60, 3.10]	(1)	-2.49 [-6.47, 1.49]	0.22	0.003	--	--	--	0.001
Females	1252	2.84 ± 0.07 [2.61, 3.11]	(1)	-4.58 [-6.96, -2.19]	$1.7x10^{-4}$	0.011	--	--	--	0.010
Combined	1722	2.84 ± 0.08 [2.60, 3.11]	(3)	-3.53 [-5.77, -1.29]	0.0020	0.008	23.7 [15.6, 31.8]	$1.0x10^{-8}$	0.019	0.025
inner CSA		($x10^5$ mm²)		($x10^2$ mm²/yr)			($x10^2$ mm²)			
Males	470	1.86 ± 0.14 [1.48, 2.30]	(2)	-4.01 [-7.53, -0.11]	0.026	0.011	--	--	--	0.738
Females	1252	1.68 ± 0.12 [1.31, 2.22]	(2)	-1.63 [-3.53, 0.27]	0.093	0.002	--	--	--	0.767
Combined	1722	1.73 ± 0.15 [1.31, 2.30]	(4)	-2.82 [-4.67, -0.97]	0.0029	0.004	-12.9 [-22.6, -3.2]	0.0086	0.006	0.826
pial CSA		($x10^5$ mm²)		($x10^2$ mm²/yr)			($x10^2$ mm²)			
Males	470	2.27 ± 0.16 [1.84, 2.73]	(2)	-7.23 [-11.2, -3.25]	$3.9x10^{-4}$	0.027	--	--	--	0.746
Females	1252	2.05 ± 0.14 [1.60, 2.62]	(2)	-4.33 [-6.55, -2.11]	$1.3x10^{-4}$	0.012	--	--	--	0.768
Combined	1722	2.11 ± 0.18 [1.60, 2.73]	(4)	-5.78 [-7.92, -3.65]	$1.2x10^{-7}$	0.016	-5.5 [-16.6, 5.6]	0.33	0.002	0.832
GM		(cc)		(cc/yr)			(cc)			
Males	470	730.6 ± 54.7 [598.9, 912.8]	(2)	-2.03 [-3.22, -0.84]	$9.0x10^{-4}$	0.023	--	--	--	0.808
Females	1252	659.0 ± 48.9 [495.4, 824.1]	(2)	-2.38 [-3.10, -1.65]	$2.1x10^{-10}$	0.032	--	--	--	0.785
Combined	1722	678.5 ± 59.8 [495.4, 912.8]	(4)	-2.20 [-2.88, -1.52]	$2.9x10^{-10}$	0.029	-7.0 [-10.6, -3.5]	$1.0x10^{-4}$	0.009	0.851

A significant decrease in mean CT with age was observed in females and in the combined group. In males, mean CT also decreased with age but not significantly, but there was no significant interaction between the age and sex on mean CT (Table 3, Figure 5A and Supplementary Table 1). Strictly speaking, the observed age effects are age-associated variations in this cross-sectional cohort, but assuming they represent the age-related changes at this age range, the observed change represents annual percent change (APC) of roughly -0.16% in females and -0.12% in the combined group.

Contrary to its absence of effect on mean CT, eTIV significantly impacted the other GM morphometrics (inner CSA, pial CSA, and GM volume, all p's $< 2 \times 10^{-16}$) and explained a large amount of the variances of these data (over 76% for all, based on partial η^2 values for eTIV in combined group analyses). None of these metrics showed any significant interaction between sex and eTIV (all p's > 0.36), indicating similar effects of eTIV on these measures across sexes. Thus, below we report age and sex effects for these metrics based on the model including eTIV (model (2) for sex-specific analyses and (4) for combined analyses).

Proportions of age-related variance in inner CSA were similar to those of CT, explaining only 1.1, 0.2, and 0.4% in males, females, and combined groups, respectively. In contrast to CT, the age effect on inner CSA was significant in males (p = 0.026) and in the combined group (p = 0.0029) but did not reach significance in females (p = 0.093).

As for CT, the estimated effects were consistently negative, representing an APC of about -0.2% in males and the combined group, and there was no detectable difference in the age trajectory between males and females (p = 0.21). Although raw values of inner CSA were larger in males compared to females, the difference was actually slightly but significantly reversed in the model with eTIV (0.7% larger in females than in males, p = 0.008).

Unsurprisingly, inner CSA and pial CSA were highly correlated in our dataset (pearson correlation r = 0.986, Supplemental Figure 16), and the total variance of pial CSA data explained by the models with eTIV was similar to those of inner CSA (over 74% in all cases). Yet, observed age-related variances for pial CSA were consistently higher than for inner CSA or CT data (2.7, 1.2, and 1.6% in males, females, and combined data). There were significant age effects in both sex-specific and combined analyses, with the estimated effects representing APC of about -0.2 to -0.3%. In the analysis that combined both sexes, no interaction between sex and age was detected. Similar to what was observed for inner CSA, the pial CSA was larger for males compared to females, but the difference was reversed non-significantly when eTIV was included in the model (0.2% larger in females than

in males; p = 0.33; Table 3 and Supplemental Table 1).

The total variance of GM volume explained by age, eTIV, and sex in the case of sex-combined analysis was slightly higher than for CSA data (over 78% in all cases), and the age-related variance in GM volume tended to be higher than CT or CSA data individually (2.3, 3.2, and 2.9% in male, female, and combined data). The total GM volume significantly decreased with age in all comparisons (p's < 9.0×10^{-4}), representing an APC of approximately -0.3%. Again there was no detectable difference in age-related reduction between males and females (p = 0.61). Not surprisingly, males had larger total GM than females when not taking into account the overall head size. When eTIV was taken into account, females showed about 1% larger volume than males ($p = 1.0 \times 10^{-4}$; Table 3).

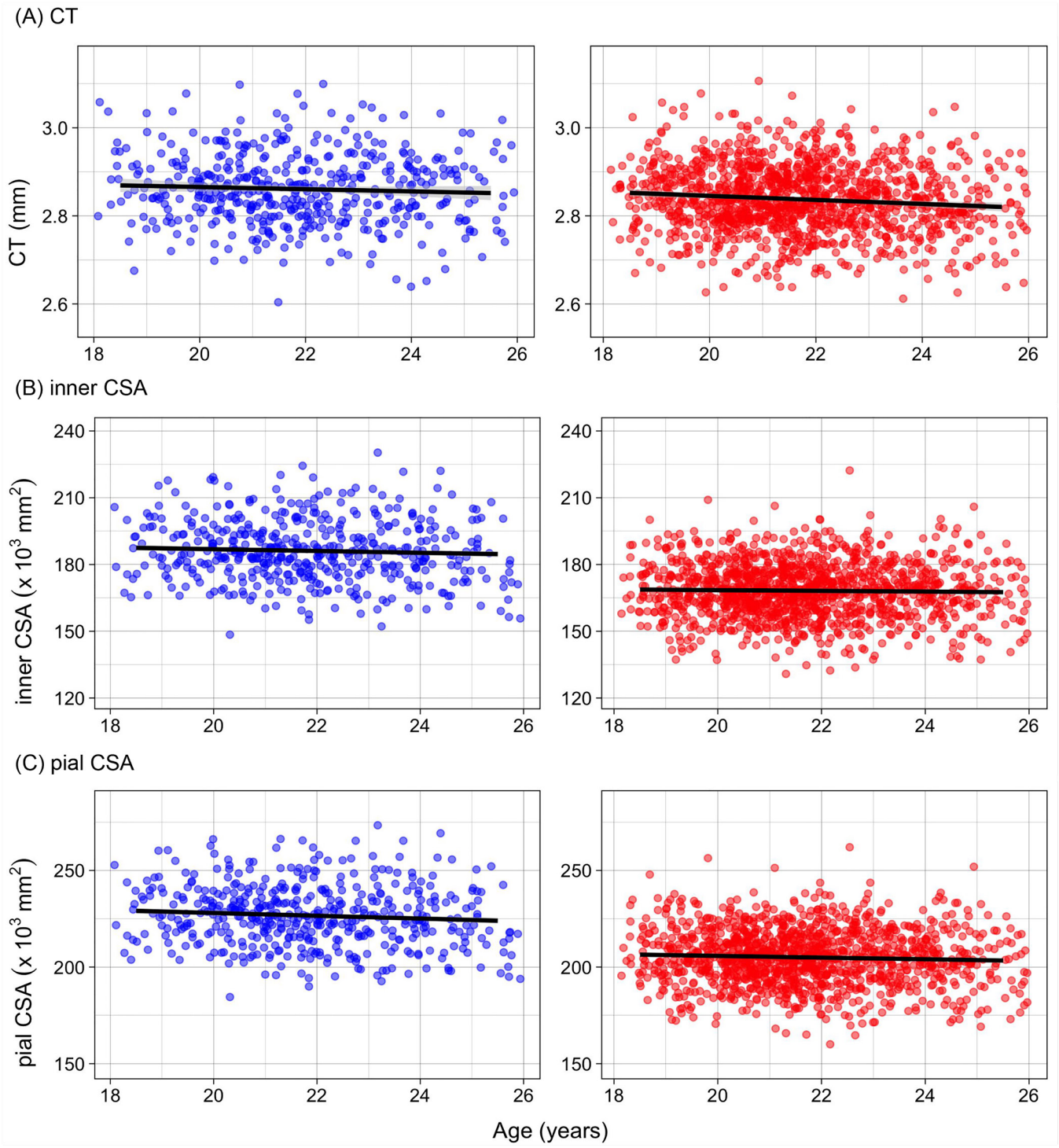

Figure 5. Age-related variations in surface-based morphometry. (A) The mean CT, (B) total inner CSA, and (C) total pial CSA are plotted against age, with individual subjects represented as scatter points (left panel: male, right panel: female). For each sex, predicted age trajectories, based on the model selected by BIC (see text) in the sex-specific analyses are shown. The plots in the right panel show predicted trajectories for hypothetical male or female subjects with identical, global mean eTIV, based on combined group analyses. The 95% confidence intervals of the predictions are represented as shades around the line.

Global white matter morphometry and DTI parameters

Table 4 provides the descriptive statistics of the following metrics of white matter: total WM volume and mean values of DTI metrics. The table also contains a summary of age and sex effects on these metrics, which are also visually presented in Figure 6B for WM volume, and Figure 7 for mean DTI metrics.

Like for CSA and GM volume data, eTIV explained a large portion of variance in the WM volume data (over 83% in all cases). Of note, unlike in GM morphometric data, there was a significant interaction between sex and eTIV ($p = 4.1x10^{-4}$), with males showing steeper slope than females for the effect of eTIV on WM volume. There was a positive and significant linear effect of age on the WM volume in both sexes (Table 4, Figure 6B and Supplemental Table 2), with an APC of about 0.2%. There was no detectable sex differences on age trajectory, and age accounted for 1 to 2% of total variance in the WM volume data. As in GM morphometric data, the sex difference in WM volume was non-significant with the inclusion of eTIV in the model ($p = 0.35$).

Like for CSA and GM volume data, eTIV explained a large portion of variance in the WM volume data (over 83% in all cases). Of note, unlike in GM morphometric data, there was a significant interaction between sex and eTIV ($p = 4.1x10^{-4}$), with males showing steeper slope than females for the effect of eTIV on WM volume. There was a positive and significant linear effect of age on the WM volume in both sexes (Table 4, Figure 6B and Supplemental Table 2), with an APC of about 0.2%. There was no detectable sex differences on age trajectory, and age accounted for 1 to 2% of total variance in the WM volume data. As in GM morphometric data, the sex difference in WM volume was non-significant with the inclusion of eTIV in the model ($p = 0.35$).

Overall, the cerebral WM mask volume used to compute DTI mean values did not influence the estimate of age effects on these mean values, and the BIC index indicated that the mask volume contributed little to the overall fit in most comparisons. The only exceptions were the mean MD and RD values in males, where diffusivity values were positively correlated with the mask volume (with partial η^2 of 0.017 and 0.021 for MD and RD, respectively, representing less than 0.01% increase in diffusivity per cc; p's < 0.005). This, however, did not impact the estimates of age effects, and only slightly affected the sex effect estimates in the combined group analyses. Below we report the results of the selected

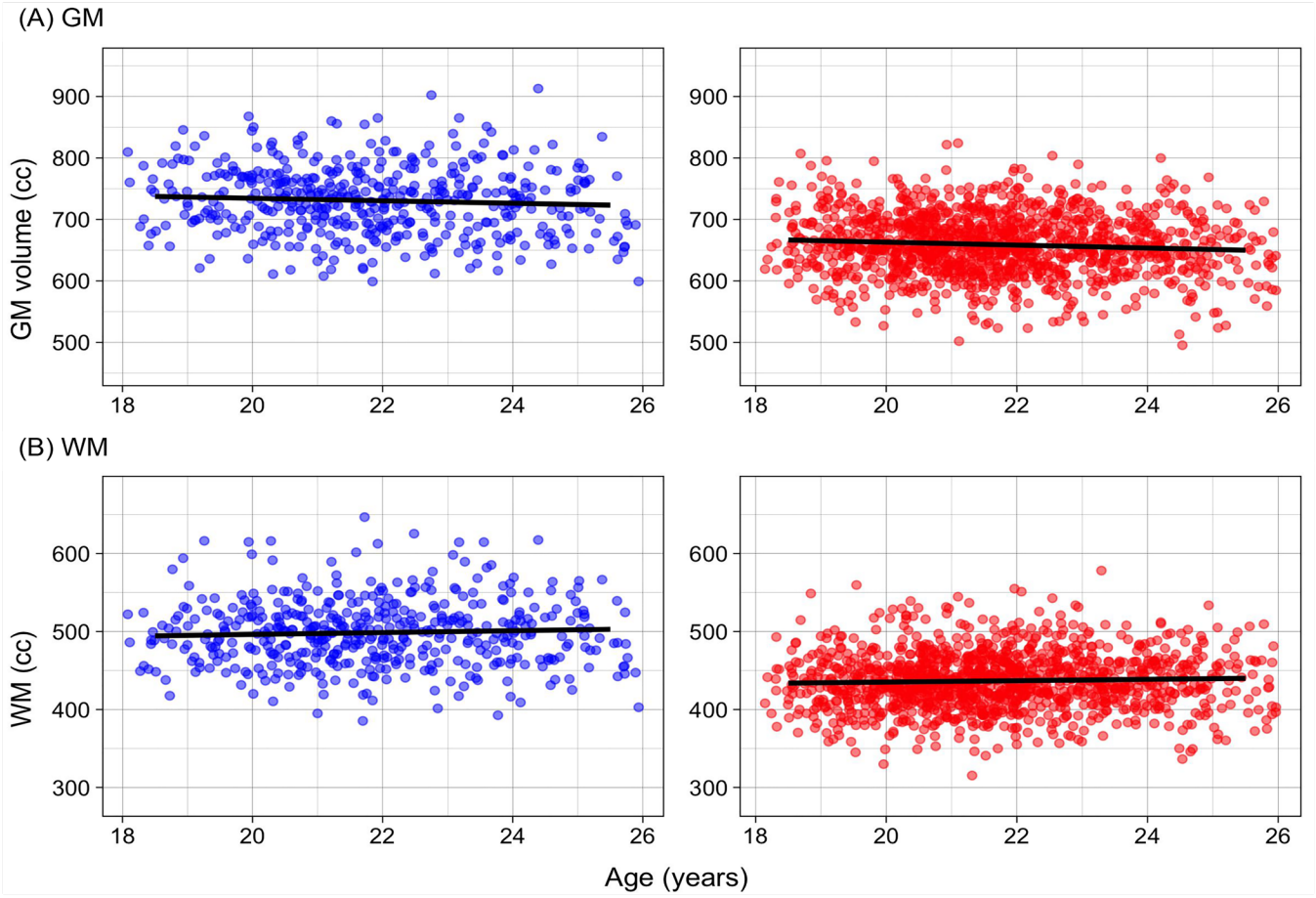

Figure 6. Age-related variations in gray and white matter volumes. (A) The total GM volume, and (B) total WM volume are plotted against age, with individual subjects represented as scatter points (left panel: male, middle panel: female). For each sex, predicted age trajectories, based on the model selected by BIC (see text) in the sex-specific analyses are shown. The plots in the right panel show predicted trajectories for hypothetical male or female subjects with identical, global mean eTIV, based on combined group analyses. The 95% confidence intervals of the predictions are represented as shades around the line.

Table 4. Summary of white matter volume and mean DTI metrics within cerebral white matter. Descriptive statistics and the results of linear model fit for total white matter volume (WM) from SPM12, as well as mean DTI metrics within subject-specific cerebral WM masks are shown. Parameter estimates (β) for age and sex are shown, together with 95% confidence intervals (CI) for each β, as well as uncorrected p values and partial eta squared as the effect sizes for each variable. The Model column indicates the chosen model (see text for details on the model selection), with the corresponding model number as described in Methods section. The interaction between sex and age was tested in the combined group but was not significant in any of the metrics listed here, and thus is not included in the table. The variance explained by eTIV or mask volume for models that included them is discussed in the text. Overall model fit is indicated as adjusted squared R values.

				Age			Sex (M>F)			
	N	Mean±SD [min, max]	Model	β [95% CI]	*p*	partial η^2	β [95% CI]	p	partial η^2	adj-R^2
WM		(cc)		(cc/yr)			(cc)			
Male	470	498.5 ±42.5 [385.3, 646.8]	(2)	1.20 [0.39, 2.99]	0.0036	0.018	--	--	--	0.856
Female	1252	436.6 ±3 5.9 [315.3, 578.2]	(2)	0.87 [0.40, 1.34]	2.8×10^{-4}	0.011	--	--	--	0.834
Combined	1722	453.5 ± 46.8 [315.3, 646.8]	(4)	1.03 [0.59, 1.45]	5.7×10^{-6}	0.013	-1.10 [-3.42, 1.21]	0.35	0.000	0.896
FA				($\times10^{-4}$ /yr)			($\times10^{-4}$)			
Male	468	0.433 ± 0.013 [0.383, 0.466]	(1)	6.97 [0.48, 13.5]	0.035	0.009	--	--	--	0.007
Female	1246	0.433 ± 0.013 [0.390, 0.474]	(1)	2.92 [-1.28, 7.13]	0.17	0.001	--	--	--	0.001
Combined	1714	0.433 ± 0.013 [0.383, 0.474]	(3)	4.95 [1.08, 8.81]	0.012	0.003	-0.85 [-14.8, 13.1]	0.90	0.000	0.002
MD		($\times10^{-4}$ mm²/sec)		($\times10^{-6}$ mm²/sec/yr)			($\times10^{-6}$ mm²/sec)			
Male	468	7.123 ± 0.169 [6.680, 7.755]	(2)	-2.16 [-2.97, -1.35]	2.6×10^{-7}	0.056	--	--	--	0.066
Female	1246	7.126 ± 0.151 [6.577, 7.616]	(1)	-1.46 [-1.94, -0.98]	2.7×10^{-9}	0.028	--	--	--	0.027
Combined	1714	7.125±0.156 [6.577, 7.755]	(4)	-1.82 [-2.27, -1.37]	5.8×10^{-15}	0.036	-2.27 [-4.40, -0.15]	0.036	0.002	0.040
AD		($\times10^{-4}$ mm²/sec)		($\times10^{-6}$ mm²/sec/yr)			($\times10^{-6}$ mm²/sec)			
Male	468	10.75 ± 0.18 [10.17, 11.27]	(1)	-2.54 [-3.41, -1.67]	1.6×10^{-8}	0.066	--	--	--	0.064
Female	1246	10.77 ±0.16 [10.17, 11.32]	(1)	-1.91 [-2.43, -1.40]	6.1×10^{-13}	0.041	--	--	--	0.040
Combined	1714	10.76 ±0.17 [10.17, 11.32]	(3)	-2.23 [-2.71, -1.74]	$<2.0\times10^{-16}$	0.048	-1.06 [-2.82, 0.69]	0.23	0.001	0.049
RD		($\times10^{-4}$ mm²/sec)		($\times10^{-6}$ mm²/sec/yr)			($\times10^{-6}$ mm²/sec)			
Male	468	5.309 ± 0.181 [4.837, 6.038]	(2)	-1.96 [-2.84, -1.09]	1.3×10^{-5}	0.040	--	--	--	0.054
Female	1246	5.306 ± 0.167 [4.780, 5.847]	(1)	-1.24 [-1.77, -0.71]	5.2×10^{-6}	0.017	--	--	--	0.016
Combined	1714	5.306 ± 0.171 [4.780, 6.038]	(4)	-1.61 [-2.11, -1.11]	2.7×10^{-10}	0.023	-2.21 [-4.55, 0.12]	0.064	0.001	0.029

models (i.e. models with mask volume for MD and RD in males and in combined group, and models without mask volume for the rest), but provide the alternative model results in the Supplemental Table 2.

All the diffusivity measures (MD, AD, and RD) showed robust significant decrease with APC of about -0.2% for AD and -0.3% for RD, with MD somewhere in between over the age range of our dataset (all *p*'s ≤ 1.3×10^{-5}; Table 4, Figure 7). FA, by contrast, only showed a trend for increase at this age range that reached significance in the males (p = 0.035) and sex-combined group (p = 0.012), but not in females (p = 0.17). Age accounted for 4.0 to 6.6% of the total variance of the diffusivity metrics (most in AD, least in RD) in males, and 1.7 to 4.1% in females, and about 1% or less in mean FA values for both sexes. The combined group analyses did not show any evidence for a sex difference in the age-related changes in any of the DTI metrics. There was a trend for a main effect of sex only for MD (greater diffusivity in females than in males at mean age), which reached uncorrected p < 0.05, but only in the model with the mask volume (p = 0.036; Table 4 and Supplemental Table 2). Of note, AD also showed the similar trend for the main effect of sex in the model with the mask volume, which was not selected based on BIC (Supplemental Table 2).

Table 5 and Figure 8 summarize the results of similar analyses conducted on mean NODDI metrics over the same subject-specific cerebral WM mask used to compute mean DTI metrics. Similarly to the DTI metrics, the effects of mask volume on the overall model fit as well as on observed age and sex effects were tested. The mask volume did not impact the estimates of age effects on NODDI metrics, but did show a small but highly significant relationship with IsoVF, with larger mask volume associated with higher IsoVF (0.03 to 0.04% increase per cc mask volume with *p*'s < 2×10^{-8} in both sexes, explaining 6.6 and 3.3% of total variance for males and females, respectively). It modified the magnitude of sex effect on mean IsoVF, but did not significantly impact that of mean NDI or ODI values (Table 5 and Supplemental Table 3). Below we present the results of models without mask volume for NDI and ODI, and the model with mask volume for IsoVF, but the alternative model results can be found in the Supplemental Table 3.

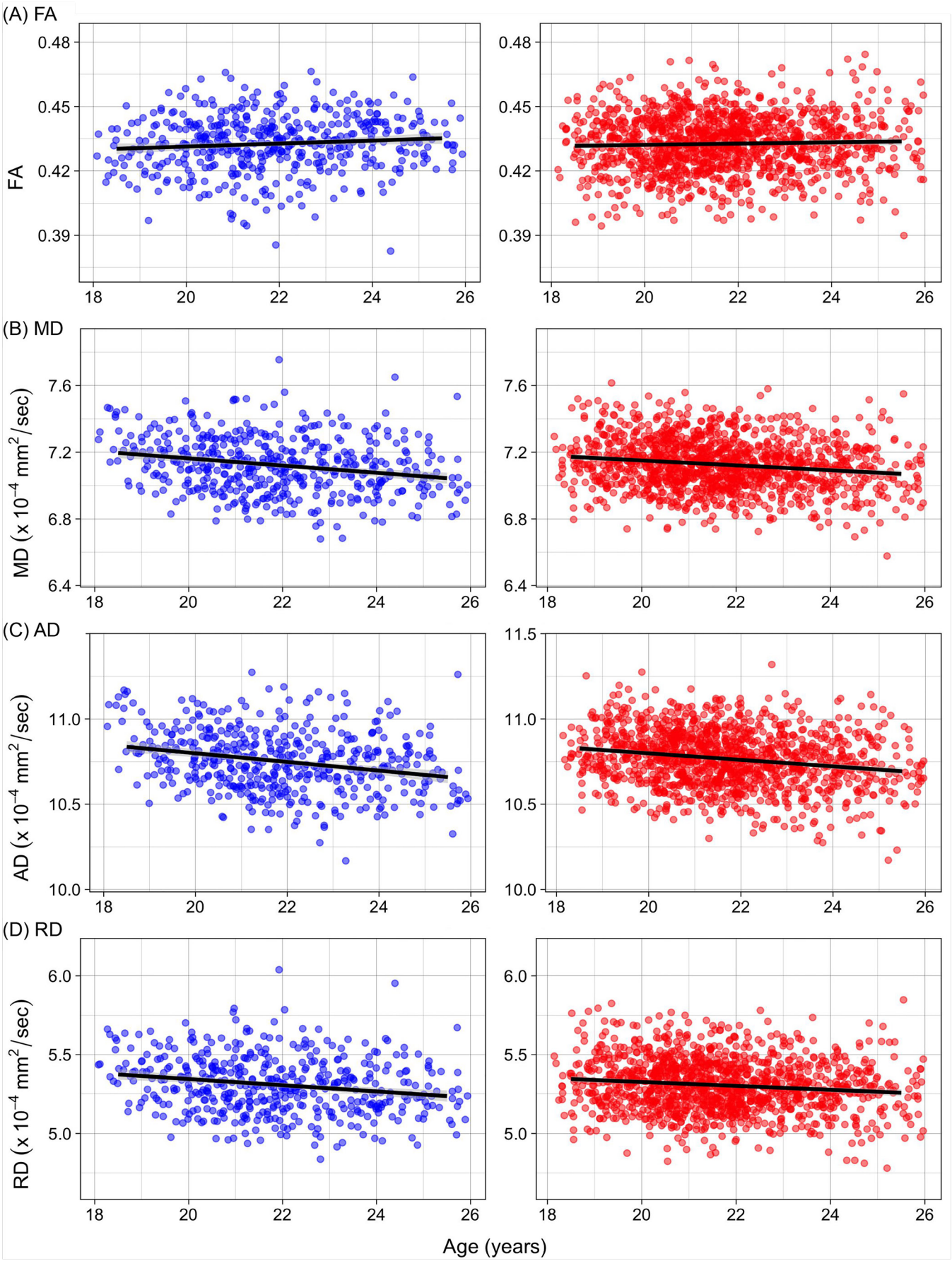

Figure 7. Age-related variations in mean DTI values within the cerebral WM mask. The mean values of (A) FA, (B) MD, (C) AD, and (D) RD within subject-specific cerebral WM mask are plotted against age, with individual subjects represented as scatter points (left panel: male, middle panel: female). For each sex, predicted age trajectories, based on the model selected by BIC (see text) in the sex-specific analyses are shown. The plots in the right panel show predicted trajectories for hypothetical male or female subjects with identical, global mean cerebral WM volume, based on combined group analyses. The 95% confidence intervals of the predictions are represented as shades around the line.

Table 5. Summary of mean NODDI metrics within cerebral white matter. *Descriptive statistics and the results of linear model fit for mean NODDI metrics within subject-specific cerebral WM masks are shown. Parameter estimates (β) for age and sex are shown, together with 95% confidence intervals (CI) for each β, as well as uncorrected p values and partial eta squared as the effect sizes for each variable. The Model column indicates the selected model (see text) with the corresponding model number as described in Methods section. The interaction between sex and age was tested in the combined group but was not significant in any of the metrics listed here, and thus is not included in the table. The variance explained by mask volume for models that included it is discussed in the text. Overall model fit is indicated as adjusted squared R values.*

				Age			Sex (M>F)			
	N	Mean±SD [min, max]	Model	β [95% CI]	*p*	partial η^2	β [95% CI]	*p*	partial η^2	adj-R^2
NDI				($x10^{-3}$ /year)			($x10^{-3}$)			
Males	468	0.636 ± 0.027 [0.548, 0.714]	(1)	3.66 [2.38, 4.95]	$3.7x10^{-8}$	0.063	--	--	--	0.061
Females	1246	0.625 ± 0.024 [0.560, 0.709]	(1)	2.53 [1.77, 3.30]	$1.1x10^{-11}$	0.033	--	--	--	0.032
Combined	1714	0.628 ± 0.025 [0.548, 0.714]	(3)	3.10 [2.38, 3.82]	$<2.0x10^{-16}$	0.041	11.3 [8.73, 13.9]	$<2.0x10^{-16}$	0.042	0.083
ODI				($x10^{-4}$/year)			($x10^{-4}$)			
Males	468	0.280 ± 0.008 [0.260-0.301]	(1)	6.66 [2.58, 10.7]	0.0014	0.022	--	--	--	0.020
Females	1246	0.277 ± 0.009 [0.253-0.308]	(1)	6.42 [3.62, 9.21]	$7.2x10^{-6}$	0.016	--	--	--	0.015
Combined	1714	0.278 ± 0.009 [0.253-0.308]	(3)	6.54 [4.01, 9.07]	$4.5x10^{-7}$	0.017	19.4 [10.2, 28.5]	$3.3x10^{-5}$	0.010	0.028
IsoVF				($x10^{-4}$/year)			($x10^{-4}$)			
Males	468	0.135 ± 0.010 [0.105, 0.170]	(2)	2.84 [-1.92, 7.61]	0.24	0.003	--	--	--	0.066
Females	1246	0.130 ± 0.009 [0.101, 0.162]	(2)	3.29 [0.34, 6.23]	0.029	0.004	--	--	--	0.035
Combined	1714	0.131 ± 0.010 [0.101, 0.170]	(4)	3.07 [0.32, 5.81]	0.028	0.004	24.5 [11.6, 37.3]	$2.7x10^{-4}$	0.012	0.106

Both NDI and ODI showed a small but robust increase with age at this age range in both the male and female groups with APC of about 0.6% and 0.2% for NDI and ODI in males, and 0.4% and 0.2%, in females. The age effect on IsoVF only reached the uncorrected $p < 0.05$ in females ($p = 0.029$) but not in males ($p = 0.24$), in the positive direction (APC of about 0.25%). The combined group analyses indicated robust main effects of sex for all the NODDI metrics, with males showing higher values for all three metrics, representing 1.8, 0.7, and 1.9% larger values in males relative to femalesfor NDI, ODI, and IsoVF, respectively. However, none of the NODDI metrics showed evidence for the sex difference in the age-related changes. Partial η^2 indicated that the amount of variance explained by age for NODDI metrics in the combined group to be about 4, 2, and 0.4% for NDI, ODI, and IsoVF, respectively, while main effect of sex accounted for about 4, 1, and 1% of the variance.

Resting-state fMRI

Figure 9A shows the average regional IC matrix computed on the 384 regions of the AICHA homotopic functional atlas. As the definition of the region is based on the functional signal, some regions (such as the rolandic region) cross the anatomical borders because they exhibit very high correlations. The regional IC matrices computed with and without global signal regression are shown side by side. Figure 9B, C, and D show the group average maps of ReHo, ALFF, and fALFF, respectively.

Summary of the results

In a sample of students aged between 18 and 26 years, several significant age-associated variations were observed. Cortical GM thickness, surface area, and total GM volume were decreasing with age, whereas WM total volume showed increase. Diffusivity, either radial or axial (and therefore mean) was found to robustly decrease with age but fractional anisotropy showed only a tendency for a slight increase. Both NDI and ODI robustly increased with age during this period, accompanied with a trend for increasing IsoVF as well. There were no sex differences in age-related trajectory in any of the global metrics we reported here. For GM morphometry, we observed thicker CT in males than in females, while inner CSA and GM volume were larger in females than in males when eTIV was taken into account. The WM DTI metrics did not differ between the two sexes. By contrast, all three NODDI metrics showed a strong sex effects, with higher values in males than in females.

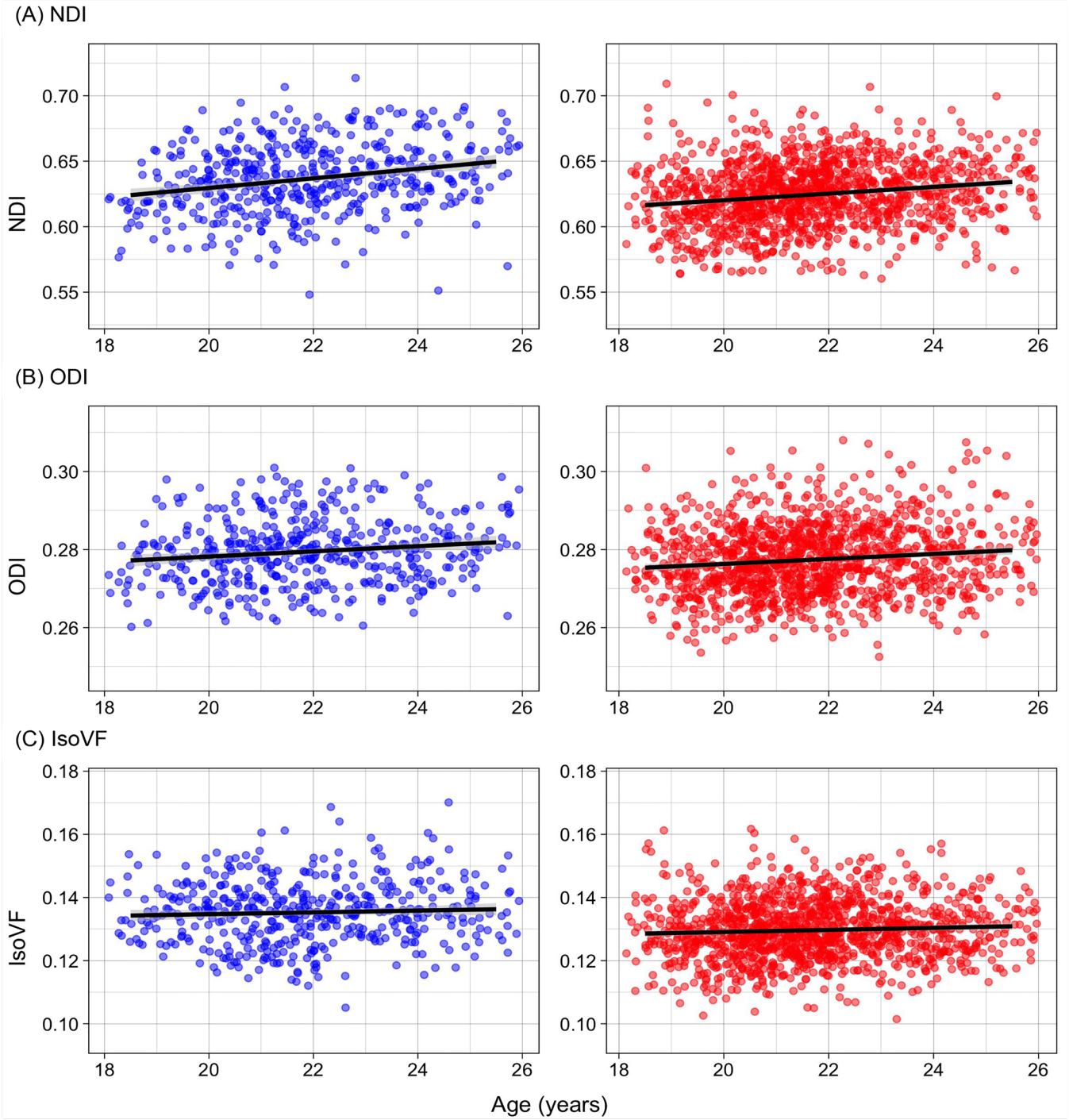

Figure 8. Age-related variations in mean NODDI values within the cerebral WM mask. The mean values of (A) NDI, (B) ODI, and (C) IsoVF within subject-specific cerebral WM mask are plotted against age, with individual subjects represented as scatter points (left panel: male, middle panel: female). For each sex, predicted age trajectories, based on the model selected by BIC (see text) in the sex-specific analyses are shown. The plots in the right panel show predicted trajectories for hypothetical male or female subjects with identical, global mean cerebral WM volume, based on combined group analyses. The 95% confidence intervals of the predictions are represented as shades around the line.

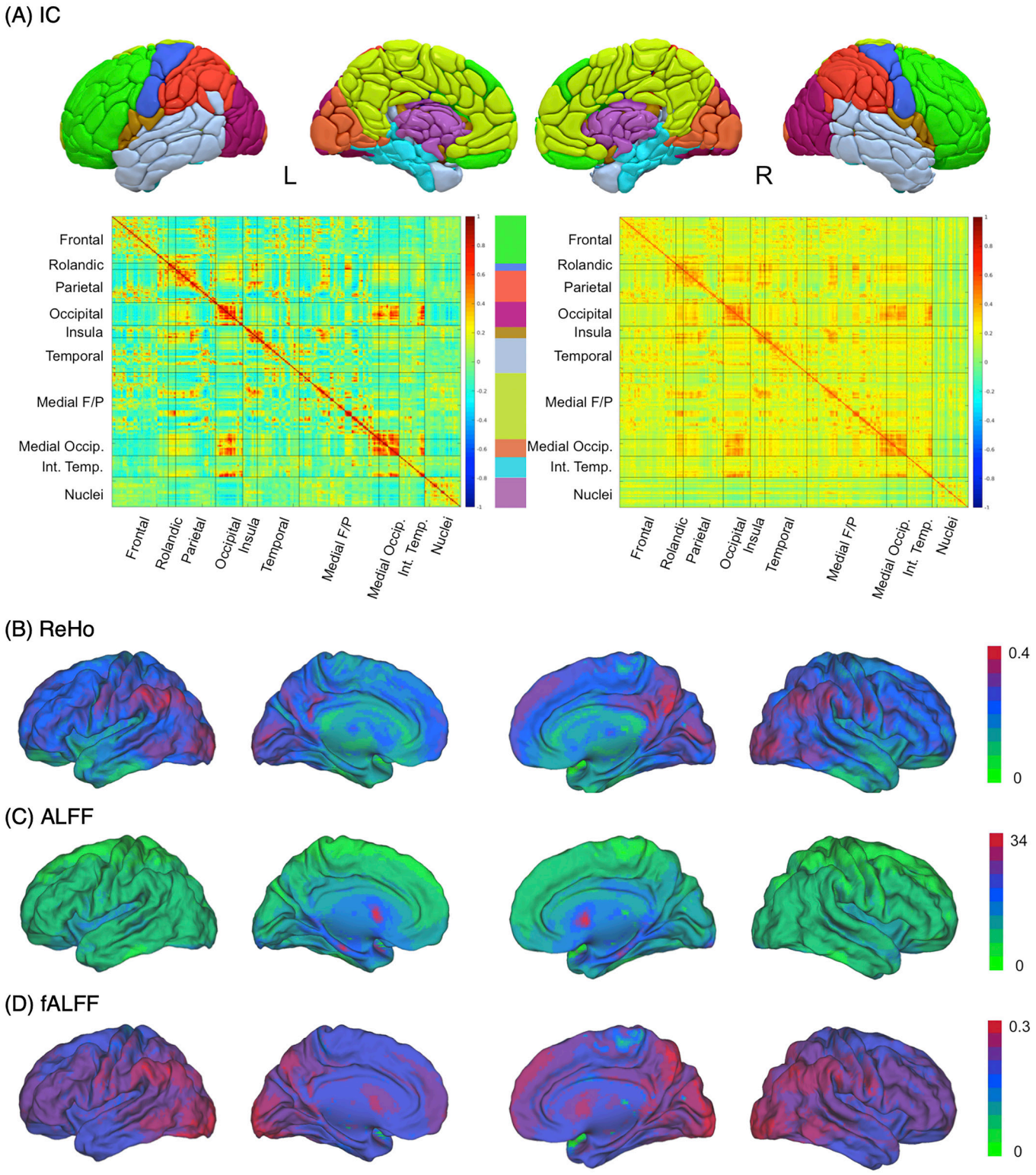

Figure 9. Group average IC matrices and three rs-fMRI-based metrics in 1,814 MRi-Share subjects. (A) AICHA atlas-based regional IC matrices computed from rs-fMRI signals with (left) and without (right) global signal regression. The top panel shows the 10 anatomical partitions of 384 AICHA regions, with the color corresponding to the color block between the two IC matrices (Medial F/P: medial fronto-parietal; Medial Occip.: medial occipital; Int.Temp.: internal temporal), displayed with Surf Ice (https://www.nitrc.org/projects/surfice). Voxel-level group average maps of (B) ReHo, (C) ALFF, and (D) fALFF in the spatially normalized space are superimposed on fiducial surface of PALS template using Caret 5.65 (http:brainvis.wustle.edu).

Discussion

We will first address the impact that some specific features of the MRi-Share study design may have on the interpretation of these findings. We then discuss our results with respect to the existing literature on the maturational/ageing changes as well as sex differences in global brain phenotypes. Lastly, we will describe the future directions and perspectives on the MRi-Share database specifically, and on the even richer resources available when combining this database with the Bio-Share and i-Share study data.

Specific features of the MRi-Share study design

The MRi-Share sample of about 2,000 students, which has been drawn from the i-Share participants from Bordeaux University, is not a representative sample of the population of healthy young adults and was actually never intended to be so. It must indeed be reminded that the primary objective of the i-Share cohort study is to investigate the student population health. As a consequence, our study sample concerns only 25% of the population of the same age range, and its structure differs from the 75% others particularly in terms of socio-demographics, lifestyle, and level of education. Some of these sampling biases can be accounted for through stratification as we did for example for sex. Some others, such as level of education or lifestyle for example, will require access to additional sources of data to be accounted for.

Another source of concern is the non-uniformity of the sample age distribution as the number of students reduces with the number of years attended at the University. This led us to analyse only a subsample of the participants with a shorter age range (18 to 26 years), thereby avoiding claiming findings to be valid for those 110 participants aged between 26 to 35 years. Additional data are clearly needed to study how the brain changes during this later period of early adulthood. Several potential confounding factors in interpreting our preliminary were not accounted for, including past or current history of mental illness, alcohol intake, smoking habits, and/or use of any recreational drugs and psychotropic medications, … Effects of these factors on structural/functional brain phenotypes in the MRi-Share cohort papers will be reported in other forthcoming publications.

The MRi-Share study design is also cross-sectional in nature, which makes one take the results of the present study with caution. Numerous reports have indeed pointed out the caveats of cross-sectional design for assessing effects of age and demonstrated how such design may lead to spurious findings when compared to those obtained with longitudinal data (Fjell et al., 2010; Pfefferbaum and Sullivan, 2015). In the present work, we tried to minimize these pitfalls by reducing the age range to 8 years only and by selecting a simple linear model to examine age-related changes. We note that several results of the present study are indeed compatible with those of previously published longitudinal studies (see discussion below) in adolescents and adults. However, such precautions do not fully eradicate some intrinsic limits of our cross-sectional study, and particularly the impossibility of identifying the dynamics of age trajectories for the different brain phenotypes as has been done in other studies (Raznahan et al. 2011). Such limitations could be alleviated by having MRi-Share participants undergo a follow-up MRI examination.

Age-related patterns of cortical thickness, surface area, and GM volume

We observed varying degrees of age-related variations in all GM morphometric measures we examined in the students aged between 18 and 26 years old. All metrics showed apparent reduction with age, suggesting that CT and both inner and pial CSA are shrinking, resulting in the reduction of total GM volume, even at the narrow age-range of late adolescence and young adulthood represented by the MRi-Share cohort. We did not find any sex differences in the expected age-related trajectory of these metrics. The observed age-related trajectories are in line with the large body of work documenting the age-related variations and changes in brain structural morphometry over the lifespan, which has revealed that while both GM and WM volumes increase rapidly during infancy, GM volume starts to decrease during childhood, when WM volume continues to grow well into adulthood, before declining at middle-to late-adulthood (reviewed in Fjell and Walhovd, 2010; Lebel and Deoni, 2018; Vijayakumar et al., 2018). The GM volume reduction is accompanied by the reduction in both CT and CSA post-childhood, although the age-related trajectories of CT and CSA are largely independent (Potvin et al., 2017; Wierenga et al., 2014), and regionally the reduction in CT and CSA may even have negative relationships (Hogstrom et al., 2013; Storsve et al., 2014).

The estimates of APC observed in our cross-sectional data (CT: -0.12%, inner CSA: -0.16%, GM: -0.32%, based on the combined-sex analyses) were less than those observed in longitudinal cohorts during development (CT: -0.8 to -1.4%, inner CSA: -0.4 to -0.7%, cortical GM: -1.1 to -1.9% between 7 to 29 years of age, Tamnes et al., 2017), and very close to those observed during adult life (CT: -0.16, -0.35%, inner CSA: -0.22, -0.19%, cortical GM: -0.41, -0.51% reported in cohorts between 18 to 87 years of age in Lemaitre et al. 2012, and between 23 to 87 years of age in Storsve et al. 2014, respectively). The slightly lower estimate for GM volume APC in our data may be partially explained by the fact that we report total GM volume, rather than cortical GM volume only, which has been shown to decrease more with age

compared to subcortical GM volumes (Walhovd et al., 2011, 2005). Alternatively, the lower GM volume, as well as the slightly lower CT and CSA APC may reflect the slowed volume change at the end of maturation and before the onset or the early phase of the ageing-related reduction in volume. We also demonstrated that pial CSA is more sensitive to age-related changes (estimated APC in the combined group at -0.27%) than both the inner CSA computed based on GM/WM boundary and the CT. This was despite the tight correlation between the inner and pial CSA. It may be explained by the notion that the pial surface is likely to be affected by age-related variations in CT more than in the white surface (Winkler et al., 2012), resulting in the slightly greater age-related reduction than either inner CSA or CT.

Age-related patterns of global WM volume and DTI/NODDI metrics

In contrast with age effects on GM morphometric measures, the eTIV-adjusted WM volume was found to be increasing between the ages of 18 and 26 years, at the rate of 0.23% annually, whereas the raw WM volume was only slightly but not significantly affected by age positively (APC = 0.08%, Supplementary Table 2). These findings are consistent with the literature that indicates the inverted U-shape age trajectory of WM volume, which increases largely linearly up to the fourth or fifth decade of life, before declining in later life (Hasan et al., 2007; Lebel et al., 2012; Walhovd et al., 2011; Westlye et al., 2010). The estimates of APC depend on the precise age range examined as well as the reference age, which are not always reported in the literature, as well as on whether or not adjustment for intracranial volume was performed. For instance, Walhovd et al. (2011) reported percent change per decade for cerebral WM to be 3.9%, calculated based on mean raw WM volumes of those aged 18 to 29 years and those aged 30 to 39 years, which would mean roughly 0.4% APC, assuming a linear and constant increase during the decade. Although the percent change per decade in this study was based on raw WM volume not corrected for intracranial volume (ICV), another study investigating multiple younger cohorts reported APC (estimated at each age) of 0 to 1% for the age range of 20 to 30 years when correcting for ICV either by dividing the WM by the ICV or by including ICV as a covariate in the model, similar to what we did here (Figure S4 in Mills et al., 2016), more in line with our estimated APC.

The observed age-related variations of WM microstructure IDPs are in consistent with the past studies that revealed the U-shaped trajectories for WM water diffusivity measures (MD, AD, and RD), which all keep decreasing throughout development and reach their minimum values between second and fourth decade of life, before increasing with age, and FA showing the opposite pattern of trajectory that increases during development and decreases in ageing (Beaudet et al., 2020; Hasan et al., 2010, 2007; Lebel et al., 2012; Slater et al., 2019; Westlye et al., 2010). More limited number of studies using NODDI showed the continuous increase of NDI through development (Genc et al., 2017; Mah et al., 2017) and adulthood (Chang et al., 2015; but see Kodiweera et al., 2016), peaking around the fourth and fifth decade of life (Slater et al., 2019) before declining at a later age (Cox et al., 2016; Merluzzi et al., 2016). ODI, on the other hand, has not been reported to change noticeably during development but starts to increase during young adulthood (Chang et al., 2015; Genc et al., 2017; Mah et al., 2017), peaking between the fourth and sixth decade of life and declining thereafter (Cox et al., 2016; Slater et al., 2019).

Although both DTI and NODDI metrics are often described in terms of biological properties, in reality they are based on mathematical models that are fit to explain DWI data that are collected at the resolution many times coarser than the structures these models aim to probe (axonal fibers, intracellular and extracellular compartments). Thus, it is not always straightforward to interpret apparent changes or differences in these metrics, in particular for DTI metrics, which could be affected by many different microstructural features (number, size, and orientations of axonal fibers, membrane permeability, myelination etc) (Jones et al., 2013). Nonetheless, it could be speculated that the apparent age-related elevation in NDI and ODI is consistent with the interpretation that continuing growth of neurites that steadily increase intracellular (axonal) diffusion in the cerebral WM is coupled with increased overall fiber complexity at this age range (ref needed). Such increase in overall fiber complexity, coupled with reduced extra-axon diffusion as a result of denser packing of axons (Suzuki et al., 2003), can account for the overall reduction in the rate of diffusion in the simple tensor model estimated at the voxel-level.

Sex effects on GM and WM global phenotypes

Beyond the well-known difference in the overall head and brain size, the findings with regard to sex differences in global and regional GM morphometry and in age-related trajectory on of these morphometric measures are often mixed (Fjell et al., 2015; e.g. Gennatas et al., 2017; Hasan et al., 2007; Herron et al., 2015; Jahanshad and Thompson, 2017; Kaczkurkin et al., 2019; Lemaître et al., 2005; McKay et al., 2014; Mutlu et al., 2013; Raznahan et al., 2010; Ritchie et al., 2018; Sowell et al., 2007), and are known to depend on if and how the effect of head or brain size is taken into account (Herron et al., 2015; Mills et al., 2016). Generally, CSA and GM volumes, but not CT, are strongly correlated with the overall brain size (Potvin et al., 2017), and

unsurprisingly, males show larger absolute values in these metrics compared to females, as was the case in our data. When corrected for eTIV, we saw a slight but significantly greater GM volume in females than in males and a similar trend for CSA in our data, although the difference was very small relative to the total variance of data (sex effects accounting for less than 1% of variance for both, based on partial η^2 values). For CT, prior large-scale studies (sample size > 500) have reported either no sex difference in global mean CT during development and over lifespan (Ducharme et al., 2016; Fjell et al., 2015; Gennatas et al., 2017), or globally greater CT in females than in males in mid- to late-adulthood (Ritchie et al., 2018), though there are also some reports of greater mean CT in males than in females throughout development (Raznahan et al., 2011) and over lifespan (Kochunov et al., 2011). We found significantly thicker mean CT in males than in females in our data, which was not affected by eTIV correction, that accounted for nearly 2% of variance in the CT data. Since sex differences in CT are also reported to be regionally heterogeneous and age-dependent (Mutlu et al., 2013; Raznahan et al., 2010; Sotiras et al., 2017; Sowell et al., 2007), future investigations will examine the regional patterns in the CT difference and clarify whether what we observe is consistent with what would be expected at this age range or somehow unique to our sample due to some specific aspects of demographic characteristics (e.g. higher education) in our data.

We did not find any sex differences in eTIV-adjusted WM volume or its age-related variations, consistent with prior studies reporting similar normalized WM volumes and age-related trajectory during much of the adulthood (Coupé et al., 2017; Fjell et al., 2009; Lebel et al., 2012), although there are a few high-powered studies reporting larger WM volume in males than in females even after correcting for the total brain volume, albeit with much reduced effect sizes (Ritchie et al., 2018; Wierenga et al., 2014).

As for the sex differences in the age trajectories of DTI metrics, most studies report no or minimal differences (Hasan et al., 2010; Hsu et al., 2010, 2008; Lebel et al., 2012; Pohl et al., 2016; Wang et al., 2012), except earlier in development (Simmonds et al., 2014). In our recent multi-cohort study that investigated mean DTI metrics across the WM skeleton in a large sample (total N >20,000) that included the MRi-Share and 9 other cohorts that collectively spanned the entire adult lifespan, we also failed to detect any sex effects on the age-associated trajectory of the DTI metrics at this or any other age ranges examined during adulthood (Beaudet et al., 2020). In the same study, we also found significantly greater AD and MD in females than males when controlling for eTIV, which affected the mean AD, MD, and FA values significantly. While it has been reported that volume over which mean DTI metrics are computed can affect mean values due to PVEs (Vos et al., 2011), the effects of tract or mask volumes, or the overall head and brain size when DTI metrics are compared in spatially normalized space, are not often investigated. Further studies are needed to clarify how it would impact the apparent sex differences or lack of them when comparing DTI metrics.

Very little is known about the sex differences in NODDI metrics. The few studies that report sex effects seem to indicate little or no sex differences in the age trajectory (Cox et al., 2016; Slater et al., 2019), but are inconsistent with regard to the main effects of sex on NODDI metrics: one developmental (Mah et al., 2017) and another lifespan (Slater et al., 2019) study reported no main effects of sex, while one study in young to middle-aged adults reported greater NDI for males compared to females in most WM tracts examined as well as greater ODI in some tracts (Kodiweera et al., 2016), and yet another study with high power (N >3,500) reported consistently higher ODI in females compared to males across all the WM tracts examined in older adults (Cox et al., 2016). While the direction of the sex differences we observed is similar to those reported by Kodiweera et al. (2016), the magnitude of the difference was much smaller in our study (2.1 and 0.7% for NDI and ODI in our data, compared to about 7% for both NDI and ODI reported by Kodiweera et al. (2016)). Further studies are needed to investigate whether the sex differences in these microstructural measures manifest themselves in specific time window of early adulthood, or whether they may be modulated by other demographic variables.

Future directions and perspectives

The MRi-Share database represents a unique, multi-modal neuroimaging and cognitive and genetic dataset of a large, cross-sectional cohort of young adults undergoing university-level education. Its design and the sample size will allow detailed characterization of age-related changes in brain structure and function in the post-adolescence period, as well as the investigation of lifestyle and sociodemographic factors that may modulate these changes.

In addition, the MRi-Share database enriches the relatively scarce corpus of data available in young adults, thereby allowing investigations of structural and functional brain changes across the complete adult lifespan. A proof of concept of such added-value of the MRi-Share sample was recently provided through a multi-cohort study across the adult life span of age-related changes of PSMD (Peak width Skeletonized Mean Diffusivity), a novel imaging marker of small vessel disease (Baykara et al., 2016): in this study, thanks to the MRi-Share sample, PSMD was demonstrated to be the only DTI-derived phenotype that increased in the immediate post-adolescence period, indicating that it could serve as

an early marker of aging (Beaudet et al., 2020). MRi-Share also provides the opportunity to assess whether imaging markers of late-life disorders can be detected earlier in adult life. With this in mind, we will release in the near future a number of additional IDPs, including white matter hyperintensities (WMH) assessed on T2-FLAIR images, enlarged perivascular spaces (ePVS) assessed on T1w images, and cerebral microbleeds (CMB) assessed on SWI images,all being well-established imaging-markers of small vessel disease (Wardlaw et al., 2013).

Acknowledgements

The i-Share cohort has been funded by a grant ANR-10-COHO-05-01 as part of the Programme pour les Investissements d'Avenir). Supplementary funding was received from the Conseil Régional of Nouvelle-Aquitaine, reference 4370420. The MRi-Share cohort and the ABACI software development have been supported by ANR-10-LABX-57 (TRAIL) and ANR-16-LCV2-0006 (GINESISLAB for the software) grants. The bio-Share cohort and some regulatory and ethical aspects of MRi-Share have been supported by the European Research Council (ERC) under the European Union's Horizon 2020 research and innovation programme under grant agreement No 640643 and the FHU SMART. Acquisition of a MRI scanner dedicated to MRi-Share was made possible thanks to a grant from the Conseil Régional d'Aquitaine. Ami Tsuchida, Naka Beguedou, and Alexandre Laurent have been supported by a grant from the Fondation pour la Recherche Médicale (DIC202161236446), Marie-Fateye Gueye, Violaine Verrecchia, and Victor Nozais by a grant ANR-16-LCV2-0006 (GINESISLAB), and Antonietta Pepe by a grant ANR-15-HBPR-0001-03 (as part of the EU FLAG-ERA MULTI-LATERAL consortium). The authors express their deep gratitude to Loïc Labache for his help in preparing the manuscript. They are also indebted to the following individuals for their invaluable contribution to the MRi-Share project: Serge Anandra, Amandine André, Gregory Beaudet, Christophe Bernard, Bruno Brochet, Aurore Capelli, Claire Cardona, Arnaud Chaussé, Christophe Delalande, Vincent Durand, Louise Knafo, Morgane Lachaize, Hugues Loiseau, Elena Milesi, Marie Mougin, Maylis Melin, Guy Perchey, Clothilde Pollet, Thomas Tourdias, Cécile Marchal, Guillaume Penchet, Cécile Dulau, Igor Sibon, Sabrina Debruxelle, Sophie Auriacombe, Caroline Roussillon, Nicolas Vinuesa, and the i-Share "relay" students. The authors are also indebted to Paul Matthews (Imperial College, London, UK) and to the personnel of the UK Biobank imaging center at Stockport (UK) for their help while designing the Mri-Share image acquisition protocol, and to Maxime Descoteaux (Sherbrook University, Canada) for his help in impementing the DWI processing and QC pipelines.Finally, the authors would like to express their gratitude to the 1,870 students of the Bordeaux University who gave their consent to participate in MRi-Share.

Data Availability

i-Share is open to collaborations and partnerships and supports local, national, and international collaborations from the public or private sector. Requests to access the database should be sent at contact@i-share.fr.

References

3C Study Group, 2003. Vascular factors and risk of dementia: design of the Three-City Study and baseline characteristics of the study population. Neuroepidemiology 22, 316–325. doi:10.1159/000072920

Alfaro-Almagro, F., Jenkinson, M., Bangerter, N.K., Andersson, J.L.R., Griffanti, L., Douaud, G., Sotiropoulos, S.N., Jbabdi, S., Hernandez-Fernandez, M., Vallee, E., Vidaurre, D., Webster, M., McCarthy, P., Rorden, C., Daducci, A., Alexander, D.C., Zhang, H., Dragonu, I., Matthews, P.M., Miller, K.L., Smith, S.M., 2018. Image processing and Quality Control for the first 10,000 brain imaging datasets from UK Biobank. Neuroimage 166, 400–424. doi:10.1016/j.neuroimage.2017.10.034

Backhausen, L.L., Herting, M.M., Buse, J., Roessner, V., Smolka, M.N., Vetter, N.C., 2016. Quality Control of Structural MRI Images Applied Using FreeSurfer-A Hands-On Workflow to Rate Motion Artifacts. Front. Neurosci. 10, 558. doi:10.3389/fnins.2016.00558

Backhouse, E.V., McHutchison, C.A., Cvoro, V., Shenkin, S.D., Wardlaw, J.M., 2017. Early life risk factors for cerebrovascular disease: A systematic review and meta-analysis. Neurology 88, 976–984. doi:10.1212/WNL.0000000000003687

Basser, P.J., Mattiello, J., LeBihan, D., 1994. MR diffusion tensor spectroscopy and imaging. Biophys. J. 66, 259–267. doi:10.1016/S0006-3495(94)80775-1

Baykara, E., Gesierich, B., Adam, R., Tuladhar, A.M., Biesbroek, J.M., Koek, H.L., Ropele, S., Jouvent, E., Alzheimer's Disease Neuroimaging Initiative, Chabriat, H., Ertl-Wagner, B., Ewers, M., Schmidt, R., de Leeuw, F.-E., Biessels, G.J., Dichgans, M., Duering, M., 2016. A novel imaging marker for small

vessel disease based on skeletonization of white matter tracts and diffusion histograms. Ann. Neurol. 80, 581–592. doi:10.1002/ana.24758

Beaudet, G., Tsuchida, A., Petit, L., Tzourio, C., Caspers, S., Schreiber, J., Pausova, Z., Patel, Y., Paus, T., Schmidt, R., Pirpamer, L., Sachdev, P.S., Brodaty, H., Kochan, N., Trollor, J., Wen, W., Armstrong, N.J., Deary, I.J., Bastin, M.E., Wardlaw, J.M., Mazoyer, B., 2020. Age-Related Changes of Peak Width Skeletonized Mean Diffusivity (PSMD) Across the Adult Lifespan: A Multi-Cohort Study. Front. Psychiatry 11, 342. doi:10.3389/fpsyt.2020.00342

Caspers, S., Moebus, S., Lux, S., Pundt, N., Schütz, H., Mühleisen, T.W., Gras, V., Eickhoff, S.B., Romanzetti, S., Stöcker, T., Stirnberg, R., Kirlangic, M.E., Minnerop, M., Pieperhoff, P., Mödder, U., Das, S., Evans, A.C., Jöckel, K.-H., Erbel, R., Cichon, S., Amunts, K., 2014. Studying variability in human brain aging in a population-based German cohort-rationale and design of 1000BRAINS. Front. Aging Neurosci. 6, 149. doi:10.3389/fnagi.2014.00149

Chang, Y.S., Owen, J.P., Pojman, N.J., Thieu, T., Bukshpun, P., Wakahiro, M.L.J., Berman, J.I., Roberts, T.P.L., Nagarajan, S.S., Sherr, E.H., Mukherjee, P., 2015. White Matter Changes of Neurite Density and Fiber Orientation Dispersion during Human Brain Maturation. PLoS ONE 10, e0123656. doi:10.1371/journal.pone.0123656

Corley, J., Cox, S.R., Deary, I.J., 2018. Healthy cognitive ageing in the Lothian Birth Cohort studies: marginal gains not magic bullet. Psychol. Med. 48, 187–207. doi:10.1017/S0033291717001489

Coupé, P., Catheline, G., Lanuza, E., Manjón, J.V., Alzheimer's Disease Neuroimaging Initiative, 2017. Towards a unified analysis of brain maturation and aging across the entire lifespan: A MRI analysis. Hum. Brain Mapp. 38, 5501–5518. doi:10.1002/hbm.23743

Cox, R.W., 1996. AFNI: software for analysis and visualization of functional magnetic resonance neuroimages. Comput. Biomed. Res. 29, 162–173. doi:10.1006/cbmr.1996.0014

Cox, S.R., Ritchie, S.J., Tucker-Drob, E.M., Liewald, D.C., Hagenaars, S.P., Davies, G., Wardlaw, J.M., Gale, C.R., Bastin, M.E., Deary, I.J., 2016. Ageing and brain white matter structure in 3,513 UK Biobank participants. Nat. Commun. 7, 13629. doi:10.1038/ncomms13629

Daducci, A., Canales-Rodríguez, E.J., Zhang, H., Dyrby, T.B., Alexander, D.C., Thiran, J.-P., 2015. Accelerated Microstructure Imaging via Convex Optimization (AMICO) from diffusion MRI data. Neuroimage 105, 32–44. doi:10.1016/j.neuroimage.2014.10.026

Deary, I.J., Gow, A.J., Taylor, M.D., Corley, J., Brett, C., Wilson, V., Campbell, H., Whalley, L.J., Visscher, P.M., Porteous, D.J., Starr, J.M., 2007. The Lothian Birth Cohort 1936: a study to examine influences on cognitive ageing from age 11 to age 70 and beyond. BMC Geriatr. 7, 28. doi:10.1186/1471-2318-7-28

Debette, S., Seshadri, S., Beiser, A., Au, R., Himali, J.J., Palumbo, C., Wolf, P.A., DeCarli, C., 2011. Midlife vascular risk factor exposure accelerates structural brain aging and cognitive decline. Neurology 77, 461–468. doi:10.1212/WNL.0b013e318227b227

Desikan, R.S., Ségonne, F., Fischl, B., Quinn, B.T., Dickerson, B.C., Blacker, D., Buckner, R.L., Dale, A.M., Maguire, R.P., Hyman, B.T., Albert, M.S., Killiany, R.J., 2006. An automated labeling system for subdividing the human cerebral cortex on MRI scans into gyral based regions of interest. Neuroimage 31, 968–980. doi:10.1016/j.neuroimage.2006.01.021

Destrieux, C., Fischl, B., Dale, A., Halgren, E., 2010. Automatic parcellation of human cortical gyri and sulci using standard anatomical nomenclature. Neuroimage 53, 1–15. doi:10.1016/j.neuroimage.2010.06.010

Diedrichsen, J., Balsters, J.H., Flavell, J., Cussans, E., Ramnani, N., 2009. A probabilistic MR atlas of the human cerebellum. Neuroimage 46, 39–46. doi:10.1016/j.neuroimage.2009.01.045

Ducharme, S., Albaugh, M.D., Nguyen, T.-V., Hudziak, J.J., Mateos-Pérez, J.M., Labbe, A., Evans, A.C., Karama, S., Brain Development Cooperative Group, 2016. Trajectories of cortical thickness maturation in normal brain development--The importance of quality control procedures. Neuroimage 125, 267–279. doi:10.1016/j.neuroimage.2015.10.010

Dumontheil, I., 2016. Adolescent brain development. Curr. Opin. Behav. Sci. 10, 39–44. doi:10.1016/j.cobeha.2016.04.012

Field, T.S., Doubal, F.N., Johnson, W., Backhouse, E., McHutchison, C., Cox, S., Corley, J., Pattie, A., Gow, A.J., Shenkin, S., Cvoro, V., Morris, Z., Staals, J., Bastin, M., Deary, I.J., Wardlaw, J.M., 2016. Early life characteristics and late life burden of cerebral small vessel disease in the Lothian Birth Cohort 1936. Aging (Albany NY) 8, 2039–2061. doi:10.18632/aging.101043

Fjell, A.M., Grydeland, H., Krogsrud, S.K., Amlien, I., Rohani, D.A., Ferschmann, L., Storsve, A.B., Tamnes, C.K., Sala-Llonch, R., Due-Tønnessen, P., Bjørnerud, A., Sølsnes, A.E., Håberg, A.K.,

Skranes, J., Bartsch, H., Chen, C.-H., Thompson, W.K., Panizzon, M.S., Kremen, W.S., Dale, A.M., Walhovd, K.B., 2015. Development and aging of cortical thickness correspond to genetic organization patterns. Proc Natl Acad Sci USA 112, 15462–15467. doi:10.1073/pnas.1508831112

Fjell, A.M., Walhovd, K.B., 2010. Structural brain changes in aging: courses, causes and cognitive consequences. Rev. Neurosci. 21, 187–221. doi:10.1515/REVNEURO.2010.21.3.187

Fjell, A.M., Walhovd, K.B., Westlye, L.T., Østby, Y., Tamnes, C.K., Jernigan, T.L., Gamst, A., Dale, A.M., 2010. When does brain aging accelerate? Dangers of quadratic fits in cross-sectional studies. Neuroimage 50, 1376–1383. doi:10.1016/j.neuroimage.2010.01.061

Fjell, A.M., Westlye, L.T., Amlien, I., Espeseth, T., Reinvang, I., Raz, N., Agartz, I., Salat, D.H., Greve, D.N., Fischl, B., Dale, A.M., Walhovd, K.B., 2009. Minute effects of sex on the aging brain: a multisample magnetic resonance imaging study of healthy aging and Alzheimer's disease. J. Neurosci. 29, 8774–8783. doi:10.1523/JNEUROSCI.0115-09.2009

Fox, J., Friendly, M., Monette, G., 2018. heplots: Visualizing Tests in Multivariate Linear Models. R package version 1.3-5.

Frazier, J.A., Chiu, S., Breeze, J.L., Makris, N., Lange, N., Kennedy, D.N., Herbert, M.R., Bent, E.K., Koneru, V.K., Dieterich, M.E., Hodge, S.M., Rauch, S.L., Grant, P.E., Cohen, B.M., Seidman, L.J., Caviness, V.S., Biederman, J., 2005. Structural brain magnetic resonance imaging of limbic and thalamic volumes in pediatric bipolar disorder. Am. J. Psychiatry 162, 1256–1265. doi:10.1176/appi.ajp.162.7.1256

Garyfallidis, E., Brett, M., Amirbekian, B., Rokem, A., van der Walt, S., Descoteaux, M., Nimmo-Smith, I., Dipy Contributors, 2014. Dipy, a library for the analysis of diffusion MRI data. Front. Neuroinformatics 8, 8. doi:10.3389/fninf.2014.00008

Genc, S., Malpas, C.B., Holland, S.K., Beare, R., Silk, T.J., 2017. Neurite density index is sensitive to age related differences in the developing brain. Neuroimage 148, 373–380. doi:10.1016/j.neuroimage.2017.01.023

Gennatas, E.D., Avants, B.B., Wolf, D.H., Satterthwaite, T.D., Ruparel, K., Ciric, R., Hakonarson, H., Gur, R.E., Gur, R.C., 2017. Age-Related Effects and Sex Differences in Gray Matter Density, Volume, Mass, and Cortical Thickness from Childhood to Young Adulthood. J. Neurosci. 37, 5065–5073. doi:10.1523/JNEUROSCI.3550-16.2017

Gluckman, P.D., Hanson, M.A., Cooper, C., Thornburg, K.L., 2008. Effect of in utero and early-life conditions on adult health and disease. N. Engl. J. Med. 359, 61–73. doi:10.1056/NEJMra0708473

Goldstein, J.M., Seidman, L.J., Makris, N., Ahern, T., O'Brien, L.M., Caviness, V.S., Kennedy, D.N., Faraone, S.V., Tsuang, M.T., 2007. Hypothalamic abnormalities in schizophrenia: sex effects and genetic vulnerability. Biol. Psychiatry 61, 935–945. doi:10.1016/j.biopsych.2006.06.027

Gorgolewski, K., Burns, C.D., Madison, C., Clark, D., Halchenko, Y.O., Waskom, M.L., Ghosh, S.S., 2011. Nipype: a flexible, lightweight and extensible neuroimaging data processing framework in python. Front. Neuroinformatics 5, 13. doi:10.3389/fninf.2011.00013

Hasan, K.M., Kamali, A., Abid, H., Kramer, L.A., Fletcher, J.M., Ewing-Cobbs, L., 2010. Quantification of the spatiotemporal microstructural organization of the human brain association, projection and commissural pathways across the lifespan using diffusion tensor tractography. Brain Struct. Funct. 214, 361–373. doi:10.1007/s00429-009-0238-0

Hasan, K.M., Sankar, A., Halphen, C., Kramer, L.A., Brandt, M.E., Juranek, J., Cirino, P.T., Fletcher, J.M., Papanicolaou, A.C., Ewing-Cobbs, L., 2007. Development and organization of the human brain tissue compartments across the lifespan using diffusion tensor imaging. Neuroreport 18, 1735–1739. doi:10.1097/WNR.0b013e3282f0d40c

Herron, T.J., Kang, X., Woods, D.L., 2015. Sex differences in cortical and subcortical human brain anatomy [version 1; peer review: 1 approved, 1 approved with reservations]. F1000Res. 4. doi:10.12688/f1000research.6210.1

Hogstrom, L.J., Westlye, L.T., Walhovd, K.B., Fjell, A.M., 2013. The structure of the cerebral cortex across adult life: age-related patterns of surface area, thickness, and gyrification. Cereb. Cortex 23, 2521–2530. doi:10.1093/cercor/bhs231

Hsu, J.-L., Leemans, A., Bai, C.-H., Lee, C.-H., Tsai, Y.-F., Chiu, H.-C., Chen, W.-H., 2008. Gender differences and age-related white matter changes of the human brain: a diffusion tensor imaging study. Neuroimage 39, 566–577. doi:10.1016/j.neuroimage.2007.09.017

Hsu, J.-L., Van Hecke, W., Bai, C.-H., Lee, C.-H., Tsai, Y.-F., Chiu, H.-C., Jaw, F.-S., Hsu, C.-Y., Leu, J.-G., Chen, W.-H., Leemans, A., 2010. Microstructural white matter changes in normal aging: a diffusion tensor imaging study with higher-order polynomial regression models. Neuroimage 49,

32–43. doi:10.1016/j.neuroimage.2009.08.031

Iglesias, J.E., Augustinack, J.C., Nguyen, K., Player, C.M., Player, A., Wright, M., Roy, N., Frosch, M.P., McKee, A.C., Wald, L.L., Fischl, B., Van Leemput, K., Alzheimer's Disease Neuroimaging Initiative, 2015a. A computational atlas of the hippocampal formation using ex vivo, ultra-high resolution MRI: Application to adaptive segmentation of in vivo MRI. Neuroimage 115, 117–137. doi:10.1016/j.neuroimage.2015.04.042

Iglesias, J.E., Van Leemput, K., Bhatt, P., Casillas, C., Dutt, S., Schuff, N., Truran-Sacrey, D., Boxer, A., Fischl, B., Alzheimer's Disease Neuroimaging Initiative, 2015b. Bayesian segmentation of brainstem structures in MRI. Neuroimage 113, 184–195. doi:10.1016/j.neuroimage.2015.02.065

Ikram, M.A., Brusselle, G.G.O., Murad, S.D., van Duijn, C.M., Franco, O.H., Goedegebure, A., Klaver, C.C.W., Nijsten, T.E.C., Peeters, R.P., Stricker, B.H., Tiemeier, H., Uitterlinden, A.G., Vernooij, M.W., Hofman, A., 2017. The Rotterdam Study: 2018 update on objectives, design and main results. Eur. J. Epidemiol. 32, 807–850. doi:10.1007/s10654-017-0321-4

Jahanshad, N., Thompson, P.M., 2017. Multimodal neuroimaging of male and female brain structure in health and disease across the life span. J. Neurosci. Res. 95, 371–379. doi:10.1002/jnr.23919

Jernigan, T.L., Brown, T.T., Hagler, D.J., Akshoomoff, N., Bartsch, H., Newman, E., Thompson, W.K., Bloss, C.S., Murray, S.S., Schork, N., Kennedy, D.N., Kuperman, J.M., McCabe, C., Chung, Y., Libiger, O., Maddox, M., Casey, B.J., Chang, L., Ernst, T.M., Frazier, J.A., Pediatric Imaging, Neurocognition and Genetics Study, 2016. The pediatric imaging, neurocognition, and genetics (PING) data repository. Neuroimage 124, 1149–1154. doi:10.1016/j.neuroimage.2015.04.057

Joliot, M., Jobard, G., Naveau, M., Delcroix, N., Petit, L., Zago, L., Crivello, F., Mellet, E., Mazoyer, B., Tzourio-Mazoyer, N., 2015. AICHA: An atlas of intrinsic connectivity of homotopic areas. J. Neurosci. Methods 254, 46–59. doi:10.1016/j.jneumeth.2015.07.013

Jones, D.K., Knösche, T.R., Turner, R., 2013. White matter integrity, fiber count, and other fallacies: the do's and don'ts of diffusion MRI. Neuroimage 73, 239–254. doi:10.1016/j.neuroimage.2012.06.081

Kaczkurkin, A.N., Raznahan, A., Satterthwaite, T.D., 2019. Sex differences in the developing brain: insights from multimodal neuroimaging. Neuropsychopharmacology 44, 71–85. doi:10.1038/s41386-018-0111-z

Kivipelto, M., Helkala, E.L., Hänninen, T., Laakso, M.P., Hallikainen, M., Alhainen, K., Soininen, H., Tuomilehto, J., Nissinen, A., 2001. Midlife vascular risk factors and late-life mild cognitive impairment: A population-based study. Neurology 56, 1683–1689. doi:10.1212/wnl.56.12.1683

Klein, A., Tourville, J., 2012. 101 labeled brain images and a consistent human cortical labeling protocol. Front. Neurosci. 6, 171. doi:10.3389/fnins.2012.00171

Kochunov, P., Glahn, D.C., Lancaster, J., Thompson, P.M., Kochunov, V., Rogers, B., Fox, P., Blangero, J., Williamson, D.E., 2011. Fractional anisotropy of cerebral white matter and thickness of cortical gray matter across the lifespan. Neuroimage 58, 41–49. doi:10.1016/j.neuroimage.2011.05.050

Kodiweera, C., Alexander, A.L., Harezlak, J., McAllister, T.W., Wu, Y.-C., 2016. Age effects and sex differences in human brain white matter of young to middle-aged adults: A DTI, NODDI, and q-space study. Neuroimage 128, 180–192. doi:10.1016/j.neuroimage.2015.12.033

Kovacs, G.G., Adle-Biassette, H., Milenkovic, I., Cipriani, S., van Scheppingen, J., Aronica, E., 2014. Linking pathways in the developing and aging brain with neurodegeneration. Neuroscience 269, 152–172. doi:10.1016/j.neuroscience.2014.03.045

Kurtzer, G.M., Sochat, V., Bauer, M.W., 2017. Singularity: Scientific containers for mobility of compute. PLoS ONE 12, e0177459. doi:10.1371/journal.pone.0177459

Lebel, C., Deoni, S., 2018. The development of brain white matter microstructure. Neuroimage 182, 207–218. doi:10.1016/j.neuroimage.2017.12.097

Lebel, C., Gee, M., Camicioli, R., Wieler, M., Martin, W., Beaulieu, C., 2012. Diffusion tensor imaging of white matter tract evolution over the lifespan. Neuroimage 60, 340–352. doi:10.1016/j.neuroimage.2011.11.094

Lemaître, H., Crivello, F., Grassiot, B., Alpérovitch, A., Tzourio, C., Mazoyer, B., 2005. Age- and sex-related effects on the neuroanatomy of healthy elderly. Neuroimage 26, 900–911. doi:10.1016/j.neuroimage.2005.02.042

Loeffler, M., Engel, C., Ahnert, P., Alfermann, D., Arelin, K., Baber, R., Beutner, F., Binder, H., Brähler, E., Burkhardt, R., Ceglarek, U., Enzenbach, C., Fuchs, M., Glaesmer, H., Girlich, F., Hagendorff, A., Häntzsch, M., Hegerl, U., Henger, S., Hensch, T., Thiery, J., 2015. The LIFE-Adult-Study: objectives and design of a

population-based cohort study with 10,000 deeply phenotyped adults in Germany. BMC Public Health 15, 691. doi:10.1186/s12889-015-1983-z

Madan, C.R., 2018. Age differences in head motion and estimates of cortical morphology. PeerJ 6, e5176. doi:10.7717/peerj.5176

Mah, A., Geeraert, B., Lebel, C., 2017. Detailing neuroanatomical development in late childhood and early adolescence using NODDI. PLoS ONE 12, e0182340. doi:10.1371/journal.pone.0182340

Makris, N., Goldstein, J.M., Kennedy, D., Hodge, S.M., Caviness, V.S., Faraone, S.V., Tsuang, M.T., Seidman, L.J., 2006. Decreased volume of left and total anterior insular lobule in schizophrenia. Schizophr. Res. 83, 155–171. doi:10.1016/j.schres.2005.11.020

Marcus, D.S., Fotenos, A.F., Csernansky, J.G., Morris, J.C., Buckner, R.L., 2010. Open access series of imaging studies: longitudinal MRI data in nondemented and demented older adults. J. Cogn. Neurosci. 22, 2677–2684. doi:10.1162/jocn.2009.21407

Mazoyer, B., Mellet, E., Perchey, G., Zago, L., Crivello, F., Jobard, G., Delcroix, N., Vigneau, M., Leroux, G., Petit, L., Joliot, M., Tzourio-Mazoyer, N., 2016. BIL&GIN: A neuroimaging, cognitive, behavioral, and genetic database for the study of human brain lateralization. Neuroimage 124, 1225–1231. doi:10.1016/j.neuroimage.2015.02.071

McKay, D.R., Knowles, E.E.M., Winkler, A.A.M., Sprooten, E., Kochunov, P., Olvera, R.L., Curran, J.E., Kent, J.W., Carless, M.A., Göring, H.H.H., Dyer, T.D., Duggirala, R., Almasy, L., Fox, P.T., Blangero, J., Glahn, D.C., 2014. Influence of age, sex and genetic factors on the human brain. Brain Imaging Behav. 8, 143–152. doi:10.1007/s11682-013-9277-5

Merluzzi, A.P., Dean, D.C., Adluru, N., Suryawanshi, G.S., Okonkwo, O.C., Oh, J.M., Hermann, B.P., Sager, M.A., Asthana, S., Zhang, H., Johnson, S.C., Alexander, A.L., Bendlin, B.B., 2016. Age-dependent differences in brain tissue microstructure assessed with neurite orientation dispersion and density imaging. Neurobiol. Aging 43, 79–88. doi:10.1016/j.neurobiolaging.2016.03.026

Mills, K.L., Goddings, A.-L., Herting, M.M., Meuwese, R., Blakemore, S.-J., Crone, E.A., Dahl, R.E., Güroğlu, B., Raznahan, A., Sowell, E.R., Tamnes, C.K., 2016. Structural brain development between childhood and adulthood: Convergence across four longitudinal samples. Neuroimage 141, 273–281. doi:10.1016/j.neuroimage.2016.07.044

Montagni, I., Cariou, T., Tzourio, C., González-Caballero, J.-L., 2019. "I don't know", "I'm not sure", "I don't want to answer": a latent class analysis explaining the informative value of nonresponse options in an online survey on youth health. Int. J. Soc. Res. Methodol. 1–17. doi:10.1080/13645579.2019.1632026

Mori, S., Oishi, K., Jiang, H., Jiang, L., Li, X., Akhter, K., Hua, K., Faria, A.V., Mahmood, A., Woods, R., Toga, A.W., Pike, G.B., Neto, P.R., Evans, A., Zhang, J., Huang, H., Miller, M.I., van Zijl, P., Mazziotta, J., 2008. Stereotaxic white matter atlas based on diffusion tensor imaging in an ICBM template. Neuroimage 40, 570–582. doi:10.1016/j.neuroimage.2007.12.035

Mutlu, A.K., Schneider, M., Debbané, M., Badoud, D., Eliez, S., Schaer, M., 2013. Sex differences in thickness, and folding developments throughout the cortex. Neuroimage 82, 200–207. doi:10.1016/j.neuroimage.2013.05.076

Nordenskjöld, R., Malmberg, F., Larsson, E.-M., Simmons, A., Ahlström, H., Johansson, L., Kullberg, J., 2015. Intracranial volume normalization methods: considerations when investigating gender differences in regional brain volume. Psychiatry Res. 231, 227–235. doi:10.1016/j.pscychresns.2014.11.011

Oishi, K., Zilles, K., Amunts, K., Faria, A., Jiang, H., Li, X., Akhter, K., Hua, K., Woods, R., Toga, A.W., Pike, G.B., Rosa-Neto, P., Evans, A., Zhang, J., Huang, H., Miller, M.I., van Zijl, P.C.M., Mazziotta, J., Mori, S., 2008. Human brain white matter atlas: identification and assignment of common anatomical structures in superficial white matter. Neuroimage 43, 447–457. doi:10.1016/j.neuroimage.2008.07.009

Pausova, Z., Paus, T., Abrahamowicz, M., Bernard, M., Gaudet, D., Leonard, G., Peron, M., Pike, G.B., Richer, L., Séguin, J.R., Veillette, S., 2017. Cohort profile: the saguenay youth study (SYS). Int. J. Epidemiol. 46, e19. doi:10.1093/ije/dyw023

Petersen, R.C., Aisen, P.S., Beckett, L.A., Donohue, M.C., Gamst, A.C., Harvey, D.J., Jack, C.R., Jagust, W.J., Shaw, L.M., Toga, A.W., Trojanowski, J.Q., Weiner, M.W., 2010. Alzheimer's Disease Neuroimaging Initiative (ADNI): clinical characterization. Neurology 74, 201–209. doi:10.1212/WNL.0b013e3181cb3e25

Pfefferbaum, A., Sullivan, E.V., 2015. Cross-sectional versus longitudinal estimates of age-related changes in the adult brain: overlaps and discrepancies. Neurobiol. Aging 36, 2563–2567. doi:10.1016/j.neurobiolaging.2015.05.005

Pohl, K.M., Sullivan, E.V., Rohlfing, T., Chu, W.,

Kwon, D., Nichols, B.N., Zhang, Y., Brown, S.A., Tapert, S.F., Cummins, K., Thompson, W.K., Brumback, T., Colrain, I.M., Baker, F.C., Prouty, D., De Bellis, M.D., Voyvodic, J.T., Clark, D.B., Schirda, C., Nagel, B.J., Pfefferbaum, A., 2016. Harmonizing DTI measurements across scanners to examine the development of white matter microstructure in 803 adolescents of the NCANDA study. Neuroimage 130, 194–213. doi:10.1016/j.neuroimage.2016.01.061

Potvin, O., Dieumegarde, L., Duchesne, S., Alzheimer's Disease Neuroimaging Initiative, 2017. Normative morphometric data for cerebral cortical areas over the lifetime of the adult human brain. Neuroimage 156, 315–339. doi:10.1016/j.neuroimage.2017.05.019

Raznahan, A., Lee, Y., Stidd, R., Long, R., Greenstein, D., Clasen, L., Addington, A., Gogtay, N., Rapoport, J.L., Giedd, J.N., 2010. Longitudinally mapping the influence of sex and androgen signaling on the dynamics of human cortical maturation in adolescence. Proc Natl Acad Sci USA 107, 16988–16993. doi:10.1073/pnas.1006025107

Raznahan, A., Shaw, P., Lalonde, F., Stockman, M., Wallace, G.L., Greenstein, D., Clasen, L., Gogtay, N., Giedd, J.N., 2011. How does your cortex grow? J. Neurosci. 31, 7174–7177. doi:10.1523/JNEUROSCI.0054-11.2011

Reuter, M., Tisdall, M.D., Qureshi, A., Buckner, R.L., van der Kouwe, A.J.W., Fischl, B., 2015. Head motion during MRI acquisition reduces gray matter volume and thickness estimates. Neuroimage 107, 107–115. doi:10.1016/j.neuroimage.2014.12.006

Ritchie, S.J., Cox, S.R., Shen, X., Lombardo, M.V., Reus, L.M., Alloza, C., Harris, M.A., Alderson, H.L., Hunter, S., Neilson, E., Liewald, D.C.M., Auyeung, B., Whalley, H.C., Lawrie, S.M., Gale, C.R., Bastin, M.E., McIntosh, A.M., Deary, I.J., 2018. Sex Differences in the Adult Human Brain: Evidence from 5216 UK Biobank Participants. Cereb. Cortex 28, 2959–2975. doi:10.1093/cercor/bhy109

Roalf, D.R., Quarmley, M., Elliott, M.A., Satterthwaite, T.D., Vandekar, S.N., Ruparel, K., Gennatas, E.D., Calkins, M.E., Moore, T.M., Hopson, R., Prabhakaran, K., Jackson, C.T., Verma, R., Hakonarson, H., Gur, R.C., Gur, R.E., 2016. The impact of quality assurance assessment on diffusion tensor imaging outcomes in a large-scale population-based cohort. Neuroimage 125, 903–919. doi:10.1016/j.neuroimage.2015.10.068

R Core Team, 2018. R: A Language and Environment for Statistical Computing.

Sachdev, P.S., Brodaty, H., Reppermund, S., Kochan, N.A., Trollor, J.N., Draper, B., Slavin, M.J., Crawford, J., Kang, K., Broe, G.A., Mather, K.A., Lux, O., Memory and Ageing Study Team, 2010. The Sydney Memory and Ageing Study (MAS): methodology and baseline medical and neuropsychiatric characteristics of an elderly epidemiological non-demented cohort of Australians aged 70-90 years. Int. Psychogeriatr. 22, 1248–1264. doi:10.1017/S1041610210001067

Sachdev, P.S., Lammel, A., Trollor, J.N., Lee, T., Wright, M.J., Ames, D., Wen, W., Martin, N.G., Brodaty, H., Schofield, P.R., OATS research team, 2009. A comprehensive neuropsychiatric study of elderly twins: the Older Australian Twins Study. Twin Res. Hum. Genet. 12, 573–582. doi:10.1375/twin.12.6.573

Salat, D.H., Greve, D.N., Pacheco, J.L., Quinn, B.T., Helmer, K.G., Buckner, R.L., Fischl, B., 2009. Regional white matter volume differences in nondemented aging and Alzheimer's disease. Neuroimage 44, 1247–1258. doi:10.1016/j.neuroimage.2008.10.030

Satterthwaite, T.D., Connolly, J.J., Ruparel, K., Calkins, M.E., Jackson, C., Elliott, M.A., Roalf, D.R., Hopson, R., Prabhakaran, K., Behr, M., Qiu, H., Mentch, F.D., Chiavacci, R., Sleiman, P.M.A., Gur, R.C., Hakonarson, H., Gur, R.E., 2016. The Philadelphia Neurodevelopmental Cohort: A publicly available resource for the study of normal and abnormal brain development in youth. Neuroimage 124, 1115–1119. doi:10.1016/j.neuroimage.2015.03.056

Schumann, G., Loth, E., Banaschewski, T., Barbot, A., Barker, G., Büchel, C., Conrod, P.J., Dalley, J.W., Flor, H., Gallinat, J., Garavan, H., Heinz, A., Itterman, B., Lathrop, M., Mallik, C., Mann, K., Martinot, J.L., Paus, T., Poline, J.B., Robbins, T.W., IMAGEN consortium, 2010. The IMAGEN study: reinforcement-related behaviour in normal brain function and psychopathology. Mol. Psychiatry 15, 1128–1139. doi:10.1038/mp.2010.4

Seiler, S., Pirpamer, L., Hofer, E., Duering, M., Jouvent, E., Fazekas, F., Mangin, J.-F., Chabriat, H., Dichgans, M., Ropele, S., Schmidt, R., 2014. Magnetization transfer ratio relates to cognitive impairment in normal elderly. Front. Aging Neurosci. 6, 263. doi:10.3389/fnagi.2014.00263

Seshadri, S., Wolf, P.A., Beiser, A., Elias, M.F., Au, R., Kase, C.S., D'Agostino, R.B., DeCarli, C., 2004. Stroke risk profile, brain volume, and cognitive function: the Framingham Offspring Study. Neurology 63, 1591–1599. doi:10.1212/01.wnl.0000142968.22691.70

Simmonds, D.J., Hallquist, M.N., Asato, M., Luna, B., 2014. Developmental stages and sex differences

of white matter and behavioral development through adolescence: a longitudinal diffusion tensor imaging (DTI) study. Neuroimage 92, 356–368. doi:10.1016/j.neuroimage.2013.12.044

Slater, D.A., Melie-Garcia, L., Preisig, M., Kherif, F., Lutti, A., Draganski, B., 2019. Evolution of white matter tract microstructure across the life span. Hum. Brain Mapp. 40, 2252–2268. doi:10.1002/hbm.24522

Smith, S.M., Jenkinson, M., Johansen-Berg, H., Rueckert, D., Nichols, T.E., Mackay, C.E., Watkins, K.E., Ciccarelli, O., Cader, M.Z., Matthews, P.M., Behrens, T.E.J., 2006. Tract-based spatial statistics: voxelwise analysis of multi-subject diffusion data. Neuroimage 31, 1487–1505. doi:10.1016/j.neuroimage.2006.02.024

Smith, S.M., Jenkinson, M., Woolrich, M.W., Beckmann, C.F., Behrens, T.E.J., Johansen-Berg, H., Bannister, P.R., De Luca, M., Drobnjak, I., Flitney, D.E., Niazy, R.K., Saunders, J., Vickers, J., Zhang, Y., De Stefano, N., Brady, J.M., Matthews, P.M., 2004. Advances in functional and structural MR image analysis and implementation as FSL. Neuroimage 23 Suppl 1, S208-19. doi:10.1016/j.neuroimage.2004.07.051

Sotiras, A., Toledo, J.B., Gur, R.E., Gur, R.C., Satterthwaite, T.D., Davatzikos, C., 2017. Patterns of coordinated cortical remodeling during adolescence and their associations with functional specialization and evolutionary expansion. Proc Natl Acad Sci USA 114, 3527–3532. doi:10.1073/pnas.1620928114

Sowell, E.R., Peterson, B.S., Kan, E., Woods, R.P., Yoshii, J., Bansal, R., Xu, D., Zhu, H., Thompson, P.M., Toga, A.W., 2007. Sex differences in cortical thickness mapped in 176 healthy individuals between 7 and 87 years of age. Cereb. Cortex 17, 1550–1560. doi:10.1093/cercor/bhl066

Storsve, A.B., Fjell, A.M., Tamnes, C.K., Westlye, L.T., Overbye, K., Aasland, H.W., Walhovd, K.B., 2014. Differential longitudinal changes in cortical thickness, surface area and volume across the adult life span: regions of accelerating and decelerating change. J. Neurosci. 34, 8488–8498. doi:10.1523/JNEUROSCI.0391-14.2014

Suzuki, Y., Matsuzawa, H., Kwee, I.L., Nakada, T., 2003. Absolute eigenvalue diffusion tensor analysis for human brain maturation. NMR Biomed. 16, 257–260. doi:10.1002/nbm.848

Tamnes, C.K., Herting, M.M., Goddings, A.-L., Meuwese, R., Blakemore, S.-J., Dahl, R.E., Güroğlu, B., Raznahan, A., Sowell, E.R., Crone, E.A., Mills, K.L., 2017. Development of the Cerebral Cortex across Adolescence: A Multisample Study of Inter-Related Longitudinal Changes in Cortical Volume, Surface Area, and Thickness. J. Neurosci. 37, 3402–3412. doi:10.1523/JNEUROSCI.3302-16.2017

Tukey, J.W., 1977. Exploratory Data Analysis, 1st ed. Pearson, Reading, Mass.

Vijayakumar, N., Mills, K.L., Alexander-Bloch, A., Tamnes, C.K., Whittle, S., 2018. Structural brain development: A review of methodological approaches and best practices. Dev. Cogn. Neurosci. 33, 129–148. doi:10.1016/j.dcn.2017.11.008

Vos, S.B., Jones, D.K., Viergever, M.A., Leemans, A., 2011. Partial volume effect as a hidden covariate in DTI analyses. Neuroimage 55, 1566–1576. doi:10.1016/j.neuroimage.2011.01.048

Wajman, J.R., Mansur, L.L., Yassuda, M.S., 2018. Lifestyle Patterns as a Modifiable Risk Factor for Late-life Cognitive Decline: A Narrative Review Regarding Dementia Prevention. Curr. Aging Sci. 11, 90–99. doi:10.2174/1874609811666181003160225

Walhovd, K.B., Fjell, A.M., Reinvang, I., Lundervold, A., Dale, A.M., Eilertsen, D.E., Quinn, B.T., Salat, D., Makris, N., Fischl, B., 2005. Effects of age on volumes of cortex, white matter and subcortical structures. Neurobiol. Aging 26, 1261–70; discussion 1275. doi:10.1016/j.neurobiolaging.2005.05.020

Walhovd, K.B., Westlye, L.T., Amlien, I., Espeseth, T., Reinvang, I., Raz, N., Agartz, I., Salat, D.H., Greve, D.N., Fischl, B., Dale, A.M., Fjell, A.M., 2011. Consistent neuroanatomical age-related volume differences across multiple samples. Neurobiol. Aging 32, 916–932. doi:10.1016/j.neurobiolaging.2009.05.013

Wang, Y., Adamson, C., Yuan, W., Altaye, M., Rajagopal, A., Byars, A.W., Holland, S.K., 2012. Sex differences in white matter development during adolescence: a DTI study. Brain Res. 1478, 1–15. doi:10.1016/j.brainres.2012.08.038

Wardlaw, J.M., Smith, C., Dichgans, M., 2013. Mechanisms of sporadic cerebral small vessel disease: insights from neuroimaging. Lancet Neurol. 12, 483–497. doi:10.1016/S1474-4422(13)70060-7

Westlye, L.T., Walhovd, K.B., Dale, A.M., Bjørnerud, A., Due-Tønnessen, P., Engvig, A., Grydeland, H., Tamnes, C.K., Ostby, Y., Fjell, A.M., 2010. Life-span changes of the human brain white matter: diffusion tensor imaging (DTI) and volumetry. Cereb. Cortex 20, 2055–2068. doi:10.1093/cercor/bhp280

Whalley, L.J., Dick, F.D., McNeill, G., 2006. A life-course approach to the aetiology of late-onset dementias. Lancet Neurol. 5, 87–96. doi:10.1016/S1474-4422(05)70286-6

White, T., El Marroun, H., Nijs, I., Schmidt, M., van der Lugt, A., Wielopolki, P.A., Jaddoe, V.W.V., Hofman, A., Krestin, G.P., Tiemeier, H., Verhulst, F.C., 2013. Pediatric population-based neuroimaging and the Generation R Study: the intersection of developmental neuroscience and epidemiology. Eur. J. Epidemiol. 28, 99–111. doi:10.1007/s10654-013-9768-0

Whitmer, R.A., Gunderson, E.P., Quesenberry, C.P., Zhou, J., Yaffe, K., 2007. Body mass index in midlife and risk of Alzheimer disease and vascular dementia. Curr. Alzheimer Res. 4, 103–109. doi:10.2174/156720507780362047

Wierenga, L.M., Langen, M., Oranje, B., Durston, S., 2014. Unique developmental trajectories of cortical thickness and surface area. Neuroimage 87, 120–126. doi:10.1016/j.neuroimage.2013.11.010

Winkler, A.M., Sabuncu, M.R., Yeo, B.T.T., Fischl, B., Greve, D.N., Kochunov, P., Nichols, T.E., Blangero, J., Glahn, D.C., 2012. Measuring and comparing brain cortical surface area and other areal quantities. Neuroimage 61, 1428–1443. doi:10.1016/j.neuroimage.2012.03.026

Yang, H., Long, X.-Y., Yang, Y., Yan, H., Zhu, C.-Z., Zhou, X.-P., Zang, Y.-F., Gong, Q.-Y., 2007. Amplitude of low frequency fluctuation within visual areas revealed by resting-state functional MRI. Neuroimage 36, 144–152. doi:10.1016/j.neuroimage.2007.01.054

Zang, Y., Jiang, T., Lu, Y., He, Y., Tian, L., 2004. Regional homogeneity approach to fMRI data analysis. Neuroimage 22, 394–400. doi:10.1016/j.neuroimage.2003.12.030

Zhang, H., Schneider, T., Wheeler-Kingshott, C.A., Alexander, D.C., 2012. NODDI: practical in vivo neurite orientation dispersion and density imaging of the human brain. Neuroimage 61, 1000–1016. doi:10.1016/j.neuroimage.2012.03.072

Zou, Q.-H., Zhu, C.-Z., Yang, Y., Zuo, X.-N., Long, X.-Y., Cao, Q.-J., Wang, Y.-F., Zang, Y.-F., 2008. An improved approach to detection of amplitude of low-frequency fluctuation (ALFF) for resting-state fMRI: fractional ALFF. J. Neurosci. Methods 172, 137–141. doi:10.1016/j.jneumeth.2008.04.012

Supplementary material*

Content

*to manuscript "The MRi-Share database: brain imaging in a cross-sectional cohort of 1,870 university students", by Tsuchida A. et al.

Description of the ABACI pipelines

Schematic figures for each pipeline follow the general scheme used for the description of UKB pipelines in (Alfaro-Almagro et al., 2018) to facilitate the comparison.

T1 and T2-FLAIR structural pipeline

Supplemental Figure 1 shows a flow-chart of the structural pipeline.

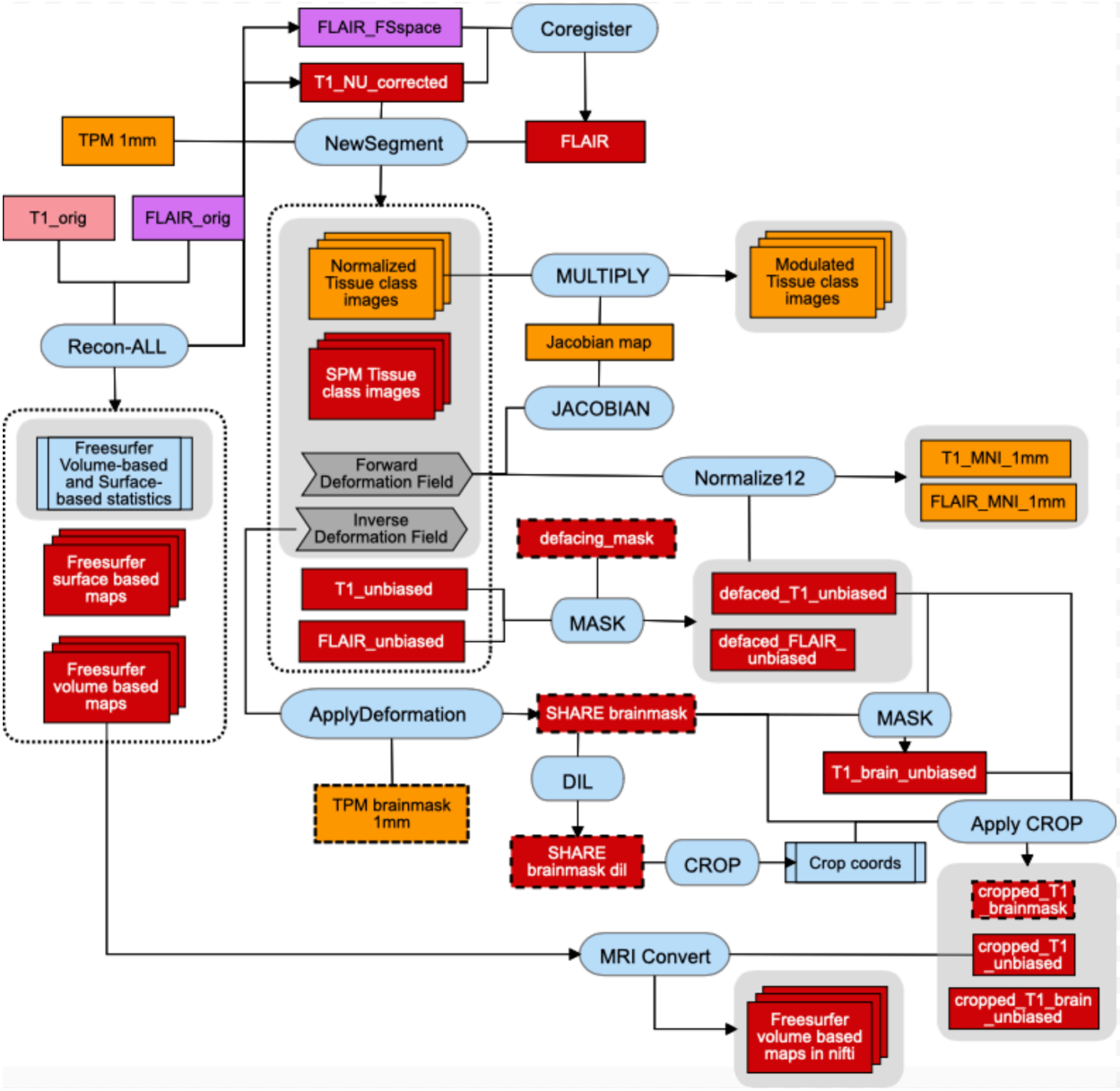

Supplemental Figure 1: Schematic representation of the structural pipeline.

In the surface-based processing branch of the structural pipeline, we used the 'recon-all' command of Freesurfer to reconstruct pial and white surfaces of the brain and to obtain both surface- and volume-based metrics from the T1 scan. Briefly, this involves non-parametric non-uniform intensity normalization (N3: Sled et al., 1998), linear transformation to the MNI305 template for estimation of intracranial volume (eTIV), intensity normalization that scales the mean intensity of the white matter to 110, skull-stripping, volume-based linear and non-linear registration to a probabilistic brain atlas for labelling of subcortical structures (Fischl et al., 2004, 2002), and surface-based registration for automatic cortical parcellation (Dale et al., 1999). We used the 'recon-all' command with '-FLAIRpial' multi-channel option to use FLAIR for refining the pial surface, and '-3T' option to use optimized parameters for the N3 correction for data acquired at 3T (based on Zheng et al., 2009) as well as the use of a 3T-based MNI305 template. We also used '-brainstem-structures' to obtain segmentations of 4 brainstem structures (medulla oblongata, pons, midbrain and superior cerebellar peduncle; Iglesias et al., 2015b), and '-hippocampal-subfields-T1T2' flag with FLAIR image input to obtain multi-channel segmentations of hippocampal subfields (Iglesias et al., 2015a).

In a semi-independent branch of the pipeline for volume-based processing, we used the N3-corrected T1 generated by Freesurfer and the FLAIR coregistered to the T1 space as the inputs for multi-channel tissue segmentation using the 'Segment' function of SPM12. This is an extension of the 'Unified Segmentation' framework described in (Ashburner and Friston, 2005) which includes an improved registration method, the option for multi-channel segmentation, as well as the new default tissue probability map (TPM) based on T2-weighted and proton density imaging data from 549 healthy adults (Ashburner et al., 2014). Our initial analysis pipeline used the raw, rather than N3-corrected T1, as the main input, with FLAIR as the secondary input, and with the default parameter setting of 'Segment'. The output images were then used both to generate tissue class maps for creation of the cohort-specific tissue probability map (TPM) template and to compute the final tissue class maps for the voxel-based morphometry analysis. However, the detailed quality control (QC) of individual tissue maps revealed that using the cohort-specific TPM this way somehow greatly biased the GM estimation on frontal regions (Supplemental Figure 2 and 3). After testing in a small subset of subjects (N = 50) as described in the section "Optimization of SPM12 segmentation" below, we 1) used Freesurfer N3-corrected T1 as the main and FLAIR coregistered to the T1 as secondary input, 2) optimized smoothing and regularization parameters for the bias field correction within 'Segment' function, and 3) kept the default TPM packaged with SPM12, rather than the cohort-specific TPM template for the unified tissue segmentation and normalization.

Using the inverse deformation field output from this step, a standard-space brain mask created from the default TPM template was transformed into the native T1 space, and this mask was applied to the bias field corrected T1 to generate a brain-extracted T1. We also used a dilated brain mask in native T1 space to compute the cropping coordinates to reduce image dimension, removing some voxels outside the brain. We then applied the cropping to both the brain-extracted and non-extracted (but defaced) T1 images. These cropped T1 images serve as the reference anatomical space for aligning other image modalities, as well as for converting Freesurfer volume-based maps (e.g. cortical and subcortical parcellation maps) to nifti format.

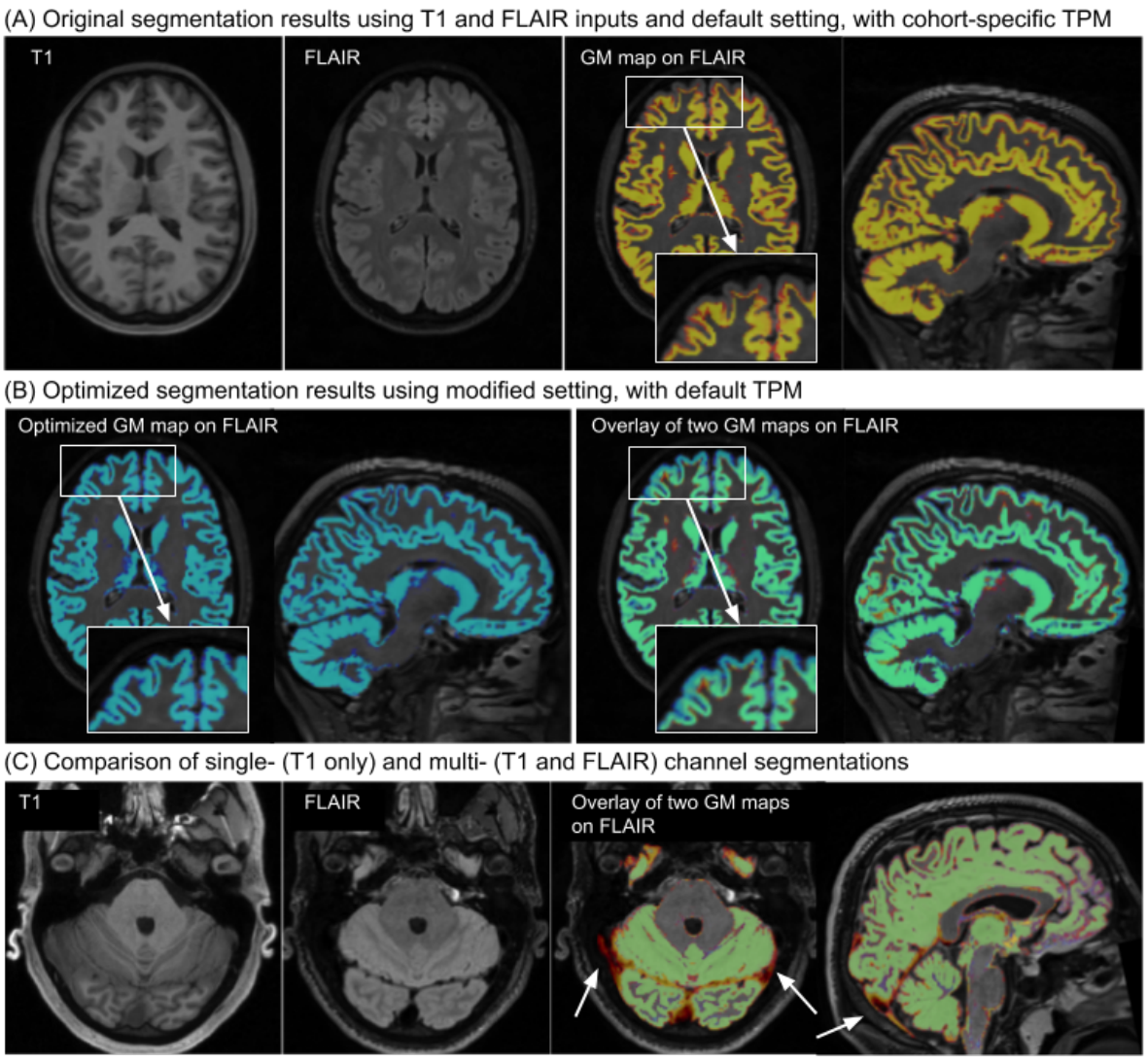

Supplemental Figure 2. Examples of segmentation failures in single- and multi-channel segmentation procedure in SPM12 and improvement after the optimization.

(A) original multi-channel segmentation using T1 and FLAIR inputs, with cohort-specific TPM and using default parameter settings of SPM12, (B) when using only T1 image, with default TPM and default parameter settings, and (C) when using the optimized procedure, with multi-channel segmentation with N3-corrected T1 and par2 setting. (A) and (B) show the same axial and sagittal slices from a representative subject, with T1 and FLAIR axial slices shown in the two left panels of (A). GM map from original segmentation is shown using warm color scale in (A) right, while that from optimized segmentation is shown using cold color scale in (B) left. (B) right shows the overlay of the original (warm) and optimized (color) GM maps. In (C) T1, FLAIR images of another subject (2 left panels), along with the overlay of the single- (warm color scale) and multi-channel (cold color scale) segmentation of GM maps (right panel) are shown. Arrows point to mis-segmentations of meninges as GM in single-channel, T1-only segmentation.

We computed the Jacobian modulation using the 'Deformations' utility in SPM12, and used this image to scale the spatially normalized tissue class maps for the final morphometric

analysis. We used this approach rather than outputting the “modulated” normalized tissue class maps directly from ‘Segment’, due to prominent artifacts (see Supplemental Figure 4 for an example) possibly related to ‘aliasing artifacts’ mentioned by the creators of SPM12 (Ashburner et al., 2014).

For Freesurfer-based IDPs, we extracted surface- (CT, inner CSA, and volume for each region of Desikan-Killiany, DKT, and Destrieux cortical atlas regions, as well as pial CSA for Desikan-Killany regions) and volume-based metrics by extracting values from lh/rh.aparc.stats and aseg.stats tables generated automatically with ‘recon-all’ function. For pial CSA, we used ‘mris_anatomical_stats’ function to generate additional summary tables for each region in DKT and Destrieux atlases, and extracted values from these tables.

For SPM-based IDPs, we computed total tissue volumes from Jacobian-modulated tissue class maps for GM, WM, and CSF. Additionally, Harvard-Oxford cortical and subcortical atlases (Desikan et al., 2006; Frazier et al., 2005; Goldstein et al., 2007; Makris et al., 2006) and Diedrichsen probabilistic cerebellar atlas (Diedrichsen et al., 2009) were used to obtain total tissue volumes within each region defined by these atlases. The cortical atlas was split by hemisphere to obtain tissue volume estimates separately for the left and right hemispheres.

Optimization of SPM12 segmentation

Initially, we created a cohort-specific TPM from the first 500 participants from the MRi-Share sample, and used this TPM for the unified segmentation and normalization procedure as implemented in SPM12, using all the default parameters and with multi-channel setting that used T1 and FLAIR images as inputs. However, the visual QC of the resulting GM segmentation image (Supplemental Figure 3A) showed underestimation of GM that was clearly visible across the majority of subjects and most prominent in frontal pole regions. The degree of underestimation was striking when compared against Freesurfer-based cortical segmentation in the same subject.

As the Freesurfer-based cortical segmentations were noticeably more accurate in many subjects, we decided to use the information about the discrepancy between Freesurfer- and SPM12-based segmentation to compare the effects of modifications on our SPM12 pipeline in a subset of the MRi-Share data (N = 50). More specifically, we computed and compared the mean of SPM12-based GM tissue probability (in native T1 space) inside the Freesurfer-based cortical parcellations after performing SPM12 segmentation procedure with the combinations of the following: 1) TPM (default TPM vs cohort-specific TPM), 2) input channel (T1 only vs multi-channel using T1 and FLAIR), 3) bias-field correction parameter setting of the SPM12 (*regularization* and the *bias field smoothing* settings: default vs two set of parameters as described below), and 4) bias-field correction on T1 *prior* to the correction applied internally within the SPM12 unified segmentation framework (none vs N3 vs N4 correction).

We compared the default and cohort-specific TPM, because it appeared that the use of default TPM seemed to mitigate the underestimation of the GM in frontal regions in our preliminary investigations. We also compared multi-channel (T1 + FLAIR) against T1-only segmentation since most published studies use only T1, although in theory multimodal segmentation should improve performance, and at least one study found empirically this to be the case (Lindig et al., 2018). We tested two different sets of bias-field correction parameter settings against the default since it has been reported that default correction parameters were

suboptimal both on simulated (Ganzetti et al., 2016a) and actual (Ganzetti et al., 2016b) MR images. While the default parameters for bias-field correction in SPM12 use 10^{-4} and 60 for the *regularization* and *bias-field smoothing*, respectively, Ganzetti *et al.* (2016a) reported 10^{-5} and 140 performed the best on their simulated 3T bias-field data, and in their second study (Ganzetti et al., 2016b) reported 10^{-2} and 30 to be the most optimal on the actual 3T dataset taken from the KIRBY21 database (https://www.nitrc.org/frs/shownotes.php?release_id=2178). We tested these three sets of settings (*def*: 10^{-4} and 60, *par2*: 10^{-5} and 140, *par3*: 10^{-2} and 30 for the *regularization* and *bias-field smoothing*, respectively). Even though this internal bias-field correction integrated with brain segmentation should be sufficient, and may even be superior to correction methods that are performed independently from segmentation (Ganzetti et al., 2016a), we tested the effects of applying two other commonly used correction methods, namely the N3 (Sled et al., 1998) and N4 (Tustison et al., 2010) prior to SPM12 segmentation.

Supplemental Figure 3 compares the degree of discrepancy between Freesurfer- and SPM12-based GM segmentation for different settings of the SPM12 as described above. They show that the use of cohort-specific TPM generally increases the discrepancy between the two algorithms (i.e. lower overall mean SPM12-based GM tissue inside Freesurfer-defined cortical GM), and also that the level of discrepancy becomes more variable across subjects, as indicated by larger standard deviations. Although single-channel segmentation using T1 image generally increases the amount of SPM12-based GM tissue inside Freesurfer-defined cortical GM, it also increases the amount of GM segmented *outside,* mis-segmenting the meninges around the cortex as GM (Supplemental Figure 2B). This is the case regardless of other parameter settings (e.g. Lindig et al., 2018), since meninges in T1 have similar contrast as GM. Within multi-channel segmentations using SPM12 default TPM, the amount of mean GM content discrepancy across cortical GM is similar across different T1 preprocessing options when using *def* or *par2* settings, but slightly worsens when using *par3* setting (Supplemental Figure 3A). However, region-by-region summary of GM content discrepancy shows that the discrepancy in the frontal pole region is most improved when using N3-corrected T1 image with *par2* setting (red arrows in Supplemental Figure 3B), without noticeably affecting the discrepancy in other regions. Visual inspection of the segmentation in a small number of subjects (Supplemental Figure 2C) corroborated this observation. Thus, for our pipeline we decided to 1) use SPM12 default TPM rather than cohort-specific template, 2) keep multi-channel with both T1 and FLAIR, but 3) use N3-corrected T1 from Freesurfer stream, and 4) adjust the *regularization* and *bias-field smoothing* settings in 'Segment' to 10^{-5} and 140, respectively.

(A) Comparison of mean SPM GM content in Freesurfer cortical GM

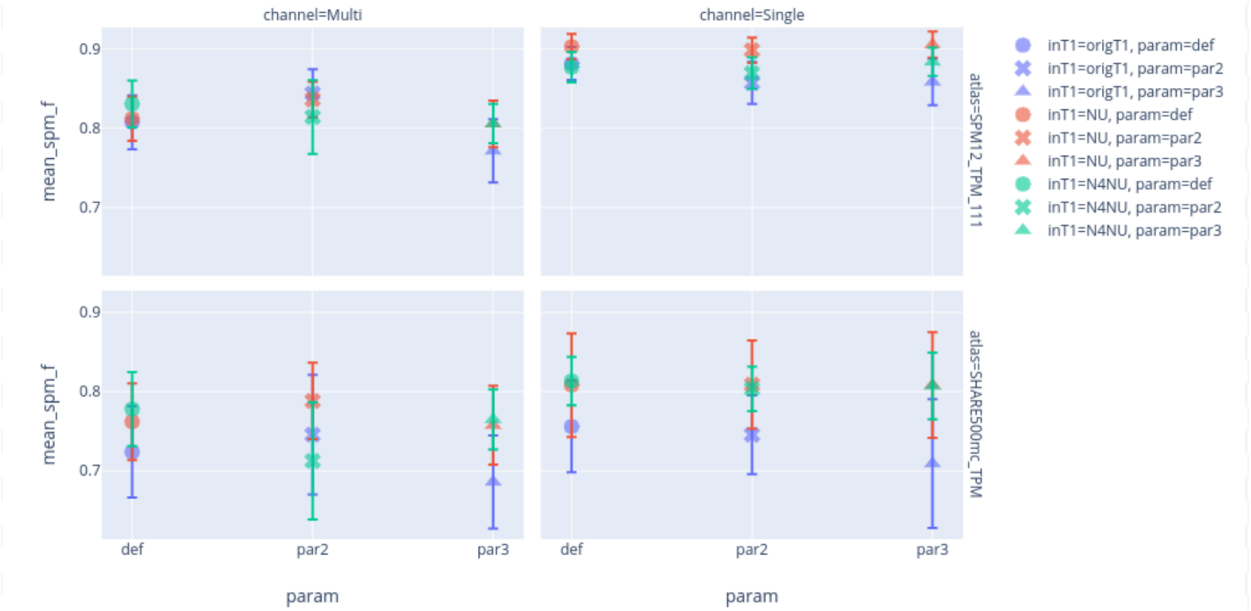

(B) Comparison of mean SPM GM content in Freesurfer Desikan cortical parcellation

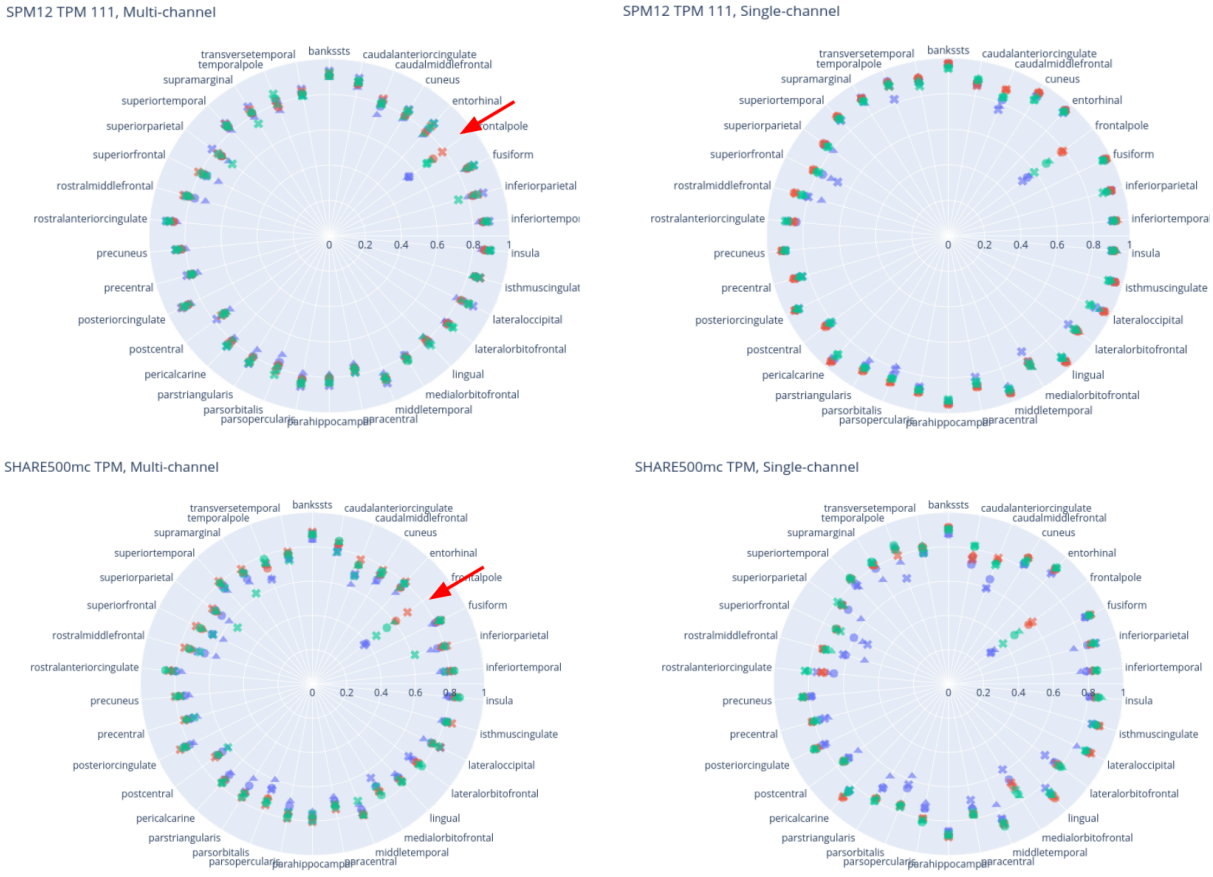

Supplemental Figure 3. Results of tests for optimizing SPM12 segmentation.

Plots show the amount of discrepancy between Freesurfer-based segmentation of the cortical GM and SPM12-based GM probability when using different inputs and parameter settings in SPM12 'Segment' as described in the text. They summarize the mean SPM-based GM content within (A) cortical GM and (B) each region of the Desikan cortical parcellation, as segmented by Freesurfer. The mean values are calculated across the subset of 50 MRiShare subjects, and the error bars indicate the standard deviation. In both (A) and (B), the colors of each data point indicate any bias field correction applied prior to performing 'Segment' (blue: no correction, pink: N3 correction based on Freesurfer, green: N4 correction using ANTS), and the symbols represent parameter settings in 'Segment' (circle: default setting, cross: par2 setting, triangle: par3 setting). Columns on the left use both T1 and FLAIR images as input (i.e. multi-channel segmentation), while the right columns only use T1 (i.e. single-channel segmentation). Upper rows in each (A) and (B) use the default TPM template upsampled to 1mm isotropic resolution, and lower rows use the cohort-specific template derived from 500 MRiShare subjects. Red arrows in (B) indicate the reduced discrepancy in the frontal pole region when using the N3-corrected T1 image with par2 settings.

Artefact in Jacobian-modulated maps produced by SPM12 'Segment' function

Jacobian-modulated maps of tissue class images in normalized space can be outputted directly in the 'Segment' function of SPM12 (denoted with prefix *mwc* for modulated, warped, class image). However, early visual inspection of this image revealed stripe-shaped artefacts in all images examined. These artefacts were not present if the modulated maps were produced "traditional" way by using the 'Deformations' utility in SPM12 to obtain the Jacobian modulation and then using it to scale the warped (i.e. spatially normalized) tissue class images (Supplemental Figure 4). Therefore, in our pipeline we included these extra steps to compute modulated tissue class images in normalized space rather than using the same map outputted directly from the 'Segment' function.

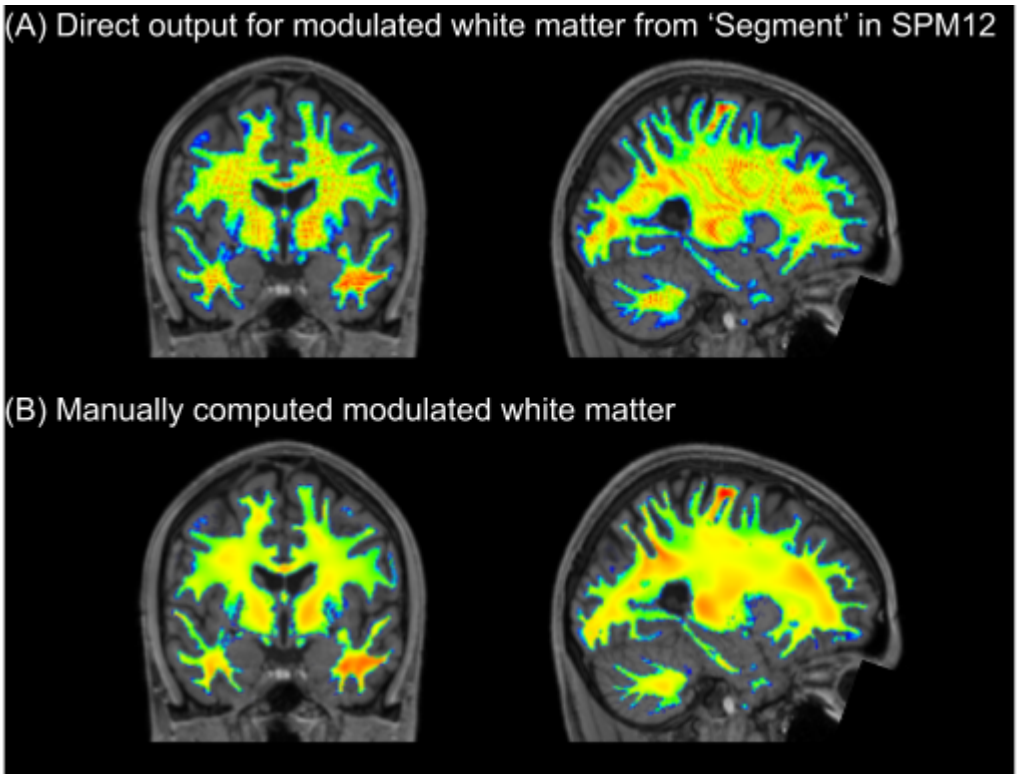

Supplemental Figure 4. Artefact in modulated maps produced by SPM12.

Images show (A) an example of striped artefacts observed in the modulated maps produced with the 'Segment' function in SPM12, and (B) the modulated map computed in the "traditional" way for the same subject. Selected coronal (left panel) and sagittal (right panel) views of the modulated white matter map, overlaid on T1 image warped to standard template space from a representative subject are shown.

Fieldmap generation pipeline

In the fieldmap generation pipeline (see Supplemental Figure 5), eight pairs of b=0 images with the opposing phase-encoding directions are extracted from DWI, merged, and fed into FSL TOPUP tool (Andersson et al., 2003). The resulting field coefficient map and movement parameter text file are kept for the later DWI processing pipeline. The TOPUP tool also produces unwarped, or distortion-corrected input b=0 images. The unwarped AP/PA b=0 images are averaged to create a fieldmap magnitude image, which is then skull-stripped with FSL BET tool (Smith, 2002), and linearly aligned to the reference T1 brain image using FSL FLIRT (Jenkinson et al., 2002; Jenkinson and Smith, 2001). The same linear transformation is also applied to the fieldmap phase image. Both the fieldmap phase and magnitude images in T1 structural space are kept for EPI unwarping in the later rs-fMRI pipeline.

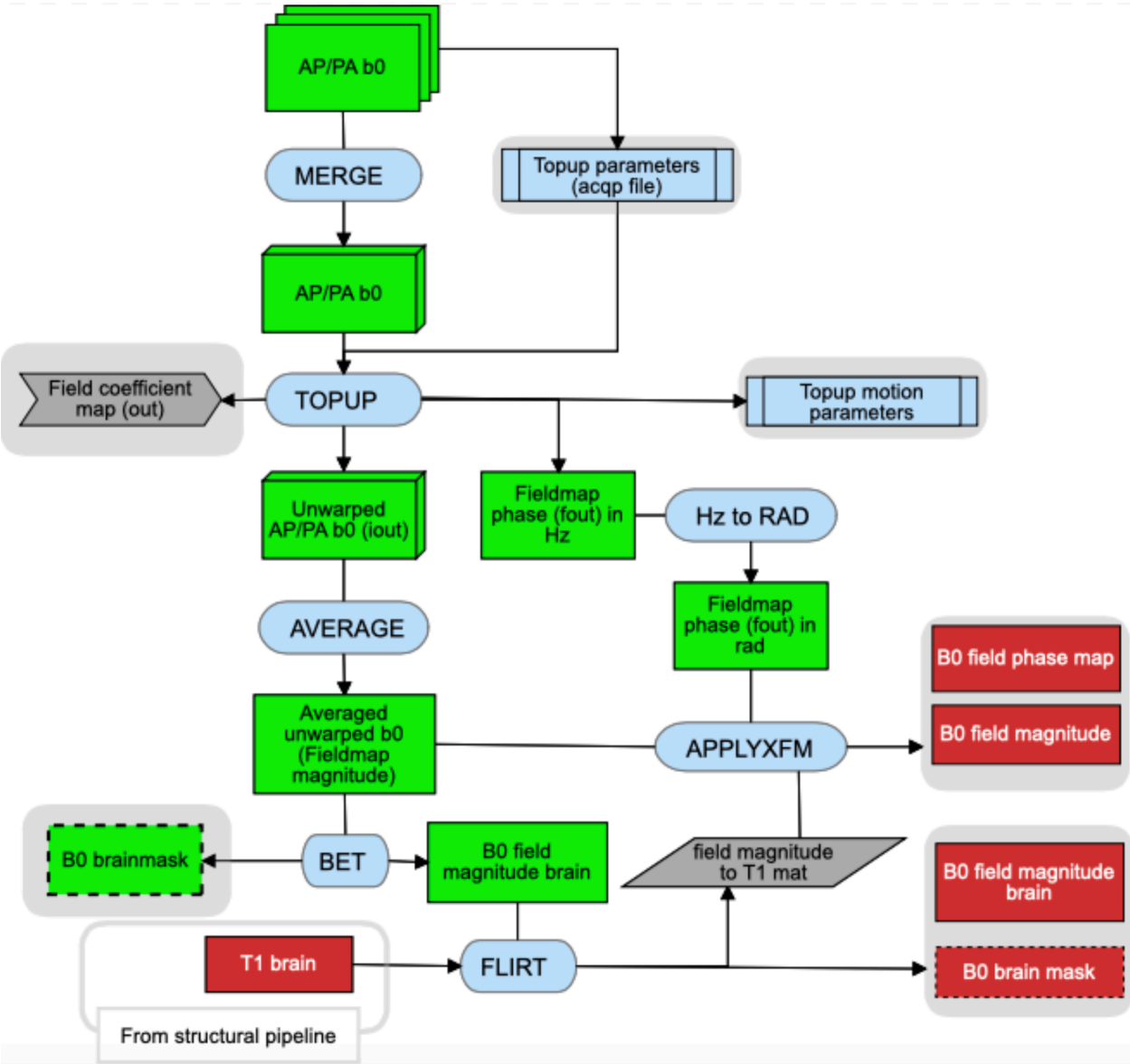

Supplemental Figure 5: Schematic representation of fieldmap generation pipeline

Diffusion MRI pipeline

Supplemental Figure 6 summarizes the DWI processing pipeline. In this pipeline, individual raw DWI data are first corrected for eddy current (EC) and top-up distortion using the FSL Eddy tool, with replacement of outlier slices (eddy_openmp as implemented in FSL v5.0.10 patch; (Andersson et al., 2016; Andersson and Sotiropoulos, 2016). After cropping the data to reduce non-brain tissue volumes, we apply non-local means filter to denoise and boost the SNR, using the 'nlmeans' denoising tool (Coupe et al., 2011, 2008) as implemented in the Dipy package (0.12.0; Garyfallidis et al., 2014). The resulting image is then used to estimate 1) DTI (Diffusion-Tensor Imaging; Basser et al., 1994) model parameters and 2) microstructural NODDI (Neurite Orientation Dispersion and Density Imaging; Zhang et al., 2012) model parameters. For DTI modelling, the volumes with high b-value (b=2000 s/mm^2) are removed from the denoised

data before fitting the data with the dipy tools (Jensen and Helpern, 2010) to compute DTI maps, namely the maps of maps of fractional anisotropy (FA), mean, axial, and radial diffusivity (MD, AD, and RD, respectively). The diffusivity maps were further cleaned by removing diffusivity value outliers using Random Sample Consensus (RANSAC) approach (Choi et al., 2009), as implemented in the scikit-learn package (0.19.1; https://scikit-learn.org/stable/index.html). The denoising, DTI computation, and the RANSAC outlier removal were performed by wrapping Scilpy scripts, developed by Sherbrooke Connectivity Imaging Lab (https://scilpy.readthedocs.io/en/latest/).

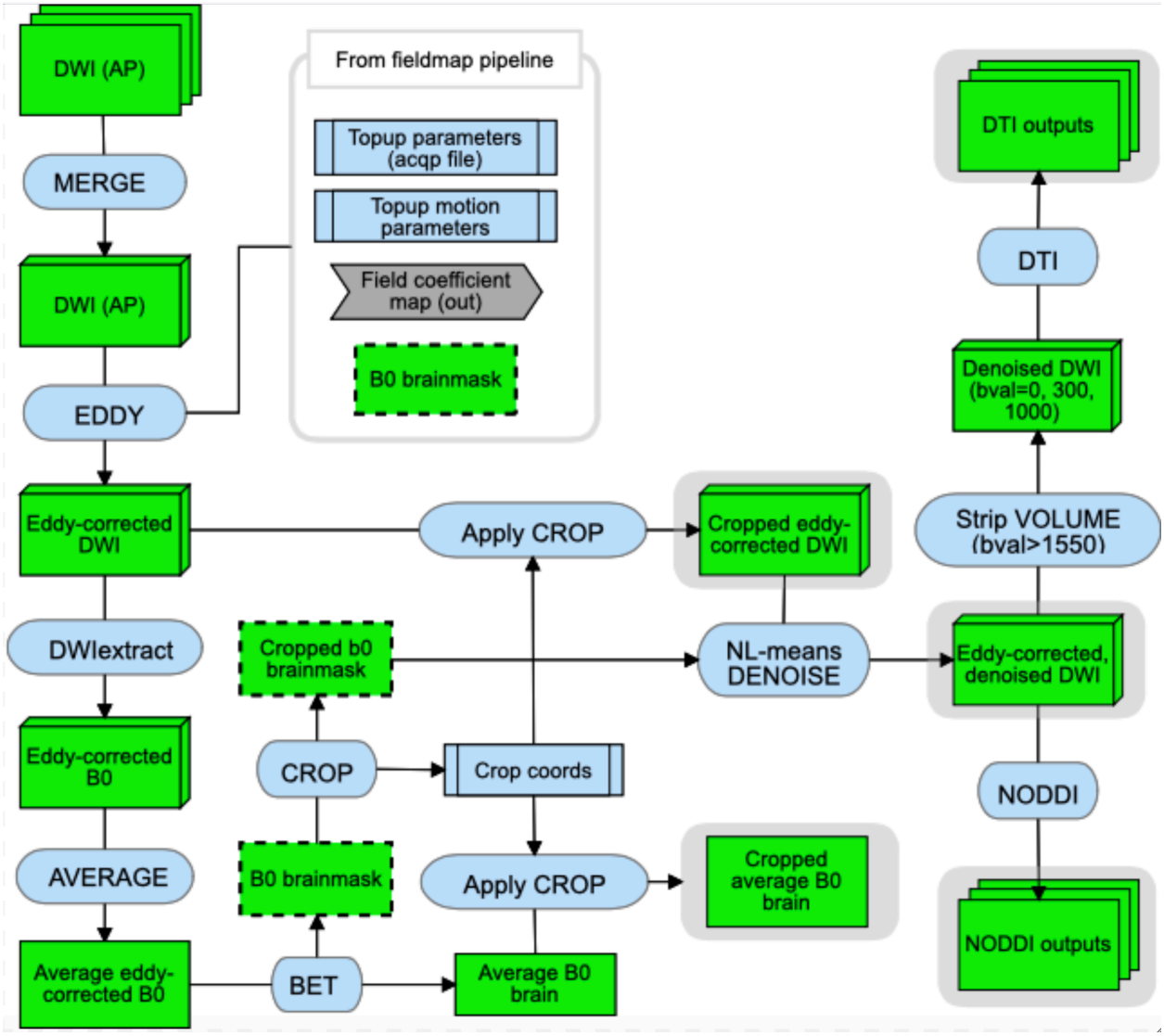

Supplemental Figure 6: Schematic representation of diffusion MRI pipeline

Before fitting denoised data for NODDI, we computed empirical values of cohort-specific isotropic and parallel diffusivity by computing the mean MD within lateral ventricles and mean AD within the corpus callosum in individual T1 space for each subject. The mean of these values across subjects were then used as dPar (1.5×10^{-3}) and dIso (2.4×10^{-3}) parameters in

the AMICO (Accelerated Microstructure Imaging via Convex Optimization) tool (Daducci et al., 2015) when fitting the denoised DWI data to obtain the following NODDI metric maps: isotropic volume fraction (IsoVF), which indicates the proportion of free water volume of each voxel, neurite density index (NDI), which represents the proportion of intracellular volume in the remaining fraction, and orientation dispersion index (ODI), a measure of within-voxel fiber dispersion.

In order to obtain mean DTI/NODDI metrics within cerebral WM, we used sub-workflows that first upsample and coregister DTI and NODDI maps in the native DWI space (1.7 mm isotropic) to the individual native T1 space (1mm isotropic), then compute mean values within a cerebral WM mask defined for each subject in their native T1 space. The coregistration sub-workflow used the '*antsRegistrationSyNQuick'* script in the ANTS package to compute a linear (rigid + affine) transform and symmetric diffeomorphic image normalization (deformable SyN; Avants et al., 2008) warp to align the eddy- and motion-corrected average b0 image, upsampled to match T1 resolution, to the individual T1 image, then applied the computed transform to the upsampled DTI and NODDI maps. The subject-specific cerebral WM mask was derived from the Freesurfer segmentation, but it was also refined by masking it with the SPM12-derived native WM tissue probability map thresholded at 0.5. This ensured that the mean DTI/NODDI values were computed within the cerebral WM regions with limited partial volume effects. Other IDPs using Freesurfer labels were generated in a similar fashion, with mean values calculated within each of the subject-specific labels, and then refined by masking it with either the SPM12-based WM (for WM regional labels) or GM (GM regional labels) mask.

To generate IDPs based on JHU ICBM-DTI-81 white matter labels atlas (Mori et al., 2008; Oishi et al., 2008), we used SPM12 'Coregister', followed by 'Normalize' function that used the deformation field generated in the structural pipeline to transform DTI/NODDI maps in the native DWI space to the standard template space (1mm isotropic) in one step. Here, subject-specific, spatially normalized WM class images (also 1mm isotropic) from the structural pipeline were thresholded at 0.5 and used as the mask when computing mean DTI/NODDI values within each region in the atlas.

Finally, IDPs based on spatially normalized WM skeleton were generated using a script based on Baykara et al. (http://www.psmd-marker.com, Baykara et al., 2016), and described in (Beaudet et al., 2020). Briefly, it used FSL TBSS (Smith et al., 2006) to obtain spatially normalized, skeletonized WM maps based on the FA maps for each individual. After removing voxels near the ventricles with a custom mask developed by Baykara et al. (2016), the voxel value distribution for each of the DTI metric was analyzed within the skeletonized WM mask, to obtain mean, standard deviation, and the value between the 95th and 5th percentile values.

Resting-state fMRI pipeline

The pipeline used for preprocessing the resting state fMRI (rs-fMRI) is sketched in the Supplemental Figure 7.

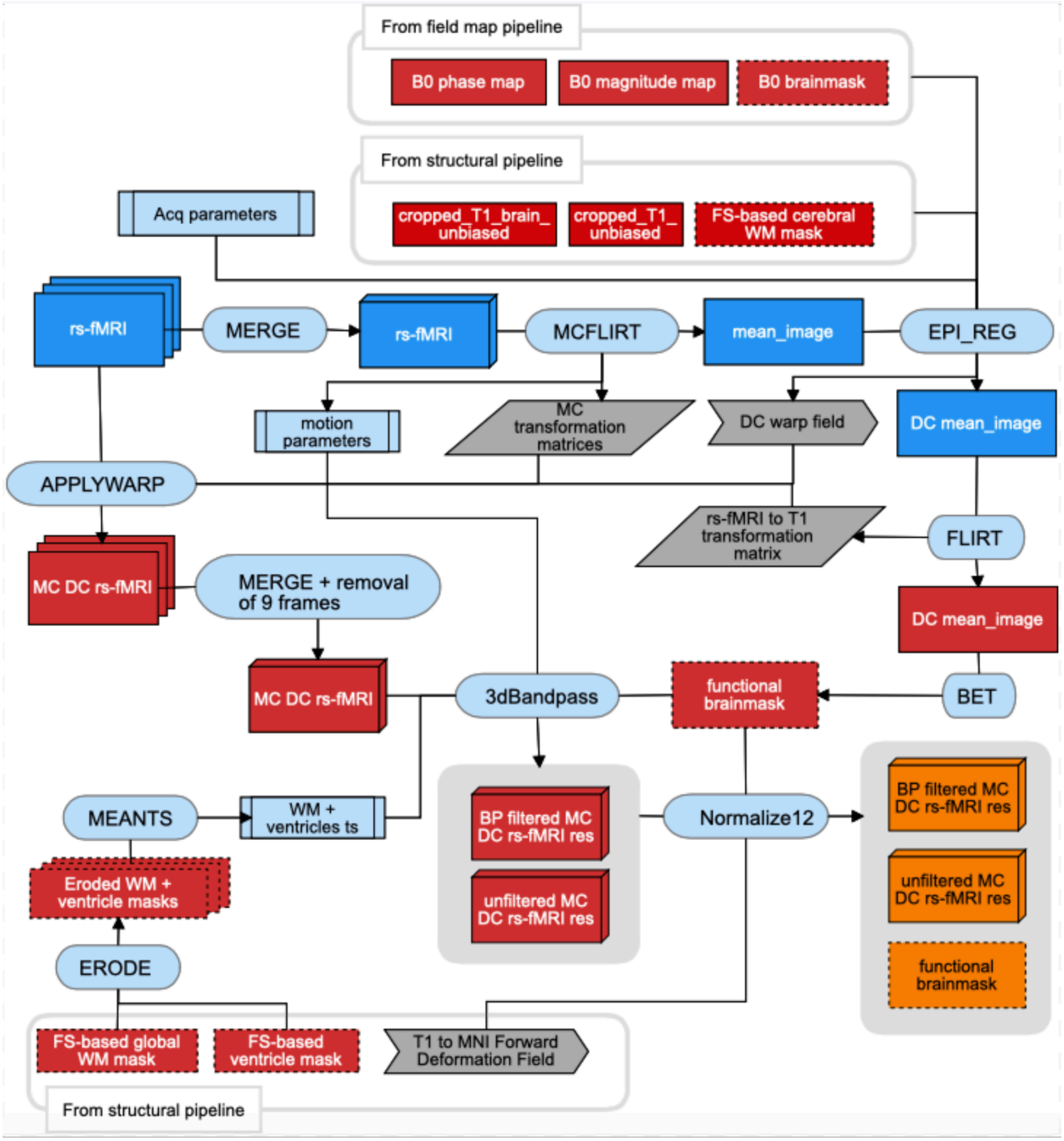

Supplemental Figure 7. Schematic representation of resting-state fMRI pipeline

Processing of the 15 minutes long rs-fMRI dataset requires additional data that have been processed with the structural and fieldmap generation pipelines (see above) including the b0-fieldmap, the T1-weighted volume, the nonlinear deformation field for stereotaxic transformation of the T1-weighted volume into the reference brain in the MNI standard space, and four masks based on FreeSurfer segmentation: 1) cerebral WM mask (not including corpus callosum), 2) global WM mask (cerebral WM with corpus callosum and cerebellar WM), 3) ventricle mask, and 4) brain mask.

The pipeline begins with the spatial alignment of the rs-fMRI data into the T1-weighted individual reference space using a 3-step procedure similar to the one described in Alfaro-Almagro et al. 2018. It includes motion correction with the FSL MCFLIRT (Jenkinson et al., 2002), followed by the combined echo-planar imaging (EPI) distortion correction and WM boundary-based registration (BBR) with the FSL 'epi_reg' script packaged with FSL FLIRT, and the final realignment to the T1 space with the FSL FLIRT (Jenkinson et al., 2002; Jenkinson and Smith, 2001). For the BBR, the Freesurfer-based WM mask was used, and the fieldmap phase and magnitude images were used for the EPI distortion correction. Both the BBR/distortion correction and post-BBR coregistrations were computed on the motion-corrected rs-fMRI mean image. For each volume of the rs-fMRI data, the spatial transformations for the three steps (motion correction, BBR/distortion correction, and post-BBR coregistration) were combined and applied together using the FSL 'applywarp' command, in order to minimize the number of interpolations. Note that the 9 first EPI volumes are removed from the analysis in order to take in account initial imperfect stabilisation of the signal. The FD that indexes the subject motion in the rs-fMRI, as described in (Power et al., 2014, 2012) was computed using the BRAMILA tools, developed by Brain and Mind Lab at Aalto University (https://users.aalto.fi/~eglerean/bramila.html).

Once in the individual T1 space, a brain mask was computed from rs-fMRI data with the FSL BET (Smith, 2002). This mask was applied when band-pass filtering the data using the AFNI 3dBandpass (Sforazzini et al., 2016). This step also included despiking and nuisance regression, using the times series of the Friston 24 motion parameters (Friston et al., 1996) and those extracted from the subject-specific, Freesurfer-based WM and ventricle masks. The WM and ventricle masks were eroded 3 and 2 times, respectively, but if the resulting mask contained less than 50 voxels, the mask with one less erosion was used to extract the nuisance time series. We used a frequency window of 0.01 to 0.1 Hz for the band-pass filtered data, and 0 to 99999 Hz to create unfiltered data with the identical despiking and nuisance regression. These images were then warped into the stereotaxic space using the SPM12 'Normalise' function with the deformation field from T1 space to the reference MNI brain generated in the structural pipeline, at a voxel sampling size of 2 mm isotropic.

For computing regional intrinsic connectivity (IC) matrices with and without global signal regression (GSR), the brain mask produced from the rs-fMRI data in T1 space was warped into the stereotaxic space using the same deformation field to transform the rs-fMRI data to the standard MNI space, and mean time series of the band-pass filtered data within this mask was extracted with FSL 'fslmeants'. This time series was then used as a regressor in FSL 'fsl_glm' function to obtain the residual of the band-pass filtered data. The band-pass filtered data with and without GSR were further cleaned to remove the effects of motion by scrubbing, in which we removed any volumes that exceeded the FD of 0.5mm (Power et al., 2014, 2012). We then extracted the average time series within each of the 384 regions (192 homotopic region pairs) of the AICHA atlas (Joliot et al., 2015) from these data, and computed the Pearson correlation coefficients (*r*) between every pair of regions to produce the two versions of regional IC matrices. When computing the group average IC matrices, any subjects with less than 75 % of a given AICHA region overlapping with the functional brain mask were excluded from the computation of the mean value for *r* involving that region (i.e. one row/column for the region).

The band-pass filtered data (but without any scrubbing or GSR) in the standard space were also used to compute three other properties of spontaneous brain activities at rest at a voxel-level: 1) regional homogeneity (ReHo; Zang et al., 2004) 2) amplitude of low frequency fluctuation (ALFF; Yang et al., 2007), and 3) fractional ALFF (fALFF; Zou et al., 2008). ReHo measures the degree of similarity in spontaneous fluctuations in the neighboring voxels, and thus shows how coherent the regional intrinsic neuronal activities are. It is computed as the average of the Kendal's coefficients of concordance between a given voxel time series and those of each of its 26 neighbors that are inside the brain mask. ALFF, in contrast, captures the total power of the regional intrinsic neuronal activity, and is computed as the integral of the square-root of the power spectrum of low-frequency (0.01 to 0.1 Hz) fluctuations in each voxel. Lastly, fALFF describes this low-frequency power as the fraction of total fluctuations in the entire range of frequency, which reportedly increases the sensitivity and specificity to the neuronal activity (Zou et al., 2008). To compute fALFF, the amplitude maps were created for both band-pass filtered and unfiltered data, and the ratio between the two were calculated for each voxel. All three maps were computed in the voxels inside the intersection between the functional brain mask and the Freesurfer-based brain mask, both in the spatially normalized space.

We also performed subject-level independent component analyses (ICA) using FSL MELODIC (Beckmann and Smith, 2004), after spatially smoothing the band-pass filtered data at full width at half maximum of 5 mm with AFNI 3dBlurInMask. The number of dimensions was estimated using the Laplace approximation to the Bayesian evidence of the model order in each subject (Beckmann and Smith, 2004; Minka, 2000)

Description of subject-level visual QC and quantitative QC metrics

Each pipeline in the ABACI generated a set of subject-level qualitative, visual QC images as well as quantitative QC metrics. As shown in Supplemental Figure 8, these were organized as linked HTML web pages, where a main page for each modality showed interactive distribution histograms for the main IDPs and/or QC metrics, with links to individual web pages for each participant through columns listing batch numbers and subject numbers per batch (each batch containing 50 subjects to avoid listing entire subjects in a single column). When a viewer hovers over the point in the scatterplot below the histogram (Supplemental Figure 8A), it shows the subject ID and the value of the metric for that subject, and when clicked, it opens the individual web page for that subject (Supplemental Figure 8B).

This way, it facilitates the detection and inspection of outliers for any given metrics within each pipeline. The interactive graphs embedded in the web pages were generated with custom python tools, using *bokeh* package (0.12.16, https://bokeh.org/). In sections below, we describe the QC procedures followed for each modality, as well as the details of qualitative and quantitative QC in each pipeline.

(A) Example of the main group-level QC web page

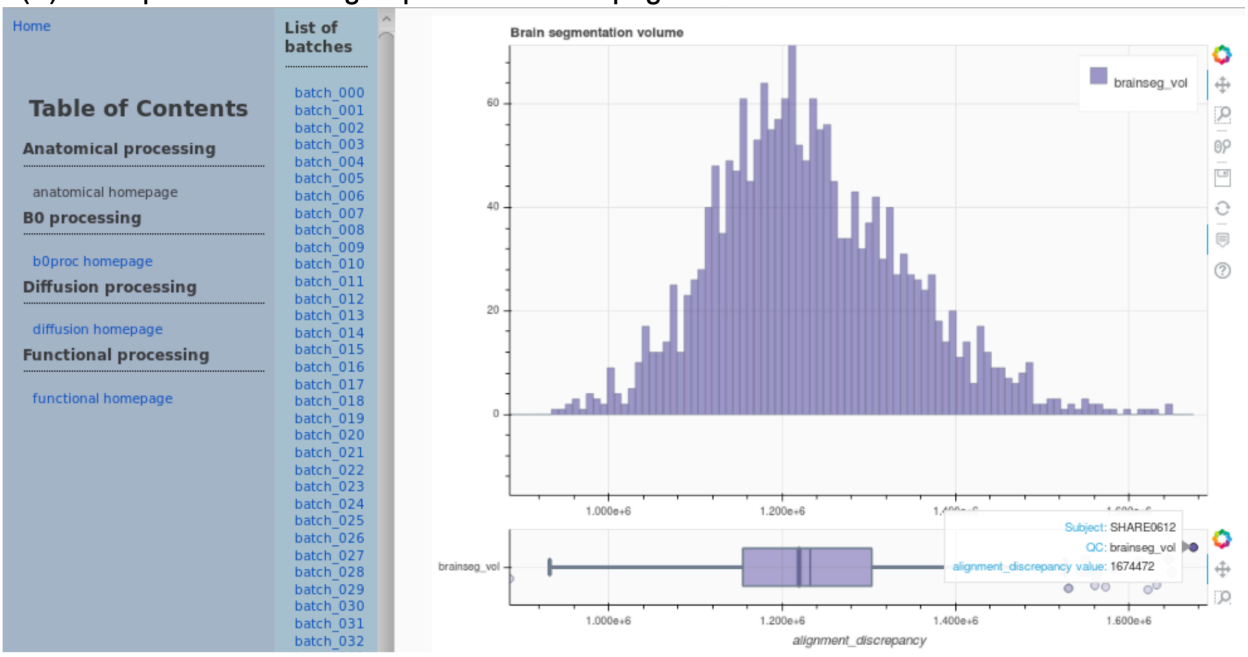

(B) Example of the individual-level QC web page

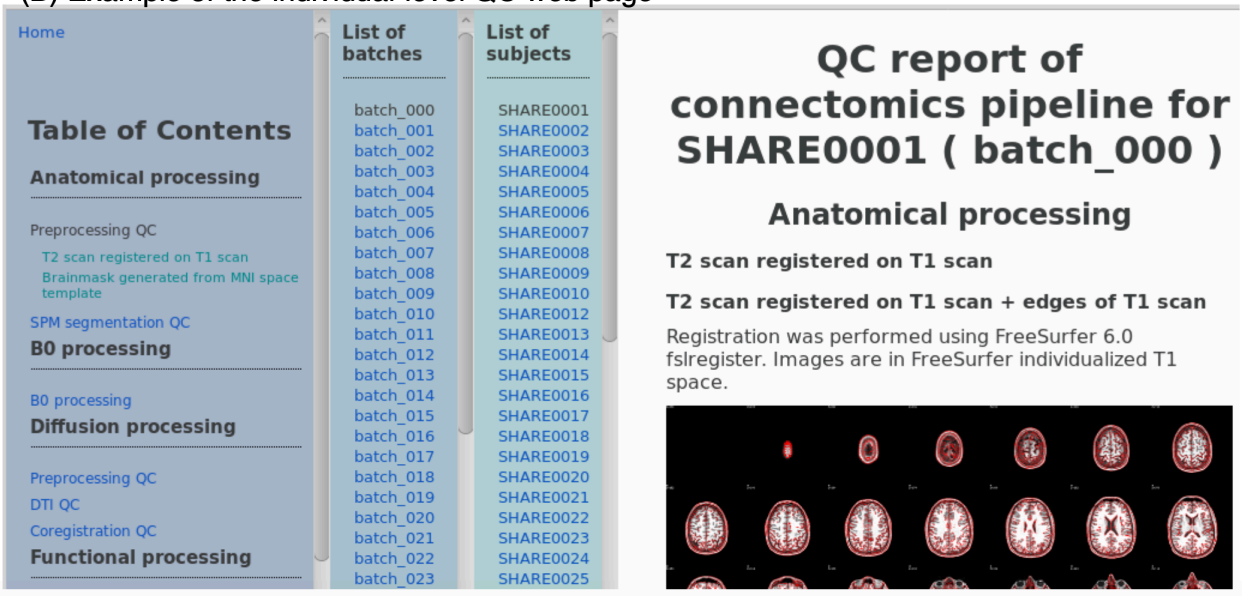

Supplemental Figure 8. Example of the QC web page produced by the ABACI.

The examples of linked QC HTML web pages generated by the ABACI pipelines are shown for the structural pipeline. (A) The main page for the structural pipeline containing the distributions of selected IDPs as interactive histogram and scatter plot. The snapshot was taken when hovering over the subject with highest Freesurfer-segmented brain volume. Clicking on it would open the linked individual-level structural QC page for that subject. (B) An example of the individual-level QC page for the structural pipeline.

Structural MRI processing QC

As a first step, the same three qualified MD investigators (B.M, E.M, and N.T-M) who reviewed raw T1 and FLAIR images for any incidental findings and non-incidental anomalies also flagged any images with visible artefacts, such as ringing and reduced contrast in the raw images. A trained rater (A.T) then rated the flagged images on four categories according to the rating system proposed by Backhausen et al. (2016); 1) Image sharpness, 2) Ringing, 3) Contrast to noise ratio (CNR) of subcortical structures, and 4) CNR of GM and WM. For each category, scores were given such that 0, 1, and 2 represented 'good', 'moderate', and 'bad' quality as described by Backhausen et al. (2016). Supplemental Figure 9 shows the example raw T1 and FLAIR images in a subject who received the worst score for T1 as well as combined T1 and FLAIR, along with the two representative output images from the two streams of structural pipeline. They show that despite the visible artefacts in both T1 and FLAIR images in this subject, there are no major failures in the tissue segmentation by SPM12 or in the surface- and volume-based segmentations in Freesurfer.

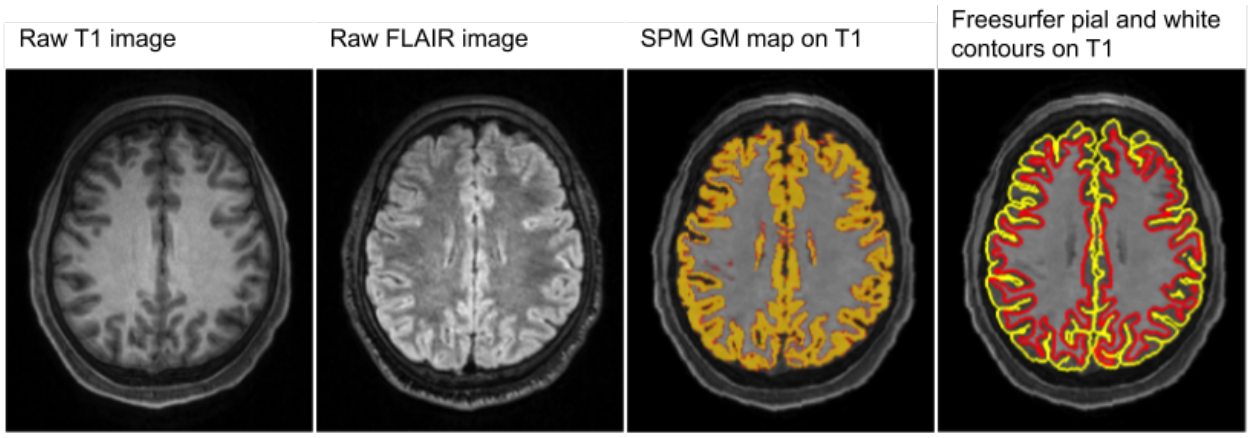

Supplemental Figure 9. Examples of visible artefacts flagged at the initial check of raw T1 and FLAIR images.

Images show raw T1 (left most panel) and FLAIR (second left) images of a subject flagged by the initial review by an MD investigator and later received the worst score of 8 (4 for T1 and FLAIR respectively, using a method suggested by Backhausen et al., 2016). A faint ringing is visible on T1 image, which is also present and more visible on FLAIR image as well. Noise within the white matter is also visible on the FLAIR image. Despite receiving the worst rating for the combined quality of T1 and FLAIR images, both SPM12-based tissue segmentation (third left) and Freesurfer-based surface reconstruction (right most panel) do not present any major problems.

Independently of the initial flagging of the artefacts, another trained rater (N.B) inspected individual qualitative QC images produced by our pipeline for all scanned participants. These images included the following (see Supplemental Figure 10 for examples of each):

- Multiple axial slices of T1 image with contours of coregistered FLAIR image for checking FLAIR-to-T1 coregistration
- Multi-axial slices of T1 image with brain mask overlay to check the quality of brain mask
- Multiple axial, sagittal, coronal slices of gray and white matter segmented with SPM12, overlaid on FLAIR image to inspect the quality of tissue segmentation

- Jacobian modulated gray and white matter overlaid on the T1 image warped to the template space to check for any unusual deformation.

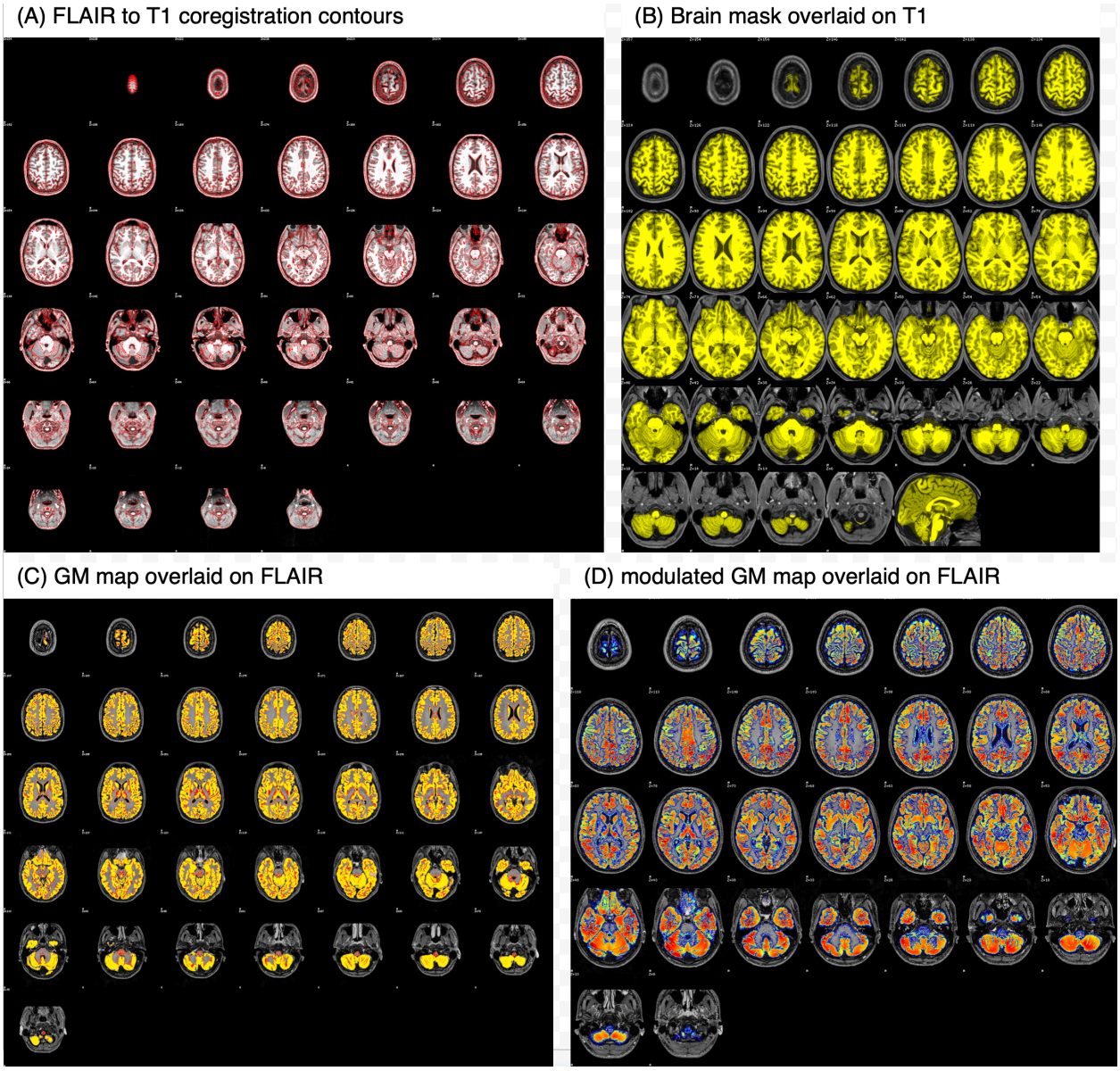

Supplemental Figure 10. Examples of subject-level visual QC images for T1 and FLAIR structural pipeline.

(A) Multiple axial slices of T1 image with contours of coregistered FLAIR image for checking FLAIR-to-T1 coregistration, (B) multi-axial slices of T1 image with brain mask overlaid on them to check the quality of the mask, (C) GM map in native T1 space created by SPM12 overlaid on FLAIR image coregistered to T1 to check the quality of SPM12 tissue segmentation, and (D) modulated GM map overlaid on FLAIR image in the stereotaxic space to check any abnormal deformation. QC images similar to (C) and (D) were created for WM maps as well, and images showing multi-coronal as well as multi-sagittal slices were created for both GM and WM maps.

The same rater also inspected another set of images and movies produced by a modified version of ENIGMA Cortical QC scripts (package 2.0, April 2017: http://enigma.ini.usc.edu/protocols/imaging-protocols/) that generated multiple views of Freesurfer surface reconstructions and cortical and subcortical parcellations to spot any gross failures in surface reconstruction. The rater followed the ENIGMA Cortical Quality Control Guide 2.0 April 2017 to check for any problems at the regional level in the Desikan cortical parcellation of each subject. While the inspection at the regional level revealed segmentation problems known to be relatively common, no major failures were found at the global surface reconstructions in 1,832 subjects examined. There were also no extreme outliers in global surface-based measures (mean CT, inner and pial CSA) or in volumetric variables (total GM and WM volumes; see Supplemental Figure 16 below in "Additional statistical analysis")

Supplemental Figure 11A shows the distributions of QC metrics computed as part of the structural pipeline and an additional sub-workflow that used the main segmentation output images to compute tissue signal-to-noise (SNR) and contrast-to-noise (CNR). More specifically, we computed:

- Cost function values for FLAIR to T1 coregistration
- Within-tissue SNR in GM and WM (defined as mean divided by standard deviation of the intensity values within these tissues)
- GM-to-WM or GM-to-CSF CNR (defined as the ratio of GM to WM or GM to CSF mean intensity values) for both T1 and FLAIR images, using SPM12-based tissue segmentations.

Similarly to UKB QC IDPs (Alfaro-Almagro et al., 2018), inverse values were computed for both SNR and CNR so as to make higher values of all the QC metrics represent worse quality.

We also computed the following QC metrics to check the distribution and outliers (Supplemental Figure 11B), and to explore their impact on morphometric measures of interest in our future investigation:

- Mean Euler number from the Freesurfer processing, which represents the topological complexity of the reconstructed cortical surface, and which was proposed to be a better index of data quality in structural scan (Rosen et al., 2018)
- Freesurfer total CNR based on *mri_cnr* tool packaged with Freesurfer
- tAverage edge strength (AES) measure, a recently proposed method for retrospectively quantifying the head motion from the structural scan (Zacà et al., 2018).
- Qoala-T score, a new metric for Freesurfer segmented MRI data, which has been proposed as a new quality metric that can be used to compare the quality of data across different datasets with differing acquisition parameters (Klapwijk et al., 2019).

The mean Euler number and AES have been shown in prior studies to affect the age effect estimate on cortical thickness (Madan, 2018; Rosen et al., 2018), even when the most problematic of the images are removed from the analyses. Of note, the mean framewise displacement (FD) from functional MRI (Power et al., 2012) has also been demonstrated to affect the structural morphometry (Madan, 2018; Reuter et al., 2015; Rosen et al., 2018; Savalia et al., 2017). We note that Qoala-T scores in our MRi-Share dataset is particularly high (mean ±

standard deviation [range] = 74.9 ± 9.7 [49.7 - 96.4] %, the maximum score is 100 %), with no images classified below the score of 30%, which is a suggested cut-off for exclusion without further visual QC (Klapwijk et al., 2019). Note that the direction of these extra QC metrics were not manipulated, in order to facilitate the comparison with prior studies using these metrics. The lower values in AES score, Freesurfer Euler number and total CNR, and Qoala-T score represent worse quality.

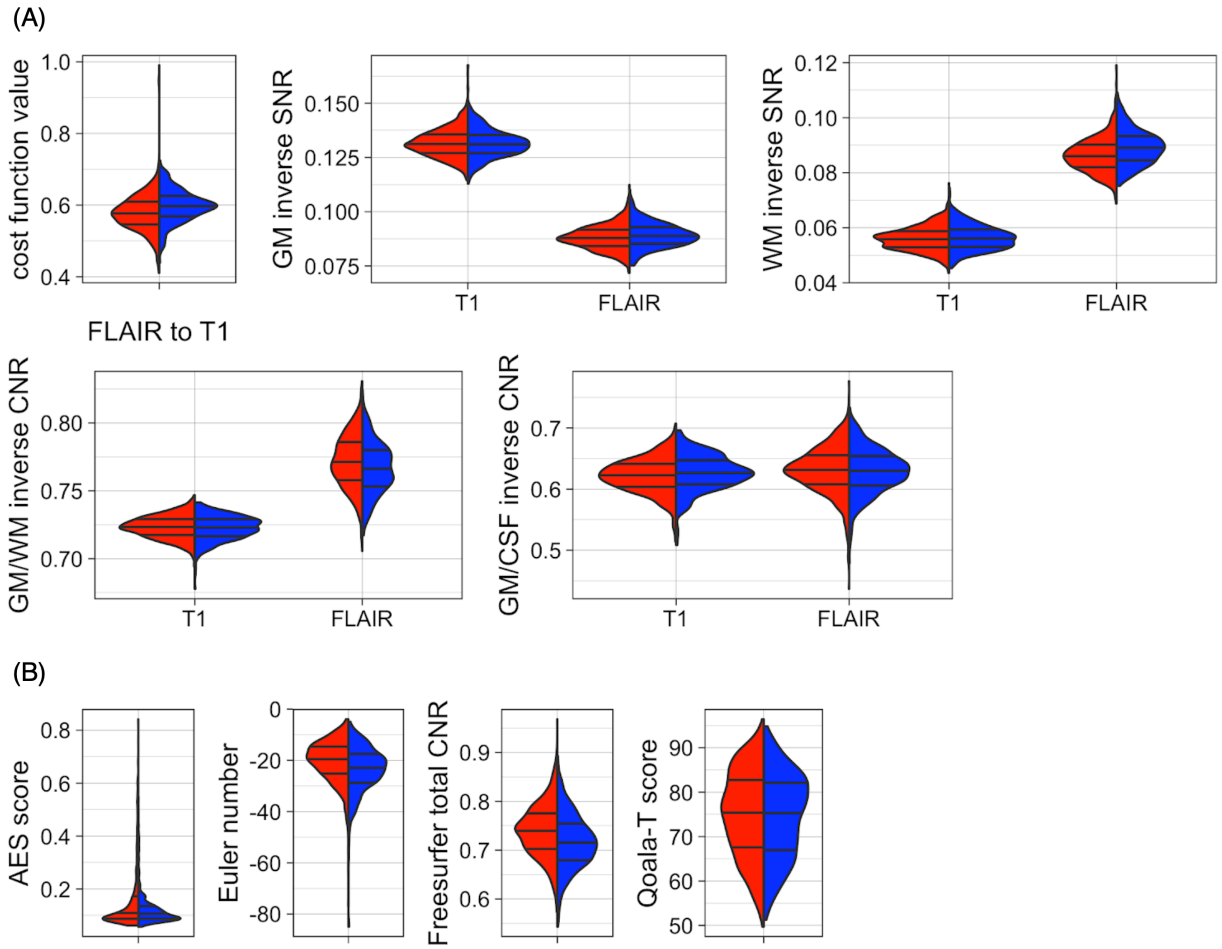

Supplemental Figure 11. Distributions of quantitative QC metrics for structural pipeline.

Distributions of (A) QC IDPs computed in the structural pipeline, and (B) additional IDPs computed outside of our in-house pipeline are presented for male (blue) and female (red) participants. Details of these IDPs are described in the text.

Fieldmap generation processing QC

During the fieldmap generation processing, the following qualitative QC images were produced for each subject:

- Multi-axial plot of B0 brain mask produced by FSL BET overlaid on the mean B0 image to check the quality of brain extraction,
- Multi-axial plot of the mean B0 image coregistered to the native T1 space with the contours of the T1 image to check the quality of B0-to-T1 coregistration.

These images were checked when QC metrics in either DWI or rs-fMRI processing suggested potential problems in the processing of these data, to make sure that they are not caused by the processing error at the fieldmap generation stage.

Diffusion MRI processing QC

During the diffusion processing, we generated both qualitative QC images and quantitative QC metrics for each subject. The qualitative QC images included the following (see Supplemental Figure 12 for examples), which were produced based on the QC metric output of FSL EDDY (Bastiani et al., 2019) and other in-house custom tools inspired by QC described in Tournier et al. (2011) and Roalf et al. (2016):

- Plots of motion root mean square (RMS) from FSL EDDY over the entire volumes, or time points, in DWI data. The RNS describes the displacement of each voxel, and therefore the amount of motion from one volume to the next. Both 'total' and 'restricted' displacement are plotted. The former includes distortion due to eddy current distortion, and the latter estimates the amount of displacement caused by the subject motion.
- Plots of slice-level outliers as well as mean and max outlier 'stdev' and 'sqr_stdev' values over the entire volumes in DWI data, also based on FSL EDDY output. These outliers can be caused by the signal dropout in a specific slice (or group of slices) due to subject motion. The 'stdev' value represents the number of standard deviations off the mean difference between the observed and predicted value computed for each slice. The 'sqr_dev' represents the number of standard deviations off the square root of the mean squared difference between the observation and prediction.
- Plots of voxel-level outliers over the entire volumes in DWI data, based on AFNI 3dToutcount, before and after EC correction and denoising
- Mid-sagittal plots of every volume for each b-value after EC correction and denoising
- Maps and intensity histograms of voxel-level CNR for each non-zero-b-value, produced by FSL EDDY
- Multi-axial maps and intensity histograms of temporal SNR (tSNR) for each b-value
- Multi-axial plot of DTI residual map with a mask of physically implausible voxels overlaid on top. The latter mask represents where the mean intensity level of the b = 0 images is below one or more non-zero-b-value images.

(A) Multi-trace plot

(B) DTI residual map and implausible

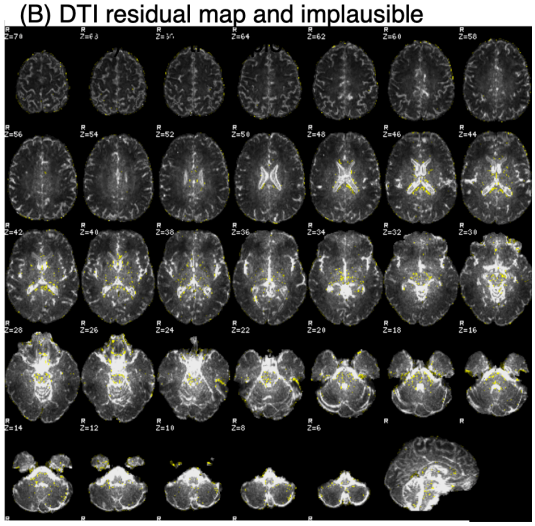

(C) Mid-sagittal plots of each volume of b = 300 image

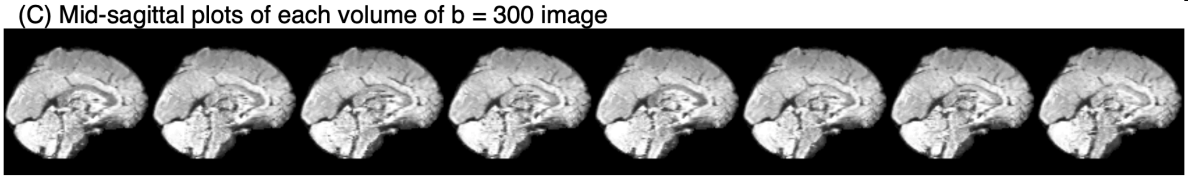

(D) CNR map for b = 300 and image intensity histogram

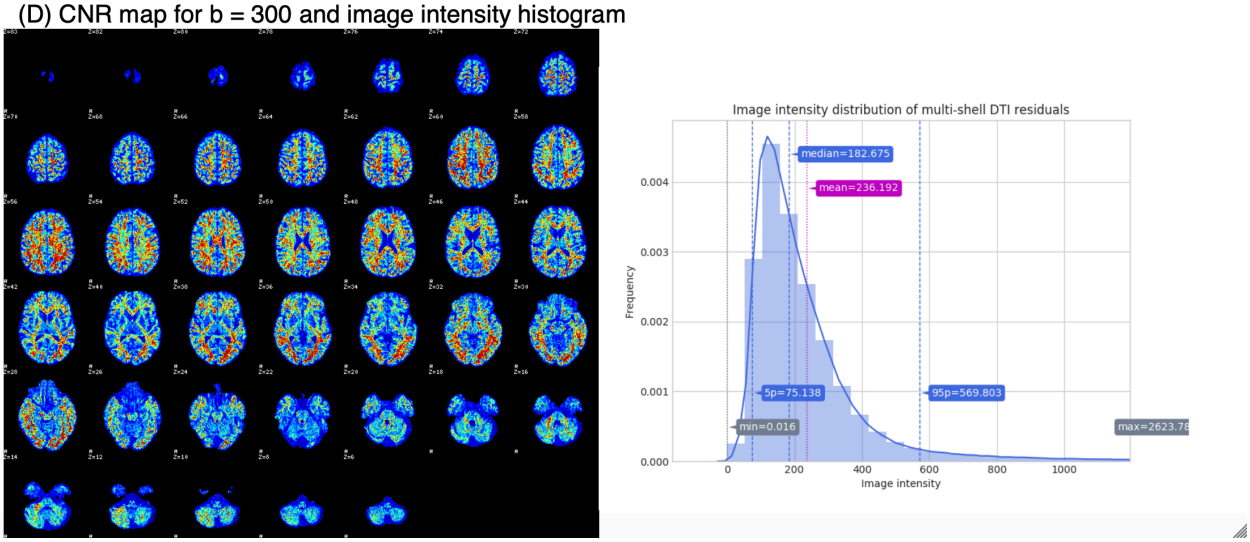

Supplemental Figure 12. Examples of subject-level visual QC images for diffusion pipeline.

(A) Multi-trace plots showing, from the top, 1) 'total' and 'restricted' RMS, 2) number of EDDY outlier slices, 3) mean and max EDDY outlier 'stdev' values, 4) mean and max EDDY outlier 'sqr_stdev' values, and 5) mean fraction of intensity outlier voxels before and after EC correction and denoising. (B) Multi-axial plot of the DTI residual map, with a mask of implausible voxels overlaid on top. (C) Mid-sagittal plots of each volume for each b-value, here showing an example from b = 300 images. (D) Multi-axial plot of CNR and tSNR maps, together with image intensity histograms for these maps, for each non-zero-b-values and b-values for CNR and tSNR, respectively. Here showing the CNR map and histogram for b = 300 as an example.

Rather than reviewing all web pages for each subject, however, we focused on identifying the outliers in any given quantitative QC metrics, then reviewing the web page for those subjects. Although there are increasing interests in the automated QC in DWI (Bastiani et al., 2019; Haddad et al., 2019; Liu et al., 2015, 2010; Oguz et al., 2014; Roalf et al., 2016; Tournier et al., 2011), there has been less consensus with regard to how and when a given data should be removed from the analysis (Liu et al., 2015), compared to the structural or functional data, where some standards have been suggested, albeit somewhat arbitrarily (e.g. Backhausen et al., 2016 for structural data; Power et al., 2015 for rs-fMRI data). As a result, such decisions depend on within- and across-study comparison of any given QC metrics to spot outlier participants or assess the overall quality of the acquired data. The quantitative QC metrics we computed were mainly derived from the same QC outputs used to generate the visual QC images described above, but represent numerical summary of these outputs. Here we present the distributions of these metrics in our dataset to be compared with other studies (Supplemental Figure 13):

- Mean ‘total’ and ‘restricted’ motion RMS
- Mean number of slices classified as outliers per volume during FSL EDDY
- Mean fraction of voxel intensity outliers in each volume after EC correction and denoising, as determined by AFNI 3dToutcount
- Inverse of the mean CNR inside the brain mask for each of the non-zero-b-values, computed using the voxelwise CNR map produced by FSL EDDY
- Inverse of the tSNR inside the brain mask computed for b-value
- Mean residuals inside the brain mask when fitting DTI model
- Fraction of physically implausible voxels inside the brain mask

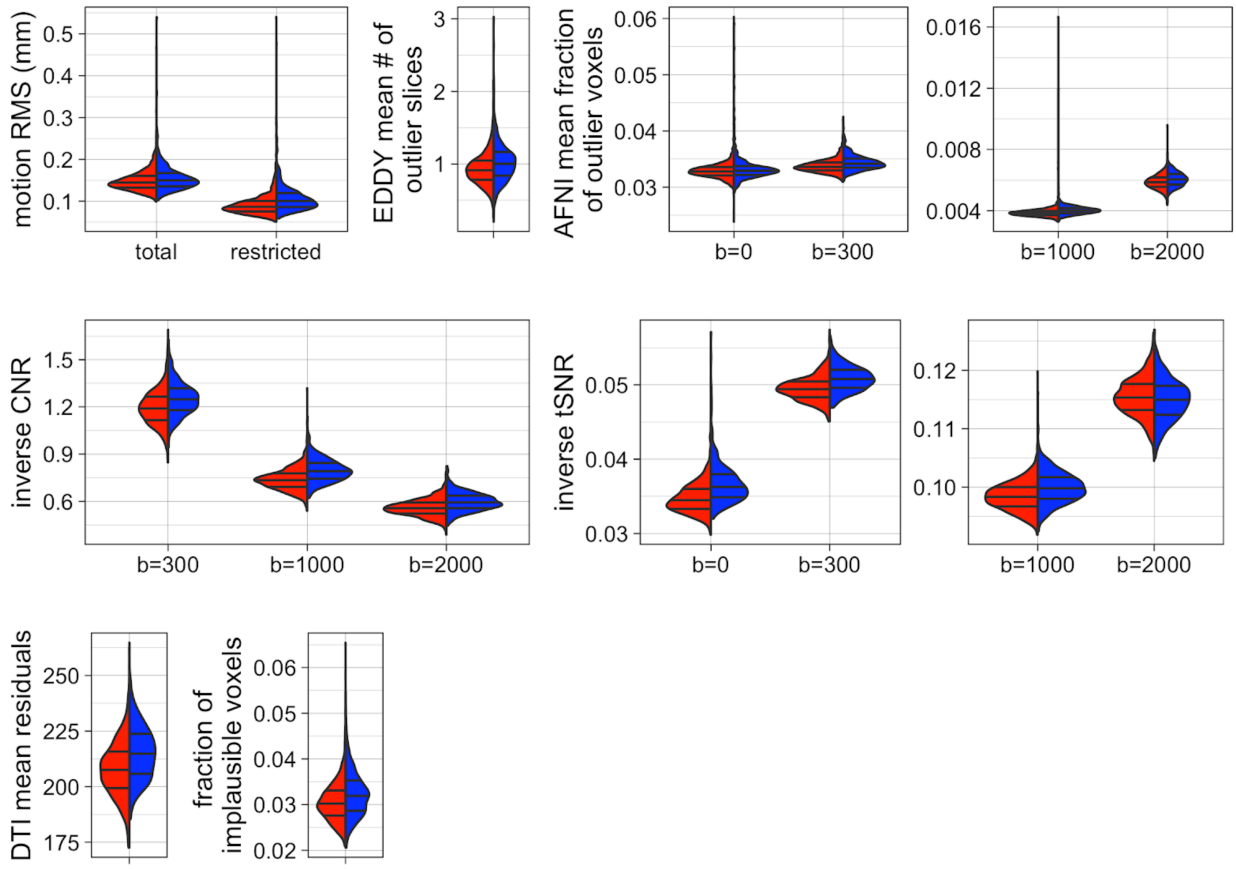

Supplemental Figure 13. Distributions of quantitative QC metrics for diffusion pipeline.

Distributions of QC IDPs from the diffusion pipeline are shown for male (blue) and female (red) participants. See text for details of individual IDPs.

Resting-state fMRI processing QC

As in DWI pipeline, we computed a number of both quantitative QC metrics and qualitative QC images during the pipeline execution. The qualitative QC images included the following (examples shown in Supplemental Figure 14):

- Plots of motion parameters from FSL MCFLIRT and FD over the entire time points of rs-fMRI data
- Plots of global mean signal, as well as mean signals within GM, WM, and ventricles over the entire time points of rs-fMRI data
- Carpet plots of preprocessed rs-fMRI data (Power, 2017) with and without GSR
- Multi-axial plot of the mean rs-fMRI data after motion and distortion correction, with contours of T1 after alignment
- Multi-axial plot of AICHA regional occupancy map, showing the percentage of the functional brain mask within each of the AICHA region in the stereotaxic space
- Similar multi-axial plot of AICHA regional occupancy map, but showing the percentage of GM/WM/ventricles within each AICHA region, using the Freesurfer-based masks in the stereotaxic space.

(A) Multi-trace motion and mean signal plots and carpet plots with and without GSR

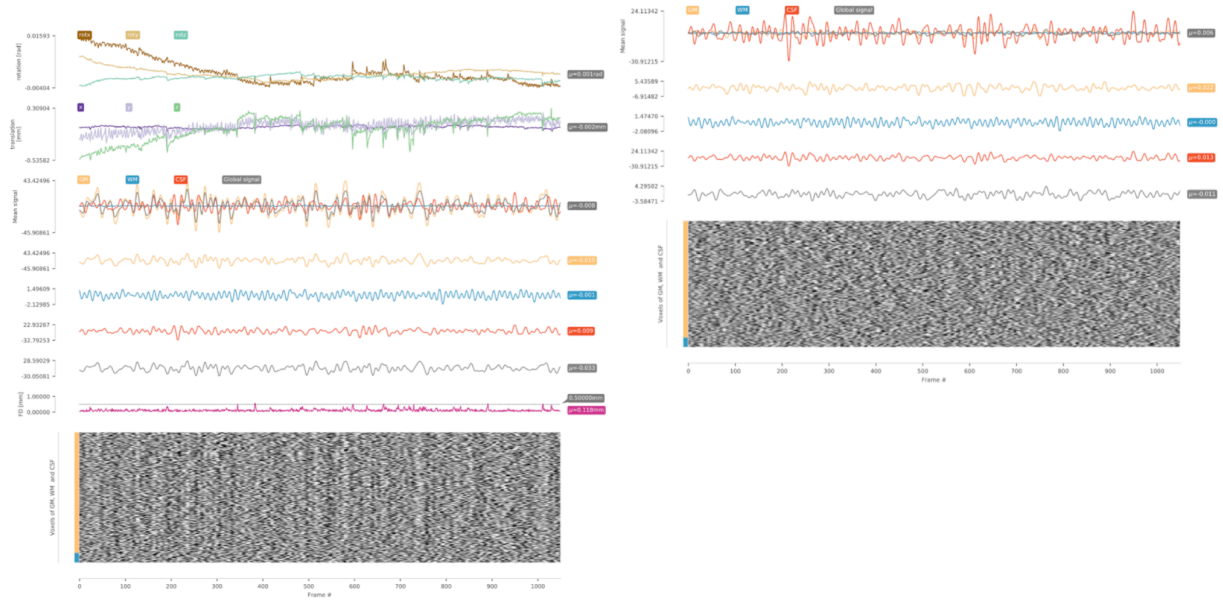

(B) EPI to T1 coregistration contours

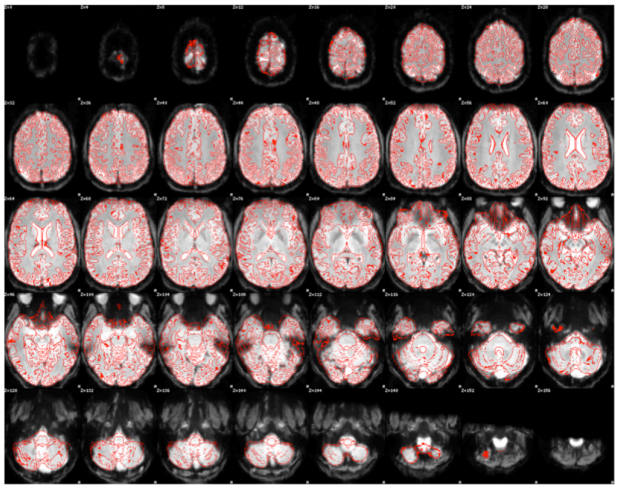

(C) AICHA regional occupancy map

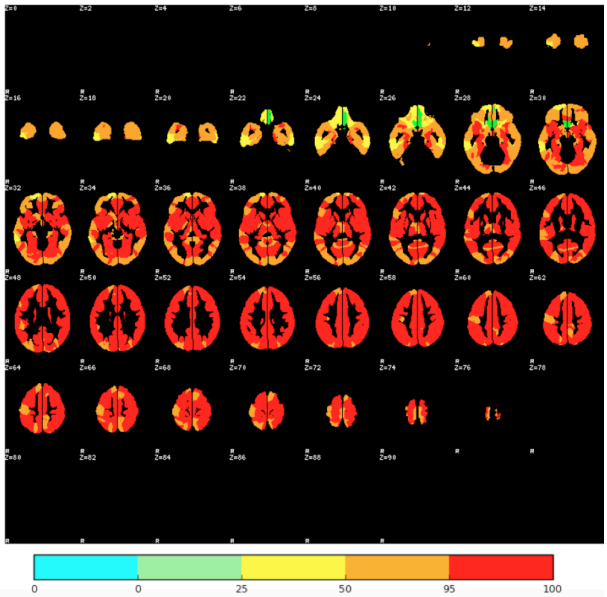

Supplemental Figure 14. Example of subject-level visual QC images for resting-state fMRI pipeline.

(A) Multi-trace plots showing, from the top of the left panel, 1) absolute rotation, 2) absolute translation, 3) global mean signal and signals within GM/WM/ventricles, 4) FD, and 5) carpet plot of the preprocessed (motion- and distortion-corrected, band-passed) rs-fMRI data. The mean signal time courses and the carpet plot in the left and right panel were derived from data without and with GSR, respectively. (B) Multi-axial plot of the average pre-processed data aligned to T1, together with the contour of the reference T1 image. (C) Multi-axial plot of AICHA regional occupancy map, showing the percentage of the functional brain mask within each AICHA region. Similar AICHA occupancy maps were created that show the percentages of GM/WM/ventricles within each AICHA region.

Also as in DWI pipeline, we focused on identifying the outliers in the quantitative QC metrics and checking their visual QC web pages rather than reviewing every single subject-level QC page. However, we note that any excessive motion was censured through 'scrubbing' described above when computing IC matrices. Also, some subjects were excluded on a regional basis when computing the average regions IC matrices. Here we present the distributions of the following quantitative QC metrics (Supplemental Figure 15) to be compared with other studies:

- Cost function values for EPI to T1 after the BBR alignment to T1, as well as after BBR + FLIRT alignment to T1
- Mean relative RMS displacement, as well as mean and max absolute translation and rotation (mean over each x, y, and z directions), over the entire time course of the rs-fMRI data estimated by MCFLIRT
- Inverse tSNR before and after band-pass filtering that also included despiking and nuisance regressor removal
- Mean FD (Power et al., 2012) and the proportion of volumes above FD above 0.2 and 0.5 (Power et al., 2015) over the entire time course of the rs-fMRI data

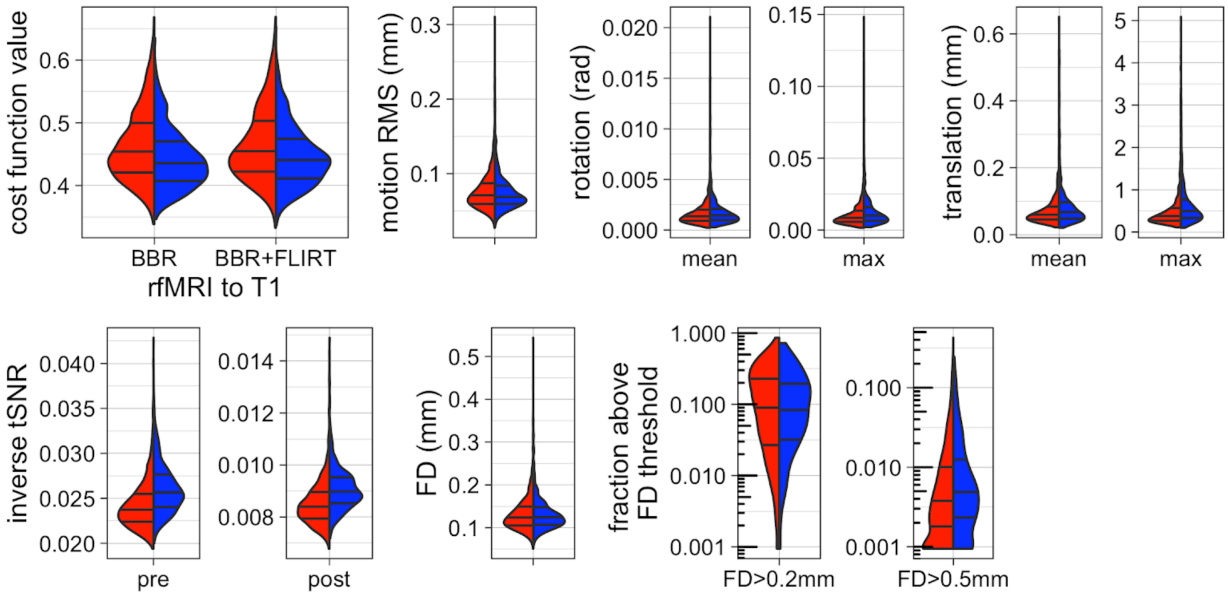

Supplemental Figure 15. Distributions of quantitative QC metrics for resting-state fMRI pipeline.

Distributions of QC IDPs from the rs-fMRI pipeline are shown for male (blue) and female (red) participants. See text for details of individual IDPs. Note that log-scale is used for the fraction of rs-fMRI volumes above the given FD threshold, since the distributions for both thresholds are highly skewed

Additional statistical analyses

Sample distribution of some global IDP's

Supplemental Figure 16 shows the distributions of global IDPs presented in the current paper, namely mean CT, total inner and pial CSA, and total GM and WM volumes (Supplemental Figure 16A) from the structural pipeline, and mean values of four DTI metrics (FA, MD, AD, and RD) and three NODDI metrics (NDI, ODI, and IsoVF) within the cerebral WM (Supplemental Figure 16B).

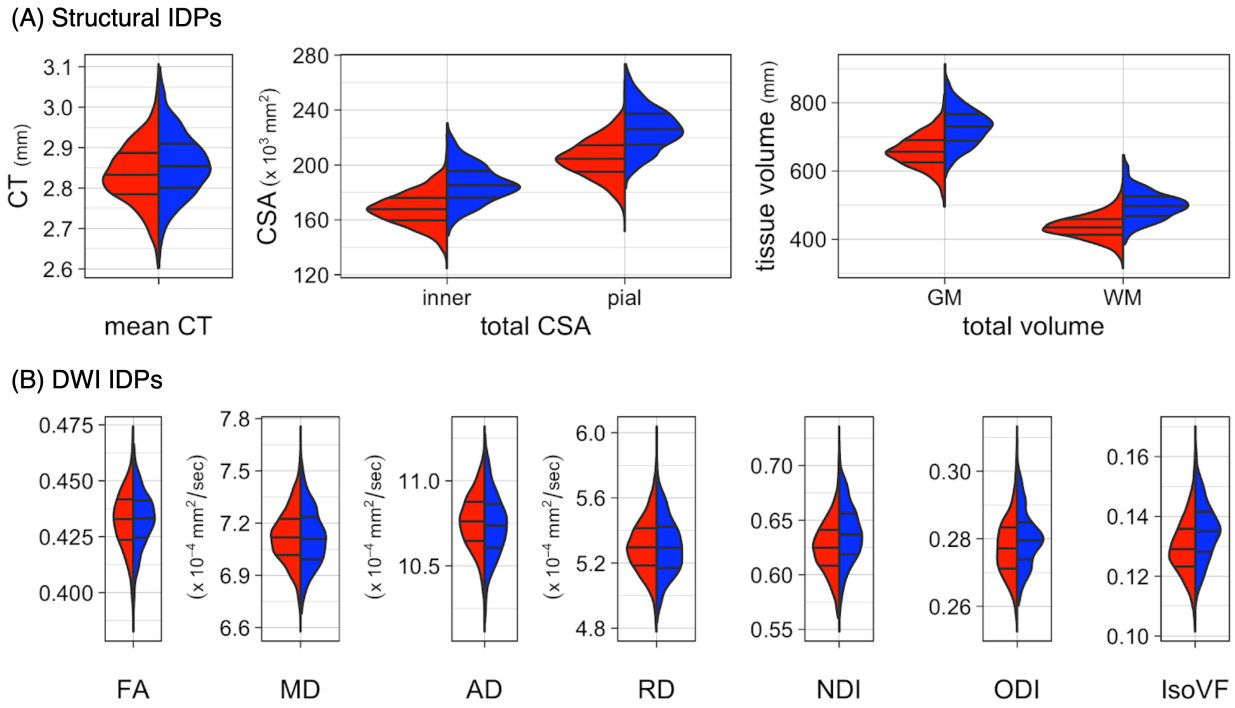

Supplemental Figure 16. Distributions of global IDPs from the structural and diffusion pipelines.

Distributions of (A) five IDPs produced by the structural pipeline and (B) seven IDPs from the diffusion pipeline are presented for male (blue) and female (red) participants.

Correlation of total inner and pial CSA

While most studies report the inner CSA defined by GM/WM interface, and this is the default cortical areal measure in Freesurfer, it is possible to compute the pial CSA defined by GM/CSF interface. Not surprisingly, the total inner and pial CSA were highly correlated in our data, with pial CSA being larger than inner CSA. Supplemental Figure 17 shows the relationship between the two variables in 1,722 subjects of the MRi-Share data.

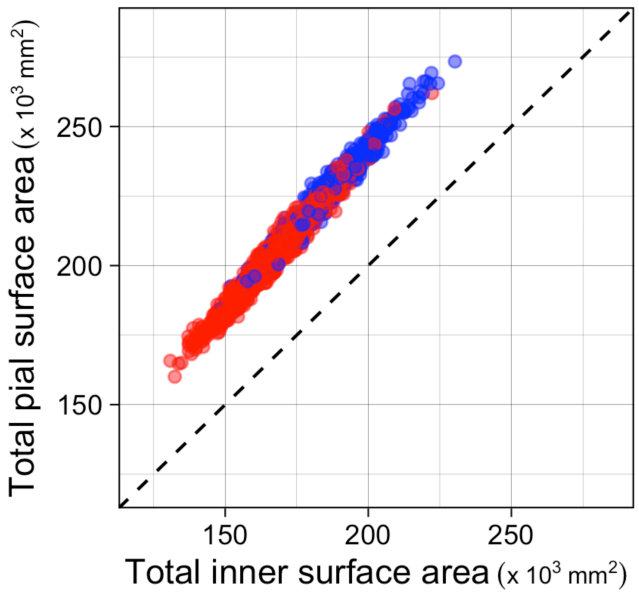

Supplemental Figure 17. The relationship between CSA and CSA pial in 1,722 subjects. The plot shows the total inner and pial CSA for each subject, represented as a dot in the scatter plot. The color represents the sex of the subject (blue for males and red for females).

The interaction of eTIV and sex in WM volume data

The combined sex analysis showed the significant interaction between eTIV and sex (p = 0.0004), indicating that the slope for males is steeper than females. Supplemental Figure 18 shows the small difference in the slopes of the WM volume-to-eTIV in males and females.

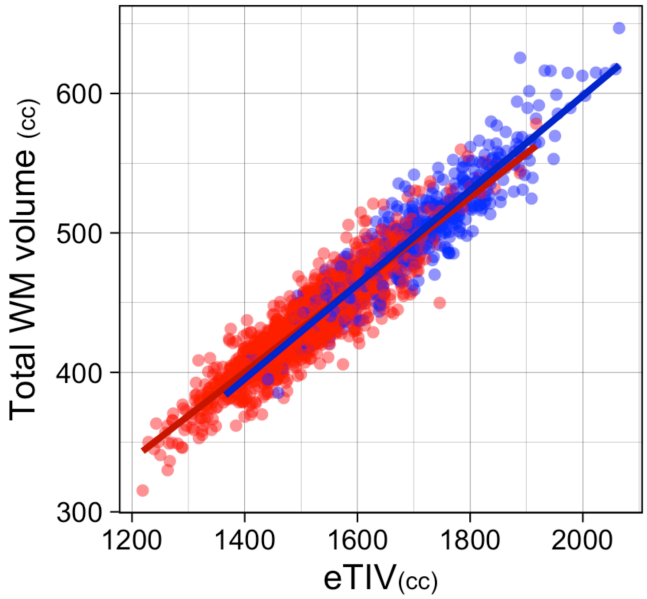

Supplemental Figure 18. The interaction of eTIV and sex in WM volume data.

The plot shows the relationship between total WM volume and eTIV in both sexes. Males show slightly steeper slope than for females.

Fit results of alternative models in the global GM, WM morphometry and WM property analyses

In the main manuscript, we primarily reported the results of linear age effect models with or without eTIV (or WM mask volume in the case of WM properties) that best describe the data according to BIC. However, here we report the results the alternative model fit results to assess how the inclusion or non-inclusion of global volume effects in the model affects the observed age or sex effects, and to allow comparison with any prior studies that did or did not control for such global volume effects.

Global gray matter morphometry

The BIC indicated that inclusion of eTIV did not improve overall fit for modeling CT, while it did for inner CSA, pial CSA, and GM volume data. Here we report the model fit results with eTIV for CT, and without eTIV for inner CSA, pial CSA, and GM in Supplemental Table 1. The estimates of age or sex effects are not much affected by the inclusion of eTIV. In contrast, excluding eTIV slightly reduces the estimates of age-related variance for both inner and pial CSA, and GM, decreasing the level of significance for the age effects in these metrics, although the estimated slope for the age tends to increase, in particular for inner and pial CSA data in males. Not surprisingly, the exclusion of eTIV also significantly impacts the observed sex effects on these metrics, as males generally have larger total eTIV and, as a result, larger raw values for inner and pial CSA as well as GM, than females. These absolute differences in the sexes disappear and in some cases reverse the effects when eTIV is accounted for in the model.

Supplemental Table 1. The effects of inclusion or exclusion of eTIV on the age and sex effects on global GM morphometry.

The results of alternative linear model fit for mean CT, total inner CSA, and total pial CSA from Freesurfer v6.0, as well as total GM volume from SPM12, are shown. Parameter estimates (β) for age and sex are shown, together with 95% confidence intervals (CI) for each β, as well as uncorrected p values and partial eta squared as the effect sizes for each variable. The Model column indicates the alternative model (see text) with the corresponding model number as described in Methods section. The interaction between sex and age was tested in the combined group but was not significant in any of the metrics listed here, and thus is not included in the table. Overall model fit is indicated as adjusted squared R values.

			Age			Sex (M>F)			
	N	**Model**	β	*p*	partial η^2	β	*p*	partial η^2	**adj R^2**
CT			($x10^{-3}$ mm/yr)			($x10^{-3}$ mm)			
Male	470	(2)	-2.47 [-6.46, 1.53]	0.23	0.003	--		--	-0.001
Female	1252	(2)	-4.56 [-6.95, -2.18]	$1.8x10^{-4}$	0.011	--		--	-0.001
Combined	1722	(4)	-3.52 [-5.76, -1.27]	0.0022	0.008	21.8 [10.1, 33.5]	$<2.0x10^{-16}$	0.009	0.024
inner CSA			($x10^2$ mm²/yr)			($x10^2$ mm²)			
Male	470	(1)	-7.51 [-14.3, -0.68]	0.031	0.010	--		--	0.008
Female	1252	(1)	-2.26 [-6.20, 1.67]	0.26	0.001	--		--	0.000
Combined	1722	(3)	-4.89 [-8.63, -1.14]	0.011	0.003	180.4 [166.8, 193.9]	$<2.0x10^{-16}$	0.284	0.028
pial CSA			($x10^2$ mm²/yr)			($x10^2$ mm²)			
Male	470	(1)	-11.3 [-19.1, -3.44]	0.0049	0.017	--		--	0.015
Female	1252	(1)	-5.06 [-9.66, -0.47]	0.031	0.004	--		--	0.003
Combined	1722	(3)	-3.10 [-12.5, -3.81]	$2.4x10^{-4}$	0.007	217.7 [202.0, 233.3]	$<2.0x10^{-16}$	0.301	0.301
GM			(cc/yr)			(cc)			
Male	470	(1)	-3.47 [-6.17, -0.78]	0.012	0.014	--		--	0.011
Female	1252	(1)	-2.63 [-4.19, -1.07]	$9.9x10^{-4}$	0.009	--		--	0.008
Combined	1722	(3)	-3.05 [-4.54, -1.57]	$5.8x10^{-5}$	0.01	72.2 [66.8, 77.5]	$<2.0x10^{-16}$	0.010	0.291

Global white matter morphometry and properties

Like GM, the total WM volume was also significantly affected by eTIV. For the mean DTI metrics within the cerebral WM mask, BIC indicated that the inclusion of mask volume in the model improved the model sufficiently for MD and AD in male, but not in female, data. Here we report the alternative model results in Supplemental Table 2.

Supplemental Table 2. The effects of inclusion or exclusion of eTIV or the WM mask volume on the age and sex effects on WM volume and DTI data.

The results of alternative linear model fit for total white matter volume (WM) from SPM12, as well as mean DTI metrics within subject-specific cerebral WM masks are shown. Parameter estimates (β) for age and sex are shown, together with 95% confidence intervals (CI) for each β, as well as uncorrected p values and partial eta squared as the effect sizes for each variable. The Model column indicates the alternative model (see text), with the corresponding model number as described in Methods section. The interaction between sex and age was tested in the combined group but was not significant in any of the metrics listed here, and thus is not included in the table. Overall model fit is indicated as adjusted squared R values.

			Age			Sex (M>F)			
	N	**Model**	β	*p*	partial η^2	β	*p*	partial η^2	**adj R^2**
CT			(x10^{-3} mm/yr)			(x10^{-3} mm)			
Male	470	(2)	-2.47 [-6.46, 1.53]	0.23	0.003	--		--	-0.001
Female	1252	(2)	-4.56 [-6.95, -2.18]	1.8x10^{-4}	0.011	--		--	-0.001
Combined	1722	(4)	-3.52 [-5.76, -1.27]	0.0022	0.008	21.8 [10.1, 33.5]	<2.0x10^{-16}	0.009	0.024
inner CSA			(x10² mm²/yr)			(x10² mm²)			
Male	470	(1)	-7.51 [-14.3, -0.68]	0.031	0.010	--		--	0.008
Female	1252	(1)	-2.26 [-6.20, 1.67]	0.26	0.001	--		--	0.000
Combined	1722	(3)	-4.89 [-8.63, -1.14]	0.011	0.003	180.4 [166.8, 193.9]	<2.0x10^{-16}	0.284	0.028
pial CSA			(x10² mm²/yr)			(x10² mm²)			
Male	470	(1)	-11.3 [-19.1, -3.44]	0.0049	0.017	--		--	0.015
Female	1252	(1)	-5.06 [-9.66, -0.47]	0.031	0.004	--		--	0.003
Combined	1722	(3)	-3.10 [-12.5, -3.81]	2.4x10^{-4}	0.007	217.7 [202.0, 233.3]	<2.0x10^{-16}	0.301	0.301
GM			(cc/yr)			(cc)			
Male	470	(1)	-3.47 [-6.17, -0.78]	0.012	0.014	--		--	0.011
Female	1252	(1)	-2.63 [-4.19, -1.07]	9.9x10^{-4}	0.009	--		--	0.008
Combined	1722	(3)	-3.05 [-4.54, -1.57]	5.8x10^{-5}	0.01	72.2 [66.8, 77.5]	<2.0x10^{-16}	0.010	0.291

When not taking eTIV into account, the total WM volume no longer showed any significant positive age-related variations, and the age-related variance in the data was much reduced. As in GM, it also affected the observed sex effects, indicating a significantly larger raw WM values in males than in females, which disappears once eTIV is taken into account.

Inclusion or exclusion of the WM mask volume did not impact the estimates of age effects in any of the mean DTI metrics. It did slightly affect the observed sex effects in the diffusivity measures, with a tendency for higher diffusivity in females than in males when controlling for the mask volume but no difference when not controlling for the volume.

For the mean NODDI metrics, BIC indicated the inclusion of WM mask volume in the model to improve the fit for IsoVF only, and not for NDI or ODI. The Supplemental Table 3 reports the alternative model results, showing the results with the mask volume in the model for NDI and ODI, and without the mask volume for IsoVF. The inclusion or exclusion of the mask volume did not noticeably affect either age or sex effects in any of the NODDI metrics, although the sex difference in the mean IsoVF (higher in males than in females) seems to be attenuated slightly when not taking into account the mask volume.

Supplemental Table 3. The effects of inclusion or exclusion of the WM mask volume on the age and sex effects on NODDI data.

The results of alternative linear model fit for mean NODDI metrics within subject-specific cerebral WM masks are shown. Parameter estimates (β) for age and sex are shown, together with 95% confidence intervals (CI) for each β, as well as uncorrected p values and partial eta squared as the effect sizes for each variable. The Model column indicates the alternative model (see text) with the corresponding model number as described in Methods section. The interaction between sex and age was tested in the combined group but was not significant in any of the metrics listed here, and thus is not included in the table. Overall model fit is indicated as adjusted squared R values.

			Age			Sex (M>F)			
	N	**Model**	β [95% CI]	*p*	partial η^2	β [95% CI]	*p*	partial η^2	**adj R^2**
NDI			($x10^{-3}$ /yr)			($x10^{-3}$)			
Male	468	(2)	3.65 [2.37, 4.94]	$4.1x10^{-8}$	0.063	--	--	--	0.060
Female	1246	(2)	2.51 [1.74, 3.27]	$1.7x10^{-10}$	0.032	--	--	--	0.034
Combined	1714	(4)	3.08 [2.36, 3.80]	$<2.0x10^{-16}$	0.041	11.0 [6.95, 13.7]	$2.5x10^{-9}$	0.023	0.083
ODI			($x10^{-4}$/yr)			($x10^{-4}$)			
Male	468	(2)	6.69 [2.61, 10.8]	0.0014	0.022	--	--	--	0.018
Female	1246	(2)	6.45 [3.66, 9.25]	$6.5x10^{-6}$	0.016	--	--	--	0.015
Combined	1714	(4)	6.57 [4.04, 9.10]	$4.0x10^{-7}$	0.018	22.1 [10.2, 34.0]	$2.7x10^{-4}$	0.009	0.026
IsoVF			($x10^{-4}$/yr)			($x10^{-4}$)			
Male	468	(1)	3.16 [-1.76, 8.08]	0.21	0.003	--	--	--	0.001
Female	1246	(1)	3.65 [0.66, 6.64]	0.017	0.005	--	--	--	0.004
Combined	1714	(3)	3.41 [0.61, 6.21]	0.017	0.004	55.6 [45.4, 65.7]	$<2.0x10^{-16}$	0.064	0.067

References

Alfaro-Almagro, F., Jenkinson, M., Bangerter, N.K., Andersson, J.L.R., Griffanti, L., Douaud, G., Sotiropoulos, S.N., Jbabdi, S., Hernandez-Fernandez, M., Vallee, E., Vidaurre, D., Webster, M., McCarthy, P., Rorden, C., Daducci, A., Alexander, D.C., Zhang, H., Dragonu, I., Matthews, P.M., Miller, K.L., Smith, S.M., 2018. Image processing and Quality Control for the first 10,000 brain imaging datasets from UK Biobank. Neuroimage 166, 400–424. doi:10.1016/j.neuroimage.2017.10.034

Andersson, J.L.R., Graham, M.S., Zsoldos, E., Sotiropoulos, S.N., 2016. Incorporating outlier detection and replacement into a non-parametric framework for movement and distortion correction of diffusion MR images. Neuroimage 141, 556–572. doi:10.1016/j.neuroimage.2016.06.058

Andersson, J.L.R., Skare, S., Ashburner, J., 2003. How to correct susceptibility distortions in spin-echo echo-planar images: application to diffusion tensor imaging. Neuroimage 20, 870–888. doi:10.1016/S1053-8119(03)00336-7

Andersson, J.L.R., Sotiropoulos, S.N., 2016. An integrated approach to correction for off-resonance effects and subject movement in diffusion MR imaging. Neuroimage 125, 1063–1078. doi:10.1016/j.neuroimage.2015.10.019

Ashburner, J., Barnes, G., Chen, C.-C., Daunizeau, J., Flandin, G., Friston, K., Kiebel, S., Kilner, J., Litvak, V., Moran, R., Penny, W., Razi, A., Stephan, K., Tak, S., Zeidman, P., Gitelman, D., Henson, R., Hutton, C., Glauche, V., Mattout, J., Phillips, C., 2014. SPM12 Manual.

Ashburner, J., Friston, K.J., 2005. Unified segmentation. Neuroimage 26, 839–851. doi:10.1016/j.neuroimage.2005.02.018

Avants, B.B., Epstein, C.L., Grossman, M., Gee, J.C., 2008. Symmetric diffeomorphic image registration with cross-correlation: evaluating automated labeling of elderly and neurodegenerative brain. Med. Image Anal. 12, 26–41. doi:10.1016/j.media.2007.06.004

Backhausen, L.L., Herting, M.M., Buse, J., Roessner, V., Smolka, M.N., Vetter, N.C., 2016. Quality Control of Structural MRI Images Applied Using FreeSurfer-A Hands-On Workflow to Rate Motion Artifacts. Front. Neurosci. 10, 558. doi:10.3389/fnins.2016.00558

Basser, P.J., Mattiello, J., LeBihan, D., 1994. MR diffusion tensor spectroscopy and imaging. Biophys. J. 66, 259–267. doi:10.1016/S0006-3495(94)80775-1

Bastiani, M., Cottaar, M., Fitzgibbon, S.P., Suri, S., Alfaro-Almagro, F., Sotiropoulos, S.N., Jbabdi, S., Andersson, J.L.R., 2019. Automated quality control for within and between studies diffusion MRI data using a non-parametric framework for movement and distortion correction. Neuroimage 184, 801–812. doi:10.1016/j.neuroimage.2018.09.073

Baykara, E., Gesierich, B., Adam, R., Tuladhar, A.M., Biesbroek, J.M., Koek, H.L., Ropele, S., Jouvent, E., Alzheimer's Disease Neuroimaging Initiative, Chabriat, H., Ertl-Wagner, B., Ewers, M., Schmidt, R., de Leeuw, F.-E., Biessels, G.J., Dichgans, M., Duering, M., 2016. A novel imaging marker for small vessel disease based on skeletonization of white matter tracts and diffusion histograms. Ann. Neurol. 80, 581–592. doi:10.1002/ana.24758

Beaudet, G., Tsuchida, A., Petit, L., Tzourio, C., Caspers, S., Schreiber, J., Pausova, Z., Patel, Y., Paus, T., Schmidt, R., Pirpamer, L., Sachdev, P.S., Brodaty, H., Kochan, N., Trollor, J., Wen, W., Armstrong, N.J., Deary, I.J., Bastin, M.E., Wardlaw, J.M., Mazoyer, B., 2020. Age-Related Changes of Peak Width Skeletonized Mean Diffusivity (PSMD) Across the Adult Lifespan: A Multi-Cohort Study. Front. Psychiatry 11, 342. doi:10.3389/fpsyt.2020.00342

Beckmann, C.F., Smith, S.M., 2004. Probabilistic independent component analysis for functional magnetic resonance imaging. IEEE Trans. Med. Imaging 23, 137–152. doi:10.1109/TMI.2003.822821

Choi, S., Kim, T., Yu, W., 2009. Performance evaluation of RANSAC family, in: Procedings of the British Machine Vision Conference 2009. Presented at the British Machine Vision

Conference 2009, British Machine Vision Association, pp. 81.1-81.12. doi:10.5244/C.23.81
Coupe, P., Manjon, J., Robles, M., Collins, L.D., 2011. Adaptive Multiresolution Non-Local Means Filter for 3D MR Image Denoising. IET Image Processing.
Coupe, P., Yger, P., Prima, S., Hellier, P., Kervrann, C., Barillot, C., 2008. An optimized blockwise nonlocal means denoising filter for 3-D magnetic resonance images. IEEE Trans. Med. Imaging 27, 425–441. doi:10.1109/TMI.2007.906087
Daducci, A., Canales-Rodríguez, E.J., Zhang, H., Dyrby, T.B., Alexander, D.C., Thiran, J.-P., 2015. Accelerated Microstructure Imaging via Convex Optimization (AMICO) from diffusion MRI data. Neuroimage 105, 32–44. doi:10.1016/j.neuroimage.2014.10.026
Dale, A.M., Fischl, B., Sereno, M.I., 1999. Cortical surface-based analysis. I. Segmentation and surface reconstruction. Neuroimage 9, 179–194. doi:10.1006/nimg.1998.0395
Desikan, R.S., Ségonne, F., Fischl, B., Quinn, B.T., Dickerson, B.C., Blacker, D., Buckner, R.L., Dale, A.M., Maguire, R.P., Hyman, B.T., Albert, M.S., Killiany, R.J., 2006. An automated labeling system for subdividing the human cerebral cortex on MRI scans into gyral based regions of interest. Neuroimage 31, 968–980. doi:10.1016/j.neuroimage.2006.01.021
Diedrichsen, J., Balsters, J.H., Flavell, J., Cussans, E., Ramnani, N., 2009. A probabilistic MR atlas of the human cerebellum. Neuroimage 46, 39–46. doi:10.1016/j.neuroimage.2009.01.045
Fischl, B., Salat, D.H., Busa, E., Albert, M., Dieterich, M., Haselgrove, C., van der Kouwe, A., Killiany, R., Kennedy, D., Klaveness, S., Montillo, A., Makris, N., Rosen, B., Dale, A.M., 2002. Whole Brain Segmentation. Neuron 33, 341–355. doi:10.1016/S0896-6273(02)00569-X
Fischl, B., Salat, D.H., van der Kouwe, A.J.W., Makris, N., Ségonne, F., Quinn, B.T., Dale, A.M., 2004. Sequence-independent segmentation of magnetic resonance images. Neuroimage 23 Suppl 1, S69-84. doi:10.1016/j.neuroimage.2004.07.016
Frazier, J.A., Chiu, S., Breeze, J.L., Makris, N., Lange, N., Kennedy, D.N., Herbert, M.R., Bent, E.K., Koneru, V.K., Dieterich, M.E., Hodge, S.M., Rauch, S.L., Grant, P.E., Cohen, B.M., Seidman, L.J., Caviness, V.S., Biederman, J., 2005. Structural brain magnetic resonance imaging of limbic and thalamic volumes in pediatric bipolar disorder. Am. J. Psychiatry 162, 1256–1265. doi:10.1176/appi.ajp.162.7.1256
Friston, K.J., Williams, S., Howard, R., Frackowiak, R.S., Turner, R., 1996. Movement-related effects in fMRI time-series. Magn. Reson. Med. 35, 346–355. doi:10.1002/mrm.1910350312
Ganzetti, M., Wenderoth, N., Mantini, D., 2016a. Quantitative evaluation of intensity inhomogeneity correction methods for structural MR brain images. Neuroinformatics 14, 5–21. doi:10.1007/s12021-015-9277-2
Ganzetti, M., Wenderoth, N., Mantini, D., 2016b. Intensity Inhomogeneity Correction of Structural MR Images: A Data-Driven Approach to Define Input Algorithm Parameters. Front. Neuroinformatics 10, 10. doi:10.3389/fninf.2016.00010
Garyfallidis, E., Brett, M., Amirbekian, B., Rokem, A., van der Walt, S., Descoteaux, M., Nimmo-Smith, I., Dipy Contributors, 2014. Dipy, a library for the analysis of diffusion MRI data. Front. Neuroinformatics 8, 8. doi:10.3389/fninf.2014.00008
Goldstein, J.M., Seidman, L.J., Makris, N., Ahern, T., O'Brien, L.M., Caviness, V.S., Kennedy, D.N., Faraone, S.V., Tsuang, M.T., 2007. Hypothalamic abnormalities in schizophrenia: sex

effects and genetic vulnerability. Biol. Psychiatry 61, 935–945. doi:10.1016/j.biopsych.2006.06.027

Haddad, S.M.H., Scott, C.J.M., Ozzoude, M., Holmes, M.F., Arnott, S.R., Nanayakkara, N.D., Ramirez, J., Black, S.E., Dowlatshahi, D., Strother, S.C., Swartz, R.H., Symons, S., Montero-Odasso, M., ONDRI Investigators, Bartha, R., 2019. Comparison of quality control methods for automated diffusion tensor imaging analysis pipelines. PLoS ONE 14, e0226715. doi:10.1371/journal.pone.0226715

Iglesias, J.E., Augustinack, J.C., Nguyen, K., Player, C.M., Player, A., Wright, M., Roy, N., Frosch, M.P., McKee, A.C., Wald, L.L., Fischl, B., Van Leemput, K., Alzheimer's Disease Neuroimaging Initiative, 2015a. A computational atlas of the hippocampal formation using ex vivo, ultra-high resolution MRI: Application to adaptive segmentation of in vivo MRI. Neuroimage 115, 117–137. doi:10.1016/j.neuroimage.2015.04.042

Iglesias, J.E., Van Leemput, K., Bhatt, P., Casillas, C., Dutt, S., Schuff, N., Truran-Sacrey, D., Boxer, A., Fischl, B., Alzheimer's Disease Neuroimaging Initiative, 2015b. Bayesian segmentation of brainstem structures in MRI. Neuroimage 113, 184–195. doi:10.1016/j.neuroimage.2015.02.065

Jenkinson, M., Bannister, P., Brady, M., Smith, S., 2002. Improved optimization for the robust and accurate linear registration and motion correction of brain images. Neuroimage 17, 825–841. doi:10.1016/s1053-8119(02)91132-8

Jenkinson, M., Smith, S., 2001. A global optimisation method for robust affine registration of brain images. Med. Image Anal. 5, 143–156. doi:10.1016/s1361-8415(01)00036-6

Jensen, J.H., Helpern, J.A., 2010. MRI quantification of non-Gaussian water diffusion by kurtosis analysis. NMR Biomed. 23, 698–710. doi:10.1002/nbm.1518

Joliot, M., Jobard, G., Naveau, M., Delcroix, N., Petit, L., Zago, L., Crivello, F., Mellet, E., Mazoyer, B., Tzourio-Mazoyer, N., 2015. AICHA: An atlas of intrinsic connectivity of homotopic areas. J. Neurosci. Methods 254, 46–59. doi:10.1016/j.jneumeth.2015.07.013

Klapwijk, E.T., van de Kamp, F., van der Meulen, M., Peters, S., Wierenga, L.M., 2019. Qoala-T: A supervised-learning tool for quality control of FreeSurfer segmented MRI data. Neuroimage 189, 116–129. doi:10.1016/j.neuroimage.2019.01.014

Lindig, T., Kotikalapudi, R., Schweikardt, D., Martin, P., Bender, F., Klose, U., Ernemann, U., Focke, N.K., Bender, B., 2018. Evaluation of multimodal segmentation based on 3D T1-, T2- and FLAIR-weighted images - the difficulty of choosing. Neuroimage 170, 210–221. doi:10.1016/j.neuroimage.2017.02.016

Liu, B., Zhu, T., Zhong, J., 2015. Comparison of quality control software tools for diffusion tensor imaging. Magn. Reson. Imaging 33, 276–285. doi:10.1016/j.mri.2014.10.011

Liu, Z., Wang, Y., Gerig, G., Gouttard, S., Tao, R., Fletcher, T., Styner, M., 2010. Quality control of diffusion weighted images. Proc. SPIE 7628. doi:10.1117/12.844748

Madan, C.R., 2018. Age differences in head motion and estimates of cortical morphology. PeerJ 6, e5176. doi:10.7717/peerj.5176

Makris, N., Goldstein, J.M., Kennedy, D., Hodge, S.M., Caviness, V.S., Faraone, S.V., Tsuang, M.T., Seidman, L.J., 2006. Decreased volume of left and total anterior insular lobule in schizophrenia. Schizophr. Res. 83, 155–171. doi:10.1016/j.schres.2005.11.020

Minka, T., 2000. Automatic choice of dimensionality for PCA. (Technical Report No. 514). MIT Media Lab Vision and Modeling Group.

Mori, S., Oishi, K., Jiang, H., Jiang, L., Li, X., Akhter, K., Hua, K., Faria, A.V., Mahmood, A., Woods, R., Toga, A.W., Pike, G.B., Neto, P.R., Evans, A., Zhang, J., Huang, H., Miller, M.I., van Zijl, P., Mazziotta, J., 2008. Stereotaxic white matter atlas based on diffusion tensor imaging in an ICBM template. Neuroimage 40, 570–582. doi:10.1016/j.neuroimage.2007.12.035

Oguz, I., Farzinfar, M., Matsui, J., Budin, F., Liu, Z., Gerig, G., Johnson, H.J., Styner, M., 2014. DTIPrep: quality control of diffusion-weighted images. Front. Neuroinformatics 8, 4. doi:10.3389/fninf.2014.00004

Oishi, K., Zilles, K., Amunts, K., Faria, A., Jiang, H., Li, X., Akhter, K., Hua, K., Woods, R., Toga, A.W., Pike, G.B., Rosa-Neto, P., Evans, A., Zhang, J., Huang, H., Miller, M.I., van Zijl, P.C.M., Mazziotta, J., Mori, S., 2008. Human brain white matter atlas: identification and assignment of common anatomical structures in superficial white matter. Neuroimage 43, 447–457. doi:10.1016/j.neuroimage.2008.07.009

Power, J.D., 2017. A simple but useful way to assess fMRI scan qualities. Neuroimage 154, 150–158. doi:10.1016/j.neuroimage.2016.08.009

Power, J.D., Barnes, K.A., Snyder, A.Z., Schlaggar, B.L., Petersen, S.E., 2012. Spurious but systematic correlations in functional connectivity MRI networks arise from subject motion. Neuroimage 59, 2142–2154. doi:10.1016/j.neuroimage.2011.10.018

Power, J.D., Mitra, A., Laumann, T.O., Snyder, A.Z., Schlaggar, B.L., Petersen, S.E., 2014. Methods to detect, characterize, and remove motion artifact in resting state fMRI. Neuroimage 84, 320–341. doi:10.1016/j.neuroimage.2013.08.048

Power, J.D., Schlaggar, B.L., Petersen, S.E., 2015. Recent progress and outstanding issues in motion correction in resting state fMRI. Neuroimage 105, 536–551. doi:10.1016/j.neuroimage.2014.10.044

Reuter, M., Tisdall, M.D., Qureshi, A., Buckner, R.L., van der Kouwe, A.J.W., Fischl, B., 2015. Head motion during MRI acquisition reduces gray matter volume and thickness estimates. Neuroimage 107, 107–115. doi:10.1016/j.neuroimage.2014.12.006

Roalf, D.R., Quarmley, M., Elliott, M.A., Satterthwaite, T.D., Vandekar, S.N., Ruparel, K., Gennatas, E.D., Calkins, M.E., Moore, T.M., Hopson, R., Prabhakaran, K., Jackson, C.T., Verma, R., Hakonarson, H., Gur, R.C., Gur, R.E., 2016. The impact of quality assurance assessment on diffusion tensor imaging outcomes in a large-scale population-based cohort. Neuroimage 125, 903–919. doi:10.1016/j.neuroimage.2015.10.068

Rosen, A.F.G., Roalf, D.R., Ruparel, K., Blake, J., Seelaus, K., Villa, L.P., Ciric, R., Cook, P.A., Davatzikos, C., Elliott, M.A., Garcia de La Garza, A., Gennatas, E.D., Quarmley, M., Schmitt, J.E., Shinohara, R.T., Tisdall, M.D., Craddock, R.C., Gur, R.E., Gur, R.C., Satterthwaite, T.D., 2018. Quantitative assessment of structural image quality. Neuroimage 169, 407–418. doi:10.1016/j.neuroimage.2017.12.059

Savalia, N.K., Agres, P.F., Chan, M.Y., Feczko, E.J., Kennedy, K.M., Wig, G.S., 2017. Motion-related artifacts in structural brain images revealed with independent estimates of in-scanner head motion. Hum. Brain Mapp. 38, 472–492. doi:10.1002/hbm.23397

Sforazzini, F., Bertero, A., Dodero, L., David, G., Galbusera, A., Scattoni, M.L., Pasqualetti, M., Gozzi, A., 2016. Altered functional connectivity networks in acallosal and socially impaired BTBR mice. Brain Struct. Funct. 221, 941–954. doi:10.1007/s00429-014-0948-9

Sled, J.G., Zijdenbos, A.P., Evans, A.C., 1998. A nonparametric method for automatic

correction of intensity nonuniformity in MRI data. IEEE Trans. Med. Imaging 17, 87–97. doi:10.1109/42.668698

Smith, S.M., 2002. Fast robust automated brain extraction. Hum. Brain Mapp. 17, 143–155. doi:10.1002/hbm.10062

Smith, S.M., Jenkinson, M., Johansen-Berg, H., Rueckert, D., Nichols, T.E., Mackay, C.E., Watkins, K.E., Ciccarelli, O., Cader, M.Z., Matthews, P.M., Behrens, T.E.J., 2006. Tract-based spatial statistics: voxelwise analysis of multi-subject diffusion data. Neuroimage 31, 1487–1505. doi:10.1016/j.neuroimage.2006.02.024

Tournier, J.-D., Mori, S., Leemans, A., 2011. Diffusion tensor imaging and beyond. Magn. Reson. Med. 65, 1532–1556. doi:10.1002/mrm.22924

Tustison, N.J., Avants, B.B., Cook, P.A., Zheng, Y., Egan, A., Yushkevich, P.A., Gee, J.C., 2010. N4ITK: improved N3 bias correction. IEEE Trans. Med. Imaging 29, 1310–1320. doi:10.1109/TMI.2010.2046908

Yang, H., Long, X.-Y., Yang, Y., Yan, H., Zhu, C.-Z., Zhou, X.-P., Zang, Y.-F., Gong, Q.-Y., 2007. Amplitude of low frequency fluctuation within visual areas revealed by resting-state functional MRI. Neuroimage 36, 144–152. doi:10.1016/j.neuroimage.2007.01.054

Zacà, D., Hasson, U., Minati, L., Jovicich, J., 2018. Method for retrospective estimation of natural head movement during structural MRI. J. Magn. Reson. Imaging 48, 927–937. doi:10.1002/jmri.25959

Zang, Y., Jiang, T., Lu, Y., He, Y., Tian, L., 2004. Regional homogeneity approach to fMRI data analysis. Neuroimage 22, 394–400. doi:10.1016/j.neuroimage.2003.12.030

Zhang, H., Schneider, T., Wheeler-Kingshott, C.A., Alexander, D.C., 2012. NODDI: practical in vivo neurite orientation dispersion and density imaging of the human brain. Neuroimage 61, 1000–1016. doi:10.1016/j.neuroimage.2012.03.072

Zheng, W., Chee, M.W.L., Zagorodnov, V., 2009. Improvement of brain segmentation accuracy by optimizing non-uniformity correction using N3. Neuroimage 48, 73–83. doi:10.1016/j.neuroimage.2009.06.039

Zou, Q.-H., Zhu, C.-Z., Yang, Y., Zuo, X.-N., Long, X.-Y., Cao, Q.-J., Wang, Y.-F., Zang, Y.-F., 2008. An improved approach to detection of amplitude of low-frequency fluctuation (ALFF) for resting-state fMRI: fractional ALFF. J. Neurosci. Methods 172, 137–141. doi:10.1016/j.jneumeth.2008.04.012